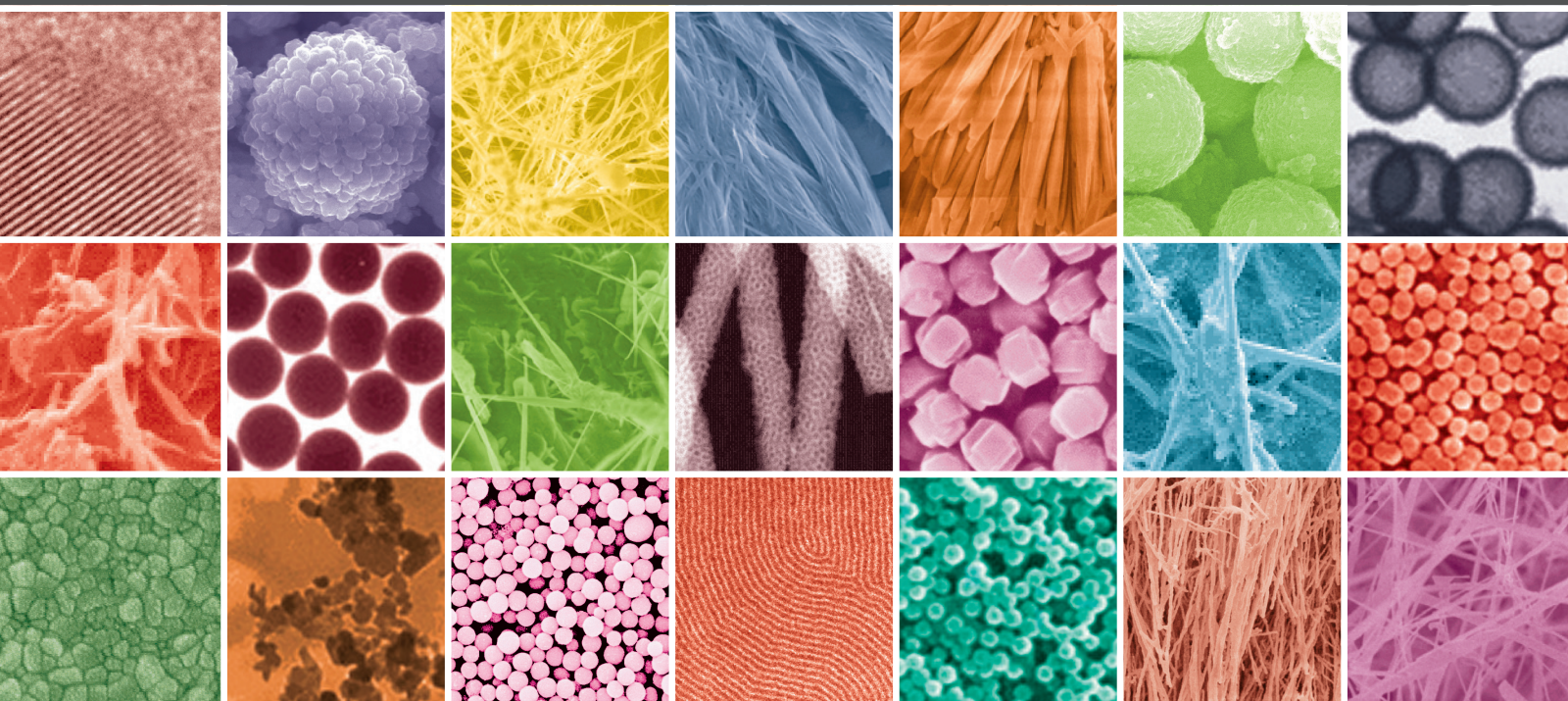# Nanomaterials for Solar Energy Harvesting and Storage

Guest Editors: Peng Hu, Yuebin Cao, Ning Han, Danping Wang, and Jiangchao Chen

Nanomaterials for Solar Energy Harvesting and Storage

Nanomaterials for Solar Energy Harvesting and Storage

Guest Editors: Peng Hu, Yuebin Cao, Ning Han, Danping Wang, and Jiangchao Chen

Editorial Board

Contents

Editorial

Nanomaterials for Solar Energy Harvesting and Storage

Peng Hu,[1] Yuebin Cao,[2] Ning Han,[3] Danping Wang,[4] and Jiangchao Chen[5]

[1]*Chinese Academy of Sciences, Beijing 100190, China*
[2]*Hanyang University, Seoul 04763, Republic of Korea*
[3]*City University of Hong Kong, Kowloon, Hong Kong*
[4]*Energy Research Institute, NTU (ERIN), Singapore 637141*
[5]*University of South Dakota, Vermillion, SD 57069, USA*

Correspondence should be addressed to Peng Hu; pengh@home.ipe.ac.cn

Solar energy harvesting and storage have nowadays attracted tremendous research efforts due to the increasing energy challenges that fossil fuels are being rapidly consumed by modern technology. For material chemists, how to develop materials that are effective in harnessing solar energy is the primary step to tackle this challenge. Apart from selection of materials with intrinsic physical properties to utilize solar energy, scientists have also been studying the unique properties when the particle size reduced to the nanometer scale. Nanomaterials, which have high surface-to-volume ratio, cover a variety of shapes of nanoparticles, nanorods, nanoporous framework, and so on. One can also easily tune the optical and charge transfer properties by changing the size of semiconductor nanomaterials. The chemical properties such as catalytic activity can also be remarkably changed with increased surface atoms of nanocatalysts.

This special issue is mainly dedicated to the synthesis of functional nanomaterials which can be used to harvest or store solar energy. As materials innovation has great potential to advance this area, most of the articles in this special issue describe the latest preparation methods and some of the current progress of semiconductor-based materials.

The desire to make solar energy into usable energy format has led to the fast development of solar cells, a direct way to convert solar energy into electricity. The ideal candidate materials to be used in solar cells should possess proper band gap to harvest as much sunlight as possible, good charge transport properties, excellent stability, and cheap cost. The preparation of $CuInS_2$ thin films has been reported in two papers. R.-F. Guan and coworkers prepared the $CuInS_2$ thin films via one-step electrodeposition method. They investigated the effects of synthesis parameters on the structure, morphology, and optical and electrical properties on the final $CuInS_2$ thin films, and optimal preparation conditions were proposed. In another paper, R.-F. Guan and coworkers used magnetron sputtering followed by sulfurization method to prepare $CuInS_2$ thin films. Optimized sputtering power, sputtering gas pressure, heat treatment temperature, and duration were reported. With detailed study on the synthesis parameters in each paper, these two papers will certainly help peer researchers for the facile preparation of $CuInS_2$ based solar cells.

As a special type of solar cell, Dye-Sensitized Solar Cells (DSSCs) use photoexcited electrons generated from the conduction band of TiO_2 thin films to generate electricity with the assistance of dye molecules. The key factors to prepare an effective DSSC are high surface area of TiO_2 thin film, efficient charge injection from dye molecules to TiO_2, and minimal loss of electrons from TiO_2 to outer circuit. Kim and coworkers developed TiO_2 nanobranch/nanoparticle hybrid structure to increase the surface area of thin film and thus the loading of dye molecules. Light harvesting efficiency is greatly promoted, leading to tripled incident photon conversion efficiency (IPCE) compared with bare nanobranch thin films.

A comprehensive review on the hybrid organic-inorganic perovskites solar cells is given by the Xu group, covering perovskite synthesis methods, hole transport materials, photoanode morphologies, and outlook and challenges for perovskites based solar cells.

Another alternative and interesting approach to utilize solar energy is through the processes of photocatalysis or artificial photosynthesis to convert solar energy into chemical energy to drive certain chemical reactions, for example, water splitting or photodegradation of organic pollutants. P. Dong and coworkers synthesized Ag_3PO_4 triangular prism by a simple coprecipitation method which was used as an excellent photocatalyst for organic compounds degradation under light irradiation.

Biomass, the nature's way of storing solar energy, is also covered in our special issue. Y. Zhang and coworkers used corn straw as the raw material, ionic liquids as solvents, and acids as catalysts to study the effects of hydrolysis conditions on reducing sugar concentration, and optimal hydrolysis parameters were provided.

White light emitting diodes (LEDs) have been acknowledged as highly efficient and green light sources. When coupled with solar cells, the white LEDs can provide efficient lighting without consuming other energy resources. R.-F. Guan and coworkers synthesized $Y_{2.94-x}Al_5O_{12}$(YAG):$Ce_{0.06}Pr_x$ phosphors with various Pr^{3+} concentrations by coprecipitation method. They investigated the influence of Pr^{3+} doping concentrations on the phases, luminescent properties, and energy transfer phenomenon from Ce^{3+} to Pr^{3+}.

Peng Hu
Yuebin Cao
Ning Han
Danping Wang
Jiangchao Chen

Research Article

Facile Preparation of TiO$_2$ Nanobranch/Nanoparticle Hybrid Architecture with Enhanced Light Harvesting Properties for Dye-Sensitized Solar Cells

Ju Seong Kim,[1] Seong Sik Shin,[1] Hyun Soo Han,[2] Sun Shin,[1] Jae Ho Suk,[1] Kisuk Kang,[1] Kug Sun Hong,[1] and In Sun Cho[3]

[1]*Research Institute of Advanced Materials, Seoul National University, Seoul 151-744, Republic of Korea*
[2]*Department of Mechanical Engineering, Stanford University, Stanford, CA 94305, USA*
[3]*Department of Materials Science and Engineering and Department of Energy Systems Research, Ajou University,*
 Suwon 443-749, Republic of Korea

Correspondence should be addressed to Kug Sun Hong; kshongss@plaza.snu.ac.kr and In Sun Cho; cisinsnu@gmail.com

We report TiO$_2$ nanobranches/nanoparticles (NBN) hybrid architectures that can be synthesized by a facile solution phase method. The hybrid architecture simultaneously improves light harvesting and charge collection performances for a dye-sensitized solar cell. First, TiO$_2$ nanorods with a trunk length of 2 μm were grown on a fluorine-doped tin oxide (FTO)/glass substrate, and then nanobranches and nanoparticles were deposited on the nanorods' trunks through a solution method using an aqueous TiCl$_3$ solution at 80°C. The relative amount of nanobranches and nanoparticles can be controlled by multiplying the number of TiCl$_3$ treatments to maximize the amount of surface area. We found that the resultant TiO$_2$ NBN hybrid architecture greatly improves the amount of dye adsorption (five times compared to bare nanorods) due to the enhanced surface area, while maintaining a fast charge collection, leading to a three times higher current density and thus tripling the maximum power conversion efficiency for a dye-sensitized solar cell.

1. Introduction

Dye-sensitized solar cells (DSSCs) have attracted attention as one of the most promising solar conversion devices due to their low fabrication cost and high conversion efficiency [1–4]. In general, a DSSC consists of four parts: the sensitizer (dye molecule), a semiconductor for electron transport, a redox electrolyte, and charge collecting electrodes. Typically, nanoparticle-based photoanodes using n-type semiconductors (TiO$_2$, ZnO, SnO$_2$, BaSnO$_3$, Zn$_2$SnO$_4$, etc.) have been investigated for adsorption of dye molecules as a result of their large surface areas [4–10]. However, these nanoparticle-based photoanodes limit charge collection efficiency because they have a large number of transport-limiting trapping/detrapping events on the nanoparticle surface; that is, they show a low charge collection efficiency [11, 12].

One strategy for overcoming this low charge collection efficiency is the use of vertically aligned one-dimensional (1D) nanostructures, which offer a direct electron transport pathway to the electrode, thus enabling low charge recombination. To date, various 1D nanostructured photoanodes have been studied, including nanowires (NWs), nanotubes (NTs), nanoparticle-decorated NWs, dendritic NWs, and core/shell NWs [13–19]. For instance, single-crystal TiO$_2$ nanowires were found to have a large electron diffusion coefficient compared to TiO$_2$ nanoparticles, owing to a lower density of surface defects [14]. Additionally, a preferentially oriented anatase TiO$_2$ nanotube, which has a small quantity of high angle grain boundaries, shows a large electron diffusion coefficient and diffusion length compared to TiO$_2$ nanoparticles [17]. Moreover, dendritic ZnO NWs with multiple branches demonstrated an enhanced photocurrent

and internal quantum efficiency over nanoparticle-based cells [19]. Nevertheless, these 1D nanostructured photoanodes frequently display a low light harvesting efficiency due to a lower dye loading capacity, which leads to a low photocurrent density compared to nanoparticle-based DSSCs [14]. Recently, to address this low dye loading problem in 1D nanostructures, a few studies have adopted hierarchical structures based on the 1D nanostructures (e.g., nanoforests and branched arrays) [20–23]. Even though the hierarchical structures exhibit improved charge collection and light harvesting efficiencies, their preparation methods are somewhat complex and require vacuum equipment, making it difficult to reproduce the synthesis technique and prepare large scale devices.

Here, we report a facile solution phase method to synthesize a TiO$_2$ nanostructured photoanode consisting of nanobranches/nanoparticles on the trunks of the NWs. These hybrid NWs can be synthesized simply by using an aqueous TiCl$_3$ solution at low temperature (80°C). One advantage of our method is that it enables us to control the relative amount of nanobranches and nanoparticles on the TiO$_2$ NW trunks as a result of applying multiple TiCl$_3$ treatments, to maximize dye adsorption (i.e., the light harvesting property). Additionally, this method facilitates a scalable preparation (up to a 4-inch wafer) due to it being a low temperature process. We carefully investigated the effect of the TiCl$_3$ treatment on the morphology progress and dye adsorption capacity, and we demonstrate that the hybrid architecture improves the photocurrent and incident photon-to-current conversion efficiency (IPCE) for DSSCs by a factor of two compared to nanorod-based DSSCs.

2. Experimental

2.1. Preparation of the TiO$_2$ Nanowires (NWs). Rutile TiO$_2$ NWs were synthesized on a fluorine-doped tin oxide (FTO)/glass substrate by a hydrothermal method [24]. Before growing the TiO$_2$ nanorods, a TiO$_2$ seed layer was deposited by a spin coating method using a TiO$_2$ polymeric sol [25] and then annealed at 450°C for 1 h. Titanium butoxide (97%, Aldrich) was slowly added to 50 mL of a hydrochloric acid (HCl) aqueous solution (25 mL of deionized (DI) water + 25 mL concentrated HCl solution (38%)) and stirred for 30 min to obtain a transparent solution. This precursor solution was transferred into a sealed Teflon-lined stainless steel autoclave (100 mL volume) and then the TiO$_2$ seed layer-coated FTO/glass substrates were immersed in this solution. The autoclave was placed in an electric oven and heated to 170°C for 6 h without stirring. The resultant TiO$_2$ nanorod samples were washed with DI water several times and finally annealed at 450°C for 1 h in air.

2.2. TiCl$_3$ Treatment. To grow the nanobranches and nanoparticles, the TiO$_2$ nanorod samples were immersed into a solution containing 10 mL of DI water, 0.1 mL of concentrated HCl solution, and 1 mL of TiCl$_3$ solution (Aldrich, 10 wt.% in 20–30 wt.% HCl solution) and held at 80°C for 30 min in an oven. The effect of the TiCl$_3$ treatment time (30 min, 1 h, 2 h,

and 4 h) on the morphology was examined first. The relative quantity of nanobranches/nanoparticles was controlled by repeating the TiCl$_3$ treatment. We have labeled the sample names as 30 min-1, 30 min-2, 30 min-3, and 30 min-4 to correspond to the number of additional TiCl$_3$ treatments. Afterward, all samples were washed with DI water and annealed at 450°C for 1 h in air.

2.3. Fabrication of DSSCs. The annealed samples were soaked in a ruthenium dye solution (N719, ruthenium (2,2′bipyridyl-4,4′dicarboxylate)$_2$(NCS)$_2$) at room temperature for 12 h. Platinum-coated FTO substrates prepared by sputtering were used as the counter electrodes. The sandwich-type DSSCs were assembled using the samples as the photoanodes and the Pt-coated FTO glasses as the counter electrodes with a hot-melt film (~60 μm, Surlyn, DuPont) as a spacer. Finally, the electrolyte was an iodide-based liquid electrolyte (SI16 L1535-01, Merck), which was introduced into the cell through a hole in the counter electrode. The active area of all samples was 0.25 cm^2.

2.4. Material and DSSC Characterization. The crystal structure and phase of the synthesized samples were identified by an X-ray diffractometer (XRD, Bruker, New D8 Advance) with CuKα radiation operated at 40 kV and 40 mA. The morphologies of the prepared samples were observed by a field-emission scanning electron microscope (FESEM, Hitachi, SU70) and a high-resolution transmission electron microscope (HRTEM, JEOL, JEM-3000F). The photovoltaic performance and electron impedance spectroscopy (EIS) of the DSSCs were measured with a potentiostat (CH Instruments, CHI308C) under AM 1.5G simulated solar light (100 mW/cm^2, Sol3A, Newport). The ultraviolet-visible (UV-Vis) absorption spectra of the dye solutions, collected by desorption from the samples, were investigated with an UV-Vis spectrometer (Agilent Technologies, Cary 5000). The DSSCs' electron transport properties were characterized by intensity-modulated photovoltage spectroscopy (IMVS) using an electrochemical workstation (Zennium, Zahner) with an attached frequency analyzer and a light-emitting diode (667 nm).

3. Results and Discussion

The morphology of the TiO$_2$ nanorods (NRs) used as the stem for the TiO$_2$ hybrid architecture is shown in Figures S1 and S2 (in Supplementary Material available online at http://dx.doi.org/10.1155/2015/139715). The NRs are grown on the FTO/glass substrate by a hydrothermal method [26]. The NRs have an average diameter of the length of 103±15 nm and 2.0 ± 0.2 μm (Tables S1 and S2), presenting high crystallinity with a preferred growth direction of [001]. Figure 1 shows top-view FESEM images of the TiO$_2$ hybrid architectures' microscopic morphologies, prepared by repeating the TiCl$_3$ treatment (1–4 times) at 80°C for 30 min. It can be seen that the TiCl$_3$ treatment significantly affects the morphology of the TiO$_2$ NRs. After the first TiCl$_3$ treatment (sample 30 min-1), small nanobranches (~10 nm in diameter and
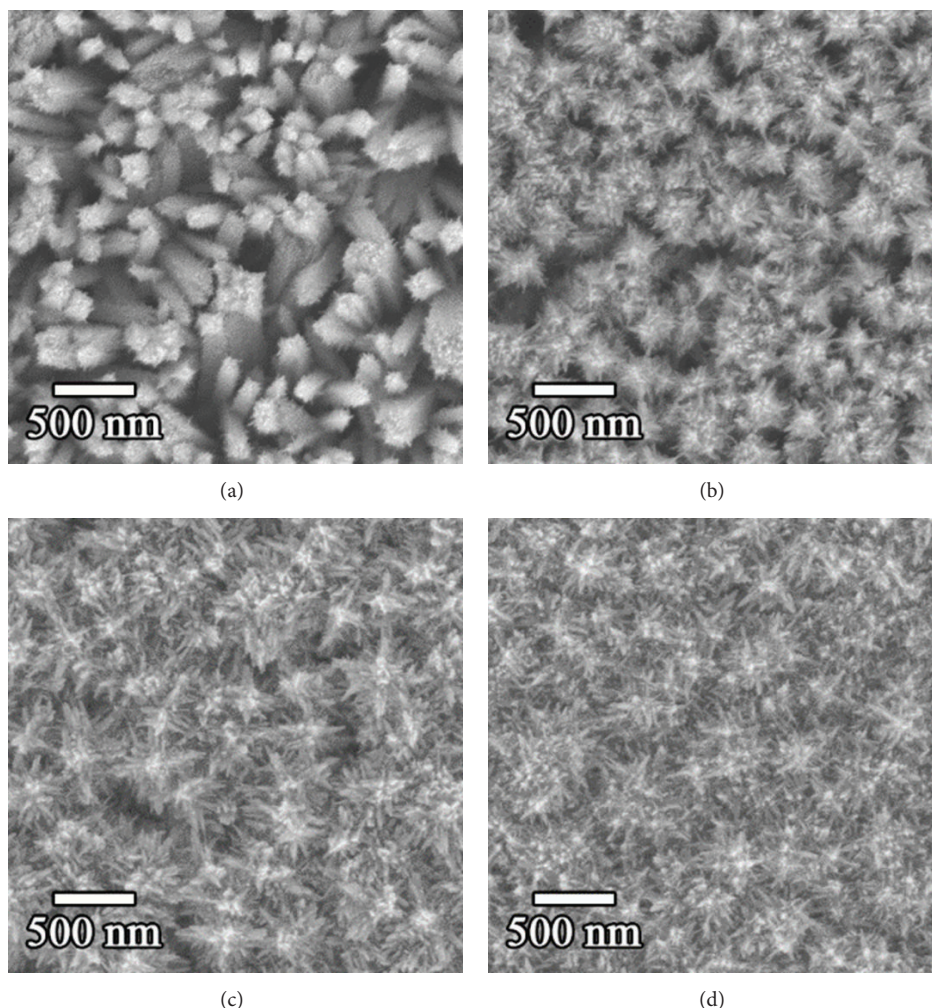
FIGURE 1: The effect of the number of TiCl$_3$ treatments on the morphology of the TiO$_2$ NWs. Top-view FESEM images, (a) one 30 min treatment (30 min-1), (b) two-time treatments (30 min-2), (c) three-time treatments (30 min-3), and (d) four-time treatments (30 min-4).

~60 nm in length) were formed on the surface of the individual TiO$_2$ NRs (Figure 1(a)), which lengthen further (~100 nm long) with an increased density on the NR surface after the second TiCl$_3$ treatment (sample 30 min-2, Figure 1(b)). When the treatment was repeated three times (sample 30 min-3, Figure 1(c)), the length of the nanobranches increased to 200–300 nm, reducing the interspaces between the TiO$_2$ NRs; these interspaces decreased significantly after the fourth treatment (sample 30 min-4, Figure 1(d)). We also investigated the effects of the TiCl$_3$ treatment duration time (Figure S3). An increased duration time provides a similar effect on the morphology; that is, it lengthens the nanobranches and increases their density as the duration time was increased from 30 min to 4 h.

The detailed variation in the TiO$_2$ nanostructure morphology with multiple TiCl$_3$ treatments was investigated further by utilizing cross-sectional FESEM images (Figure 2). For the 30 min-1 and 30 min-2 samples, there were no significant changes in the TiO$_2$ NRs except for the formation of nanobranches. However, for the 30 min-3 sample, the nanobranches grew in length, reducing the space between

NRs, especially at their tops (Figure 2(c)). Interestingly, at the bottom of the nanorods, nanoparticles with an average size of ~30 nm formed together with the nanobranches, suggesting that more than three TiCl$_3$ treatments induce a different growth mode, generating nanoparticles at the bottom of the NRs. Finally, after the fourth treatment (30 min-4), the TiO$_2$ nanoparticles completely filled the NR interspaces, up to the top of the film. These two different growth modes, that is, the nanobranch and nanoparticle growth, during the multiple TiCl$_3$ treatments enable the morphology to be tuned, thereby controlling the relative surface area of the 1D nanostructure based on the NRs.

The XRD patterns of the samples discussed above are shown in Figure 3. All diffraction peaks of the TiO$_2$ NRs (30 min-1) are in agreement with tetragonal rutile TiO$_2$ (JCPDS number 21-1276, P4$_2$/mnm, $a = b = 4.593$ Å, $c = 2.959$ Å). In general, rutile TiO$_2$ NRs prepared by a hydrothermal method grow along the (001) plane, as it has the fastest growth rate compared to the other crystal faces [13, 27, 28]. Similar to other reports, our TiO$_2$ NRs have a preferred growth direction of [001], which was

(a)

(b)

(c)

(d)
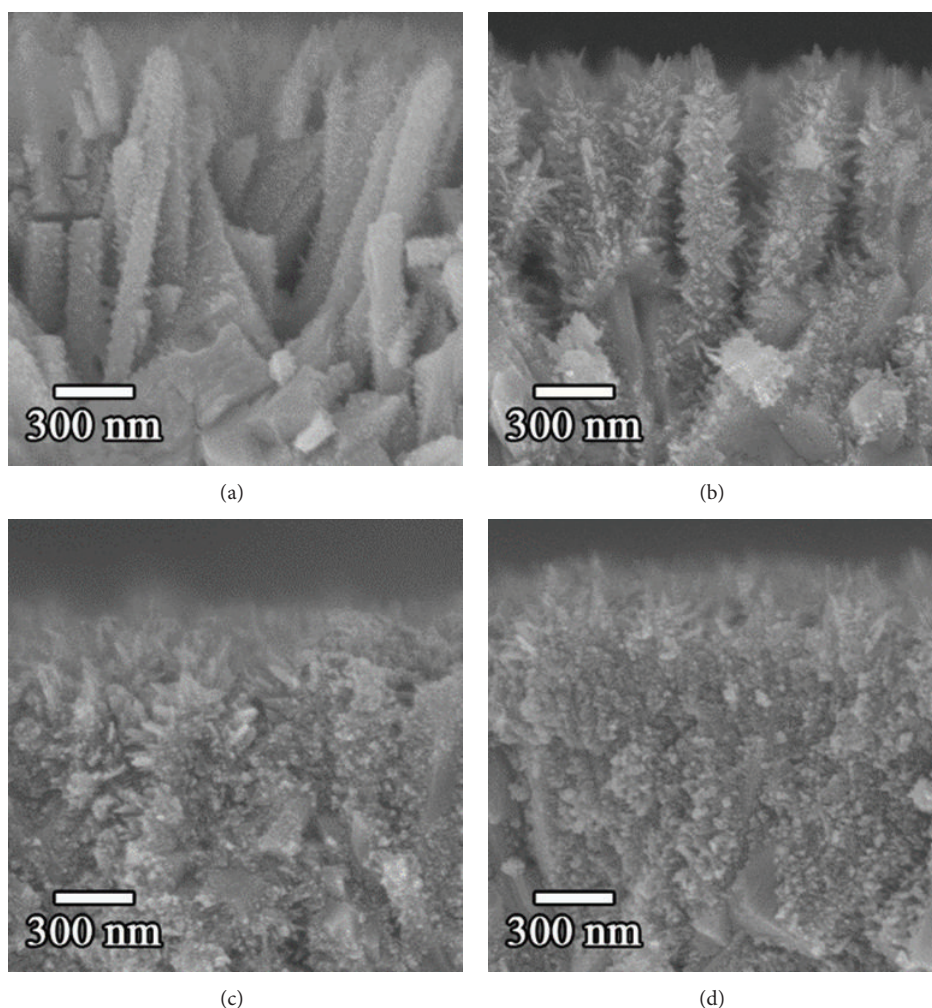
FIGURE 2: Cross-sectional SEM images of the TiO$_2$ NWs obtained by repeating the TiCl$_3$ treatments, (a) 30 min-1, (b) 30 min-2, (c) 30 min-3, and (d) 30 min-4. After three TiCl$_3$ treatments, nanoparticles start to form and fill the gaps between NWs.
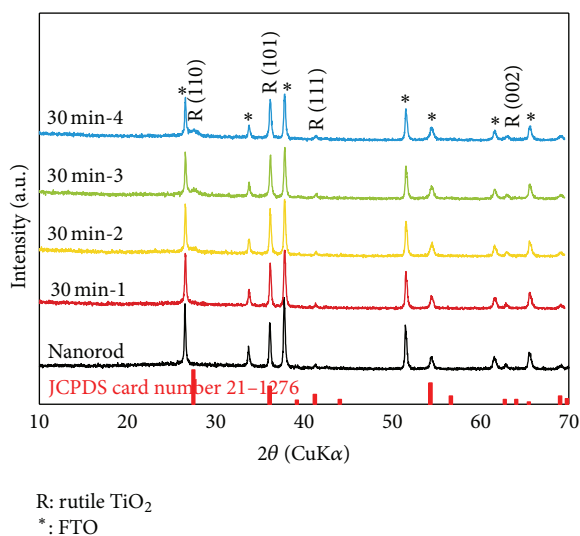
FIGURE 3: XRD patterns of TiO$_2$ NWs and hybrid architectures obtained by the TiCl$_3$ treatments (0–4 times).

also confirmed by a TEM analysis (Figure S2). For the XRD peaks of the multiple TiCl$_3$ treatment samples, there were no considerable differences from the 30 min-1 sample, suggesting that the nanobranches and nanoparticles are also rutile tetragonal structures. The perceptible development of the (110) diffraction peaks at 27.5° in the 30 min-2, 30 min-3, and 30 min-4 samples implies that the nanobranches have the same preferred [001] growth direction [24].

Based on the above observation, the formation process of the TiO$_2$ nanobranch/nanoparticle (NBN) hybrid architectures is displayed schematically in Figure 4. After the first treatment, short nanobranches are formed on the surface of the NRs, which grow to longer nanobranches with an average length of ~100 nm after the second TiCl$_3$ treatment. The third TiCl$_3$ treatment induces nanoparticle growth from the bottom of the film, which reduces the interspaces between the NRs at their bases. With a further TiCl$_3$ treatment, however, additional nanoparticles formed, filling the remaining interspaces between the NRs to the top of the film, finally forming a NBN hybrid architecture.
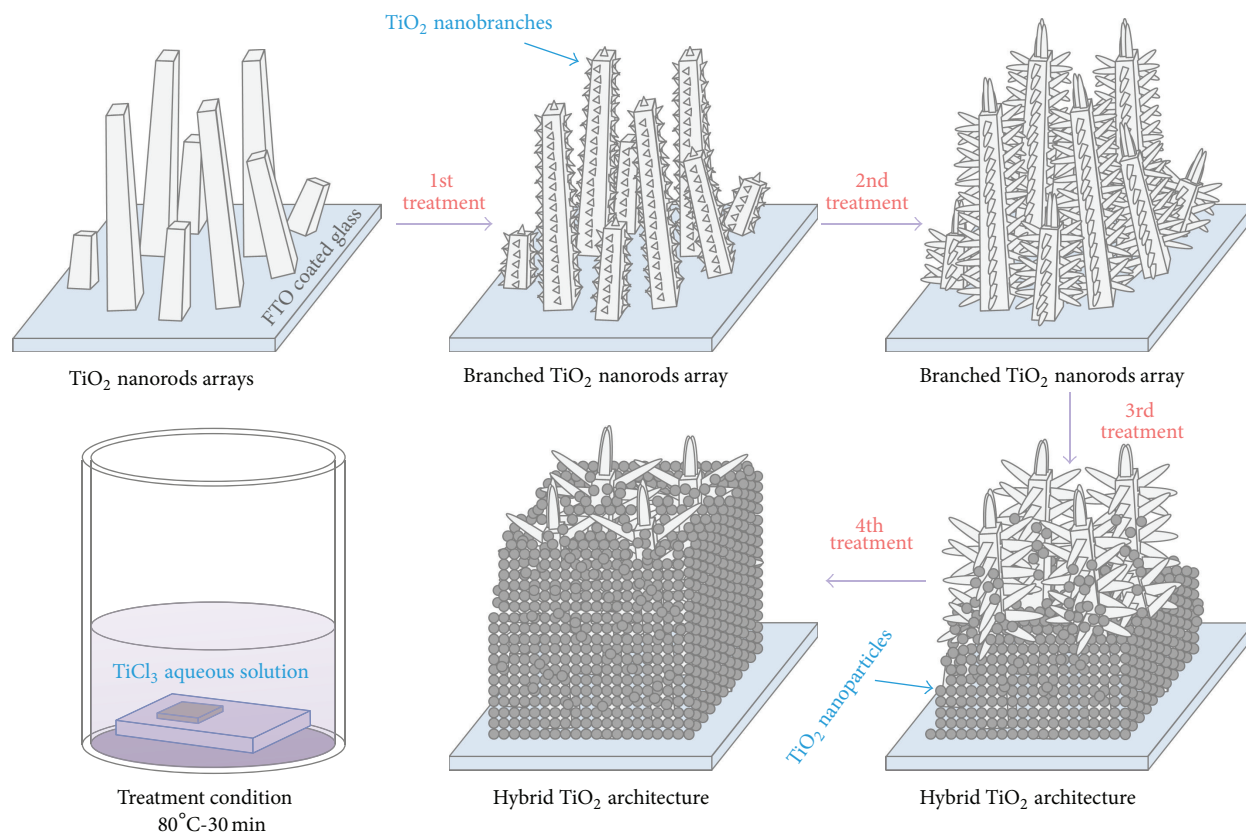
FIGURE 4: Schematic illustration of the TiO$_2$ hybrid architecture formation process.

It should be noted that these interesting 1D architectures are obtained by simply repeating the TiCl$_3$ treatment, which enabled the unusual growth (or deposition) behavior during the additional TiCl$_3$ treatments. In general, the pH of the growth solution significantly affects the growth morphology (i.e., the crystal phase and morphology) of TiO$_2$ nanocrystals [29], that is, nanoparticles near pH 7 and elongated nanorods or nanoneedles below pH 4. Therefore, the two different growth modes, of the nanobranches and nanoparticles, might relate to the change in the solution's pH value during the multiple TiCl$_3$ treatments. A detailed analysis of this is under investigation.

Next, in order to check the usefulness of the NBN hybrid architectures for a solar energy conversion device, we fabricated dye-sensitized solar cells (DSSCs) with them. First, the light harvesting behavior, that is, the dye adsorption property, was investigated by UV/Vis absorption spectroscopy (Figure 5). The absorption spectra were obtained of dye solutions after collecting the dye by a desorption process in a basic solution. The peak at 510 nm in the absorption spectra is a characteristic peak of these dye molecules (N719), and this can be used to estimate the amount of dye molecules adsorbed onto the TiO$_2$ surface. As shown in the inset of Figure 5, the amount of adsorbed dye molecules continued to increase with repeated TiCl$_3$ treatments, before becoming saturated with the 30 min-3 sample. The amount of adsorbed

dye of the 30 min-4 sample increased nearly by a factor of four compared to the 30 min-0 sample, indicating that the NBN hybrid architecture (30 min-4 sample) has a larger surface area, thus improving the light harvesting efficiency for the DSSCs.

Figure 6(a) shows the photocurrent density-voltage curves of the DSSCs fabricated using the above four samples, which were measured under AM 1.5G simulated solar light (1 sun, 100 mW/cm^2) and their representative solar cell parameters are shown in Figures 6(b) and 6(c) (with the other parameters summarized in Table 1). Initially, the short circuit photocurrent density (J_{sc}) values increased linearly until the third treatment and eventually reaching a maximum J_{sc} value of 13.4 mA/cm^2 for the fourth treatment. This result strongly correlates with the absorbance spectra of the desorbed dye shown in the inset of Figure 5, indicating that the NBN hybrid architecture has an improved light harvesting property, thus increasing the J_{sc} for DSSCs. The open circuit voltage (V_{oc}) of the TiO$_2$ NR-based DSSC was 0.82 V. This V_{oc} value decreased slightly with an increasing number of TiCl$_3$ treatments to 0.77, 0.72, 0.71, and 0.69 V for the 30 min-1, 30 min-2, 30 min-3, and 30 min-4 samples, respectively. In the case of the fill factor (FF) values, there were no notable differences (Table 1). As a result, the power conversion efficiency was enhanced from 2.6% (for the NR-based DSSC) to

TABLE 1: The photocurrent density-voltage characteristics and dye loading of the NBN-TiO$_2$-based DSSCs with various TiCl$_3$ treatment times.

Photoelectrode	J_{sc} [mA/cm^2]	V_{oc} [V]	FF [%]	η [%]	Dye loading [$\times 10^{-9}$ mole/cm^3]
Nanorod	5.62	0.82	57	2.6	0.34
30 min-1	7.86	0.77	58	3.5	0.43
30 min-2	11.26	0.72	58	4.7	0.92
30 min-3	12.95	0.71	57	5.2	1.50
30 min-4	13.35	0.69	58	5.3	1.65
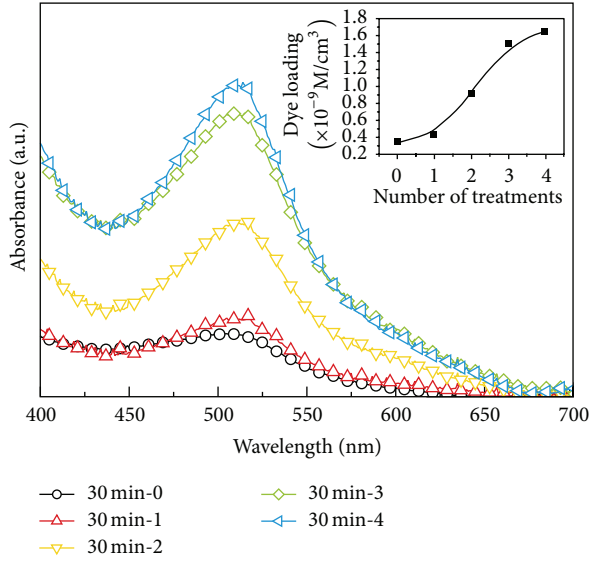
FIGURE 5: The UV-Vis absorption spectra of the dye (N719) detached from the TiO$_2$ films prepared under a varied number of TiCl$_3$ treatments. To measure the UV-Vis absorption spectra of the dye (N719), it was first desorbed by an ammonium (NH$_4$OH) solution in water and ethanol (50 : 50, v/v).

5.3% (for the NBN hybrid architecture- (30 min-4-) based DSSC), demonstrating that the NBN hybrid architecture is advantageous to improve J_{sc} in DSSCs.

To understand the effect of the multiple TiCl$_3$ treatments on the electron dynamics, an intensity-modulated photocurrent/photovoltage spectroscopy (IMPS/IMVS) was used to measure the samples (Figure S4). All samples show a typical power-law dependence of their transport time constants on the J_{sc} value (Figure S4a). This indicates an exclusive random walk of photoelectrons between trap sites having a power-law distribution of waiting (release) times in the form of $\tau^{-1-\alpha}$, where the parameter α can be related to the shape of the trap distribution [30, 31]. Initially, the charge transport time increased with the additional TiCl$_3$ treatments, indicating that the route photoelectrons travel to the FTO substrate became longer and more complicated due to the nanobranches and nanoparticles. This reduction in the transport time constant competes with the effect of the increased dye adsorption. The transport time constant and the dye adsorption correlate to the charge collection efficiency and light harvesting efficiency, respectively, which determine the power conversion efficiency. However, since

the effects of the dye adsorption are dominant, the power conversion efficiency of the TiO$_2$ NBN hybrid architecture DSSC increased with repeated TiCl$_3$ treatments.

Second, the charge recombination time constant consistently decreased with an increasing number of TiCl$_3$ treatments. The infiltrated TiO$_2$ nanobranches and nanoparticles decreased the diffusion efficiency of the I$_3^-$ ions in the electrolyte. The relation between the recombination time and V_{oc} can be described by the following equation [32, 33]:

$$V_{oc} = \frac{RT}{\beta F} \ln\left(\frac{AI}{n_0 k_1 \left[I_3^- \right] + n_0 k_2 \left[D^+ \right]} \right), \quad (1)$$

where R is the molar gas constant, T is the temperature, β is the reaction order for the electrons, F is the Faraday constant, A is the electrode area, I is the incident photon flux, n_0 is the concentration of accessible electronic states in the conduction band, and k_1 and k_2 are the kinetic constants of the injected electron with triiodide (I$_3^-$) back reaction and the recombination of these electrons with oxidized dye (D$^+$) molecules, respectively. Neglecting the recombination of the injected electrons with oxidized dye molecules, the V_{oc} value is logarithmically dependent on the back reaction of these electrons with the triiodide (k_1). Therefore, the rate of the electron recombination from the TiO$_2$ photoanode to the I$_3^-$ ions in the electrolyte increased with an increasing number of TiCl$_3$ treatments.

Figure 7 shows the incident photon-to-current efficiency (IPCE) spectra of the TiO$_2$ photoanode-based DSSCs. All of the DSSCs show the typical spectral response of N719-based DSSCs with a peak at approximately 530 nm. However, the maximum IPCE (or external quantum efficiency, EQE) varies with the number of TiCl$_3$ treatments. The 30 min-4 sample exhibited the maximum IPCE and the NR sample displayed the minimum IPCE. The IPCE of DSSCs is determined by the light harvesting efficiency (η_{lh}), the charge injection efficiency (η_{inj}), and the charge collection efficiency (η_{cc}). The IPCE value can be expressed by the following equation:

$$\text{IPCE} \, (\%) = \eta_{lh} \times \eta_{inj} \times \eta_{cc}. \quad (2)$$

The light harvesting efficiency is generally affected by the dye loading capacity [34]. As mentioned in Figure 5, the dye loading capacity of the TiO$_2$ photoanodes increased significantly with multiple TiCl$_3$ treatments, implying that the light harvesting efficiency increased with additional TiCl$_3$ treatments. On the other hand, the IMPS and IMVS data (Figure S4) demonstrate that the charge collection efficiency decreased monotonically with the multiple TiCl$_3$ treatments.

(a)

(b)

(c)
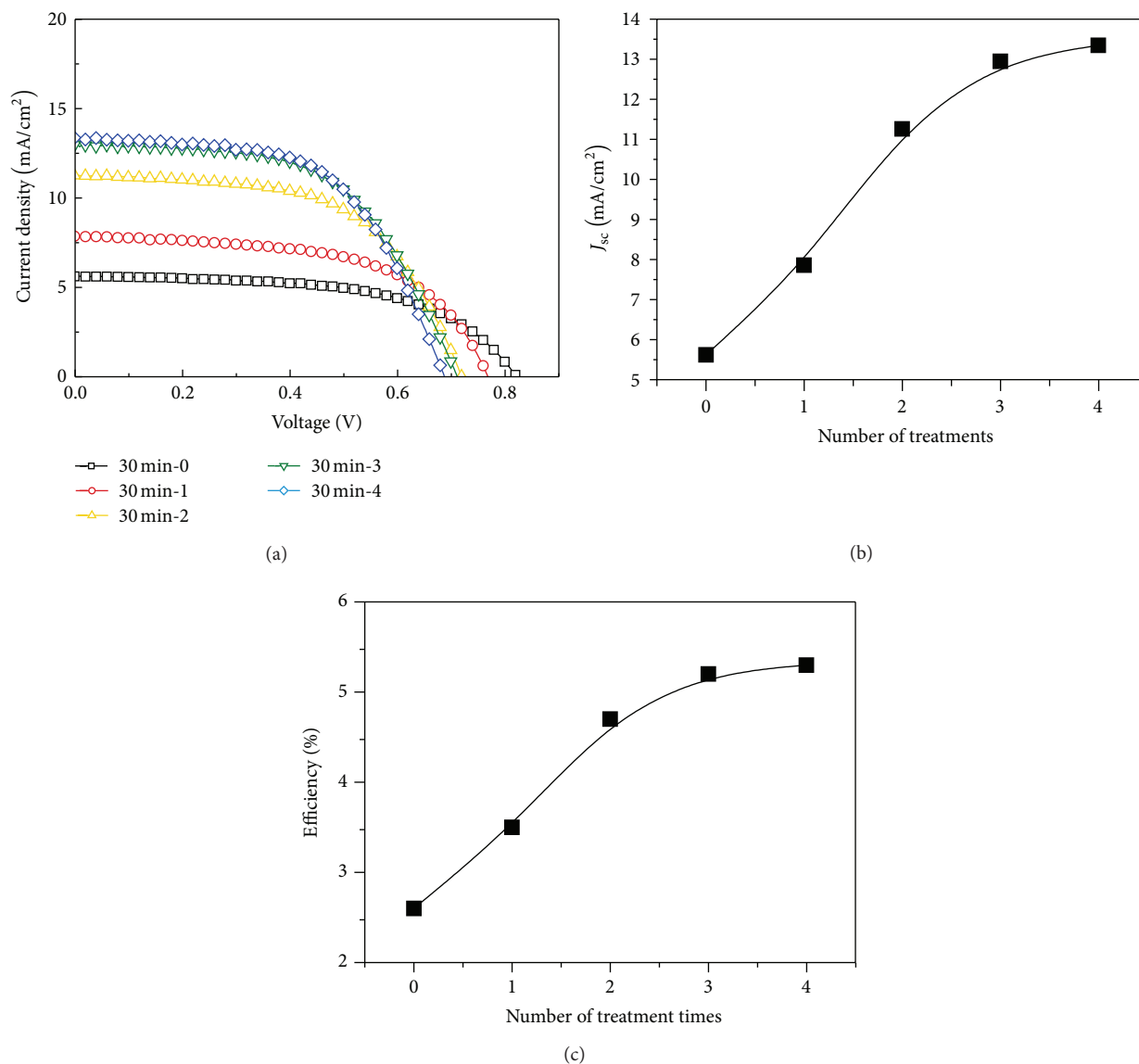
FIGURE 6: (a) The photocurrent density-voltage curves of the NBN-TiO$_2$-based DSSCs measured under AM 1.5G, at a 1 sun light intensity, using a shadow mask. Effect of treatment times on (b) photocurrent density (J_{sc}) and (c) efficiency (%).

Even though the NBN hybrid architecture reduced the electron transport property slightly, it can be concluded that the enhancement seen in the light harvesting efficiency was greater than the decrease in the charge collection efficiency. Interestingly, the IPCE values of the samples after multiple TiCl$_3$ treatments show a shoulder at a longer wavelength (>680 nm), indicating that the NBN hybrid architecture has additional enhancement effects for DSSCs, that is, improving the light scattering effect. This light scattering effect also enhances the light harvesting efficiency in combination with the increased dye loading capacity.

4. Conclusions

In summary, we report on a TiO$_2$ hybrid architecture composed of TiO$_2$ nanobranches and nanoparticles, easily synthesized by a solution phase method. A TiCl$_3$ aqueous solution treatment at 80°C enables a controlled morphology of the TiO$_2$ nanorods. By repeating this TiCl$_3$ treatment, nanobranches and/or nanoparticles are deposited on the trunks of the TiO$_2$ nanorods, giving hybrid architecture with an enhanced surface area. We found that the resultant TiO$_2$ nanobranch/nanoparticle hybrid architecture greatly improved the dye adsorption (five times compared to bare nanorods) due to the enhanced surface area, albeit a slight decrease in a charge collection property. Additionally, the complex architecture produces a large light scattering effect, eventually leading to a three times greater current density and thus tripling the maximum power conversion efficiency for a dye-sensitized solar cell. We believe that the synthesized TiO$_2$ hybrid architecture, after further structural optimization, has the potential for use in other energy harvesting devices
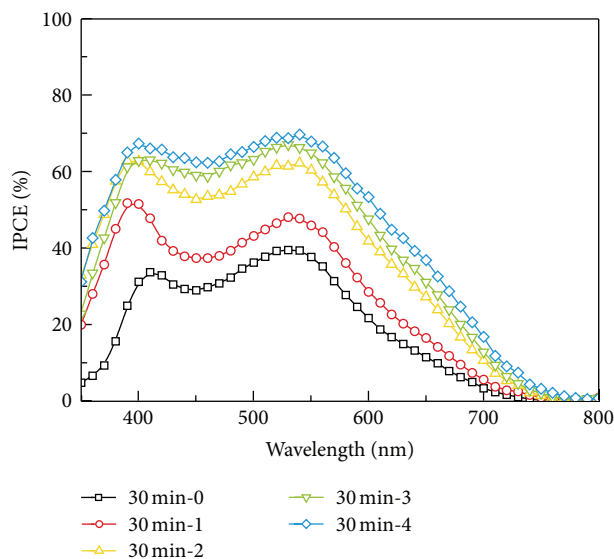
FIGURE 7: The incident photon-to-current conversion efficiency (IPCE) spectra of the TiO_2 hybrid architecture-based DSSCs with various $TiCl_3$ treatment times.

such as quantum-dot dye-sensitized solar cells (QD-DSSCs), photoelectrochemical (PEC) water-splitting, and solid-state solar cells, which require both high light harvesting and charge collection efficiencies.

Conflict of Interests

The authors declare that there is no conflict of interests regarding the publication of this paper.

Acknowledgment

References

[1] M. Grätzel, "Dye-sensitized solar cells," *Journal of Photochemistry and Photobiology C: Photochemistry Reviews*, vol. 4, no. 2, pp. 145–153, 2003.

[2] B. O'Regan and M. Graetzel, "A low-cost, high-efficiency solar cell based on dye-sensitized colloidal TiO_2 films," *Nature*, vol. 353, no. 6346, pp. 737–740, 1991.

[3] M. Grätzel, "Solar energy conversion by dye-sensitized photovoltaic cells," *Inorganic Chemistry*, vol. 44, no. 20, pp. 6841–6851, 2005.

[4] A. Yella, H.-W. Lee, H. N. Tsao et al., "Porphyrin-sensitized solar cells with cobalt (II/III)-based redox electrolyte exceed 12 percent efficiency," *Science*, vol. 334, no. 6056, pp. 629–634, 2011.

[5] T. P. Chou, Q. Zhang, G. E. Fryxell, and G. Cao, "Hierarchically structured ZnO film for dye-sensitized solar cells with enhanced energy conversion efficiency," *Advanced Materials*, vol. 19, no. 18, pp. 2588–2592, 2007.

[6] Q. Zhang, T. P. Chou, B. Russo, S. A. Jenekhe, and G. Cao, "Aggregation of ZnO nanocrystallites for high conversion efficiency in dye-sensitized solar cells," *Angewandte Chemie*, vol. 120, no. 13, pp. 2436–2440, 2008.

[7] J. Liu, T. Luo, S. Mouli T, F. Meng, B. Sun, and M. Li, "A novel coral-like porous SnO_2 hollow architecture: biomimetic swallowing growth mechanism and enhanced photovoltaic property for dye-sensitized solar cell application," *Chemical Communications*, vol. 46, no. 3, pp. 472–474, 2010.

[8] A. Kay and M. Grätzel, "Dye-sensitized core-shell nanocrystals: Improved efficiency of mesoporous tin oxide electrodes coated with a thin layer of an insulating oxide," *Chemistry of Materials*, vol. 14, no. 7, pp. 2930–2935, 2002.

[9] S. S. Shin, J. S. Kim, J. H. Suk et al., "Improved quantum efficiency of highly efficient perovskite $BaSnO_3$-based dye-sensitized solar cells," *ACS Nano*, vol. 7, no. 2, pp. 1027–1035, 2013.

[10] D. W. Kim, S. S. Shin, I. S. Cho et al., "Synthesis and photovoltaic property of fine and uniform Zn_2SnO_4 nanoparticles," *Nanoscale*, vol. 4, no. 2, pp. 557–562, 2012.

[11] J. H. Noh, H. S. Han, S. Lee et al., "Nanowire-based three-dimensional transparent conducting oxide electrodes for extremely fast charge collection," *Advanced Energy Materials*, vol. 1, no. 5, pp. 829–835, 2011.

[12] W.-Q. Wu, J.-Y. Liao, H.-Y. Chen, X.-Y. Yu, C.-Y. Su, and D.-B. Kuang, "Dye-sensitized solar cells based on a double layered TiO_2 photoanode consisting of hierarchical nanowire arrays and nanoparticles with greatly improved photovoltaic performance," *Journal of Materials Chemistry*, vol. 22, no. 34, pp. 18057–18062, 2012.

[13] B. Liu and E. S. Aydil, "Growth of oriented single-crystalline rutile TiO_2 nanorods on transparent conducting substrates for dye-sensitized solar cells," *Journal of the American Chemical Society*, vol. 131, no. 11, pp. 3985–3990, 2009.

[14] X. Feng, K. Zhu, A. J. Frank, C. A. Grimes, and T. E. Mallouk, "Rapid charge transport in dye-sensitized solar cells made from vertically aligned single-crystal rutile TiO_2 nanowires," *Angewandte Chemie International Edition*, vol. 51, no. 11, pp. 2727–2730, 2012.

[15] G. K. Mor, K. Shankar, M. Paulose, O. K. Varghese, and C. A. Grimes, "Use of highly-ordered TiO_2 nanotube arrays in dye-sensitized solar cells," *Nano Letters*, vol. 6, no. 2, pp. 215–218, 2006.

[16] J. R. Jennings, A. Ghicov, L. M. Peter, P. Schmuki, and A. B. Walker, "Dye-sensitized solar cells based on oriented TiO_2 nanotube arrays: transport, trapping, and transfer of electrons," *Journal of the American Chemical Society*, vol. 130, no. 40, pp. 13364–13372, 2008.

[17] S. Lee, I. J. Park, D. H. Kim et al., "Crystallographically preferred oriented TiO_2 nanotube arrays for efficient photovoltaic energy conversion," *Energy and Environmental Science*, vol. 5, no. 7, pp. 7989–7995, 2012.

[18] M. Law, L. E. Greene, J. C. Johnson, R. Saykally, and P. Yang, "Nanowire dye-sensitized solar cells," *Nature Materials*, vol. 4, no. 6, pp. 455–459, 2005.

[19] Y. Gao, M. Nagai, T.-C. Chang, and J.-J. Shyue, "Solution-derived ZnO nanowire array film as photoelectrode in dye-sensitized solar cells," *Crystal Growth and Design*, vol. 7, no. 12, pp. 2467–2471, 2007.

[20] S. H. Ko, D. Lee, H. W. Kang et al., "Nanoforest of hydrothermally grown hierarchical ZnO nanowires for a high efficiency

dye-sensitized solar cell," *Nano Letters*, vol. 11, no. 2, pp. 666–671, 2011.

[21] H. Wang, Y. Bai, Q. Wu et al., "Rutile TiO_2 nano-branched arrays on FTO for dye-sensitized solar cells," *Physical Chemistry Chemical Physics*, vol. 13, no. 15, pp. 7008–7013, 2011.

[22] W.-P. Liao and J.-J. Wu, "Wet chemical route to hierarchical TiO_2 nanodendrite/ nanoparticle composite anodes for dye-sensitized solar cells," *Journal of Materials Chemistry*, vol. 21, no. 25, pp. 9255–9262, 2011.

[23] F. Shao, J. Sun, L. Gao, S. Yang, and J. Luo, "Forest-like TiO_2 hierarchical structures for efficient dye-sensitized solar cells," *Journal of Materials Chemistry*, vol. 22, no. 14, pp. 6824–6830, 2012.

[24] I. S. Cho, Z. Chen, A. J. Forman et al., "Branched TiO_2 nanorods for photoelectrochemical hydrogen production," *Nano Letters*, vol. 11, no. 11, pp. 4978–4984, 2011.

[25] H. S. Jung, J.-K. Lee, B. S. Kang, Q. Jia, and M. Nastasi, "Strain relaxation in sol-gel grown epitaxial anatase thin films," *The Journal of Physical Chemistry C*, vol. 112, no. 11, pp. 4205–4208, 2008.

[26] E. Hosono, S. Fujihara, K. Kakiuchi, and H. Imai, "Growth of submicrometer-scale rectangular parallelepiped rutile TiO_2 films in aqueous $TiCl_3$ solutions under hydrothermal conditions," *Journal of the American Chemical Society*, vol. 126, no. 25, pp. 7790–7791, 2004.

[27] H. Cheng, J. Ma, Z. Zhao, and L. Qi, "Hydrothermal preparation of uniform nanosize rutile and anatase particles," *Chemistry of Materials*, vol. 7, no. 4, pp. 663–671, 1995.

[28] H. Perron, C. Domain, J. Roques, R. Drot, E. Simoni, and H. Catalette, "Optimisation of accurate rutile TiO_2 (110), (100), (101) and (001) surface models from periodic DFT calculations," *Theoretical Chemistry Accounts*, vol. 117, no. 4, pp. 565–574, 2007.

[29] S. Lee, I.-S. Cho, J. H. Lee et al., "Two-step sol-gel method-based TiO_2 nanoparticles with uniform morphology and size for efficient photo-energy conversion devices," *Chemistry of Materials*, vol. 22, no. 6, pp. 1958–1965, 2010.

[30] J. Nelson, S. A. Hague, D. R. Klug, and J. R. Durrant, "Trap-limited recombination in dye-sensitized nanocrystalline metal oxide electrodes," *Physical Review B*, vol. 63, no. 20, Article ID 205321, 9 pages, 2001.

[31] J. van de Lagemaat and A. J. Frank, "Nonthermalized electron transport in dye-sensitized nanocrystalline TiO_2 films: transient photocurrent and random-walk modeling studies," *The Journal of Physical Chemistry B*, vol. 105, no. 45, pp. 11194–11205, 2001.

[32] Q. Wang, J.-E. Moser, and M. Grätzel, "Electrochemical impedance spectroscopic analysis of dye-sensitized solar cells," *The Journal of Physical Chemistry B*, vol. 109, no. 31, pp. 14945–14953, 2005.

[33] D. Hwang, D. Y. Kim, and S. Y. Jang, "Superior photoelectrodes for solid-state dye-sensitized solar cells using amphiphilic TiO_2," *Journal of Materials Chemistry A*, vol. 1, no. 4, pp. 1228–1238, 2013.

[34] J.-H. Yum, S.-R. Jang, R. Humphry-Baker et al., "Effect of coadsorbent on the photovoltaic performance of zinc pthalocyanine-sensitized solar cells," *Langmuir*, vol. 24, no. 10, pp. 5636–5640, 2008.

Research Article

Synthesis and Photocatalytic Activity of Ag$_3$PO$_4$ Triangular Prism

Pengyu Dong,[1] Yan Hao,[2] Peiyang Gao,[2] Entian Cui,[1] and Qinfang Zhang[1]

[1]*Key Laboratory for Advanced Technology in Environmental Protection of Jiangsu Province, Yancheng Institute of Technology, Yancheng 224051, China*
[2]*School of Materials Engineering, Yancheng Institute of Technology, Yancheng 224051, China*

Correspondence should be addressed to Pengyu Dong; dongpy11@gmail.com

Ag$_3$PO$_4$ triangular prism was synthesized by a facile chemical precipitation approach by simply adjusting external ultrasonic condition. The as-synthesized Ag$_3$PO$_4$ triangular prism was characterized by X-ray diffraction pattern (XRD), field emission scanning electron microscopy (SEM), fourier transform infrared (FTIR) spectra, and ultraviolet-visible diffuse reflectance (UV-vis DRS) absorption spectra. The photocatalytic activity of Ag$_3$PO$_4$ triangular prism was evaluated by photodegradation of organic methylene blue (MB), rhodamine B (RhB), and phenol under visible light irradiation. Results showed that Ag$_3$PO$_4$ triangular prism exhibited higher photocatalytic activity than N-doped TiO$_2$ and commercial TiO$_2$ (P25) under visible light irradiation.

1. Introduction

Photocatalysis technology is considered as an efficient, stable, and environmentally friendly method for controlling environmental pollutions [1]. In the past years, the discovery of new efficient visible-light-driven photocatalysts attracts much attention. It is noted that a breakthrough on visible-light-driven photocatalysts was made by Yi et al.'s research team, who reported the use of Ag$_3$PO$_4$ as an active visible-light-driven photocatalyst for oxidation of water and photodecomposition of organic compounds [2]. This research finding is considered as a breakthrough in the field of visible-light active photocatalysts. Hence, investigation of the basic principles and application of Ag$_3$PO$_4$ photocatalyst is a hot topic. Up to now, various methods have been proposed to further enhance the visible-light-driven photocatalytic activity. One of the methods is the coupling of Ag$_3$PO$_4$ with other semiconductors or noble metals to promote the charge separation efficiency of Ag$_3$PO$_4$ and then enhancing of the photocatalytic activity. Some composite samples such as Ag$_3$PO$_4$/TiO$_2$ [3], AgBr@Ag$_3$PO$_4$/Fe$_3$O$_4$ [4], Ag$_3$PO$_4$/graphene oxide [5], Ag$_3$PO$_4$/TiOF$_2$ [6], Ag$_3$PO$_4$/Ag

[7], Ag$_3$PO$_4$/ZnO [8], Ag$_3$PO$_4$/BiOCl [9], Ag$_3$PO$_4$/reduced graphite oxide sheets [10], and g-C$_3$N$_4$/Ag$_3$PO$_4$ [11] have recently been developed to enhance the photocatalytic activity of Ag$_3$PO$_4$. Another method is the synthesis of Ag$_3$PO$_4$ with various new morphologies. In addition, it is known that the morphologies and microstructures of functional materials affect the physical and chemical properties [12, 13]. The morphology control of photocatalysts was considered to be one of the most promising avenues to improve the photocatalytic properties [14]. Therefore, further studies on Ag$_3$PO$_4$ crystals with new morphologies and structures will be of great value. In recent years, some morphologies of Ag$_3$PO$_4$ have been reported [15–21]. For example, Bi et al. fabricated the single-crystalline Ag$_3$PO$_4$ rhombic dodecahedrons with {110} facets exposed and cubes bounded entirely by {100} facets, and they found that both of these samples exhibited higher photocatalytic activity than the microsized spherical Ag$_3$PO$_4$ particles [15]. Our research group prepared Ag$_3$PO$_4$ nanorods with enhanced photocatalytic activity [16]. Wang et al. synthesized the tetrahedral Ag$_3$PO$_4$ crystals exposed with {111} facets [17]. Liang et al. synthesized hierarchical Ag$_3$PO$_4$ porous microcubes with enhanced photocatalytic
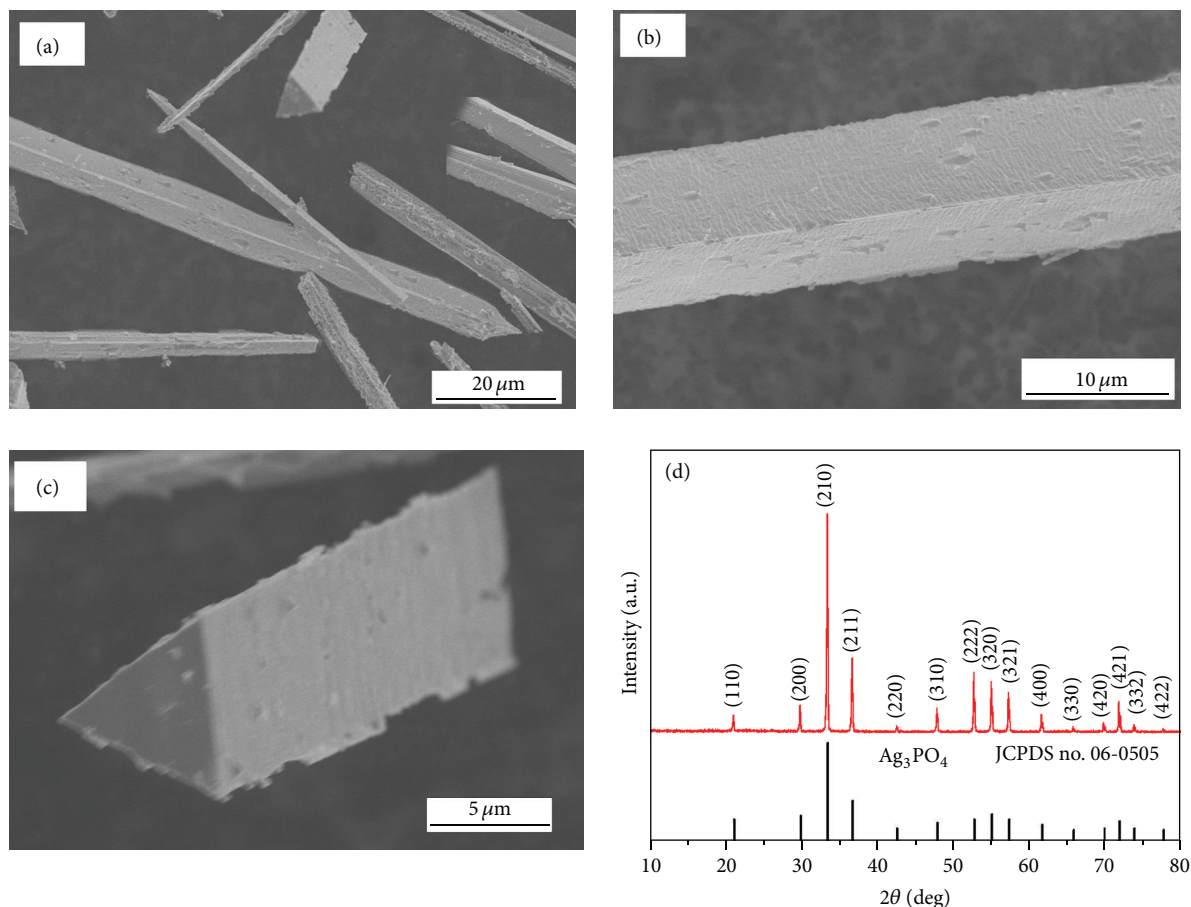
FIGURE 1: (a)–(c) SEM images and (d) XRD pattern of as-prepared Ag_3PO_4 sample.

property [18]. Up to now, synthesis of Ag_3PO_4 crystals with novel morphologies or microstructures is still an important and challenging research field.

To the best of our knowledge, there is no research on the synthesis of Ag_3PO_4 triangular prism. Herein, we controllably prepared Ag_3PO_4 triangular prism via a facile and efficient synthesis process in the mixture solvent of DMF and H_2O at room temperature. Meanwhile, the photocatalytic activity was investigated in this paper.

2. Experimental

In a typical preparation procedure, 10 mL of N,N-dimethylformamide (DMF) and 10 mL of deionized water (H_2O) were mixed together to form transparent solvent. Then, 3 mmol of $AgNO_3$ was dissolved into the mixture solvent. Subsequently, H_3PO_4 (1 mL, 85%) was added dropwise into the above solution under ultrasonic condition (ultrasonic reactor, KQ-100B, 40 kHz, 120 W/cm^2, Kunshan Co., China). After this process, the ultrasonic condition was maintained for 4 h. The obtained precipitation was separated by centrifuge and followed by washing with ethanol and deionized water for 3 times, respectively, to remove the DMF and other residues. Finally, the product was dried at 60°C. For comparison purpose, N-doped TiO_2 was synthesized by a reported

method [22]. The commercial TiO_2 (P25) was purchased from Degussa.

X-ray diffraction (XRD) experiment was carried out with a D/max-2400 diffractometer (Rigaku, Japan) using Cu-Ka radiation. The morphologies of the sample were examined by scanning electron microscopy (SEM, Hitachi S-4800). Fourier transform infrared (FTIR) spectrum of the sample was recorded between 400 and 4000 cm^{-1} on a Nicolet NEXUS 670 FTIR spectrometer. Ultraviolet-visible diffuse reflectance (UV-vis DRS) absorption spectrum was measured using a Perkin Elmer 950 spectrometer, while $BaSO_4$ was used as a reference.

The photocatalytic activity of sample was measured by decomposition of methylene blue (MB) and rhodamine B (RhB) in a reactor at room temperature. In a typical process for degradation of a dye, 50 mg of photocatalyst was suspended in the dye solution (10 mg/L, 60 mL). Before irradiation, the suspensions were stirred in the dark for 60 min to ensure the establishment of adsorption-desorption equilibrium. A 350 W Xe lamp with a cutoff filter of 420 nm was employed for the visible-light irradiation source and positioned 20 cm away from the reactor to trigger the photocatalytic reaction. A certain volume of suspension was withdrawn at selected times for analysis. After recovering the photocatalyst by centrifugation, the concentration of dye

(a)

(b)
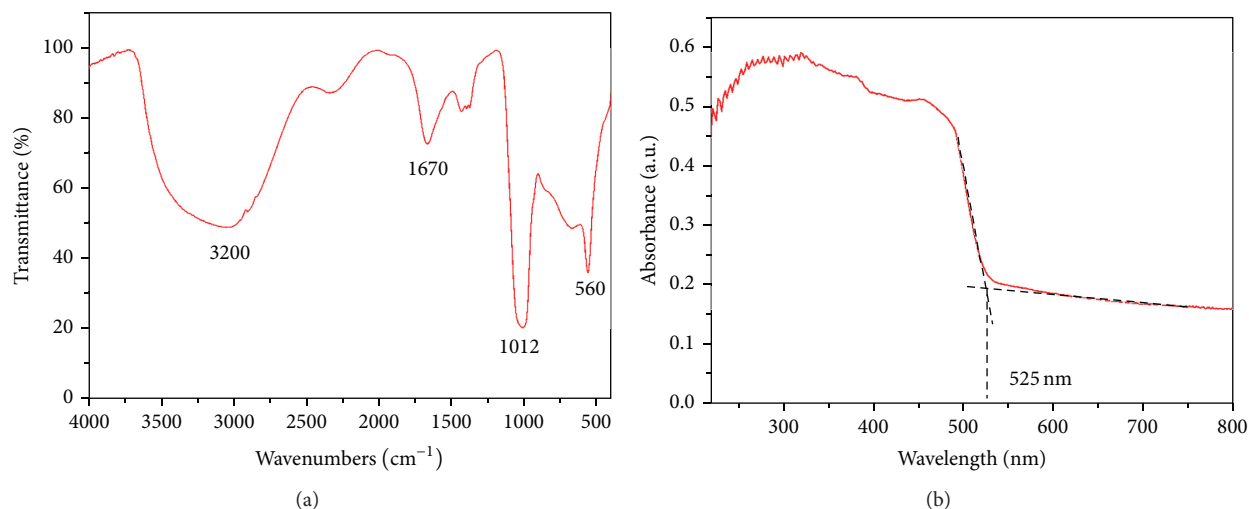
FIGURE 2: (a) FTIR spectrum of Ag_3PO_4 triangular prism in the regions of 4000–400 cm^{-1}, (b) UV-vis diffuse reflectance absorption spectrum of Ag_3PO_4 triangular prism.

solution was analyzed by measuring the light absorption of the clear solution at 664 nm (λ_{max} for MB solution) or 555 nm (λ_{max} for RhB solution) using a Perkin Elmer 950 spectrometer. The percentage of degradation was calculated by C/C_0. Here, C is the concentration of remaining dye solution at each irradiated time interval, while C_0 is the initial concentration. Furthermore, a colorless compound, phenol, was also chosen as a model pollutant since phenol shows no absorption in the visible region. The concentration of phenol solution was analyzed by measuring the light absorption of the clear solution at 270 nm (λ_{max} for phenol solution).

To test the stability of Ag_3PO_4 triangular prism, the cycling runs in photocatalytic degradation of MB in the presence of Ag_3PO_4 triangular prism were measured. After one cycle, the photocatalyst was filtrated and washed thoroughly with deionized water, and then fresh MB solution (10 mg/L) was added to the photocatalyst to begin the next cycling run. Five consecutive cycles were completed and each cycle lasted for 60 min.

3. Results and Discussion

The SEM images of as-prepared sample were displayed in Figures 1(a)–1(c). It is observed that more than 80% of the product could be assigned to the triangular-prism-shaped morphology in this sample. Moreover, the lengths of bottom and chamfered edges are up to several micrometers. The XRD pattern of as-prepared triangular-prism-shaped sample was shown in Figure 1(d). All the diffraction peaks could be indexed to the cubic Ag_3PO_4 phase (JCPDS number 06-0505). Combining the SEM results, a conclusion that Ag_3PO_4 triangular prism was obtained can be drawn. The synthesis mechanisms of Ag_3PO_4 triangular prism could be explained as follows: the ultrasound assisted method could accelerate solid particles to high velocities via creating cavitation and shock waves, which leads to interparticle collision and effective fusion at the point of collision [23, 24]. This kinetic
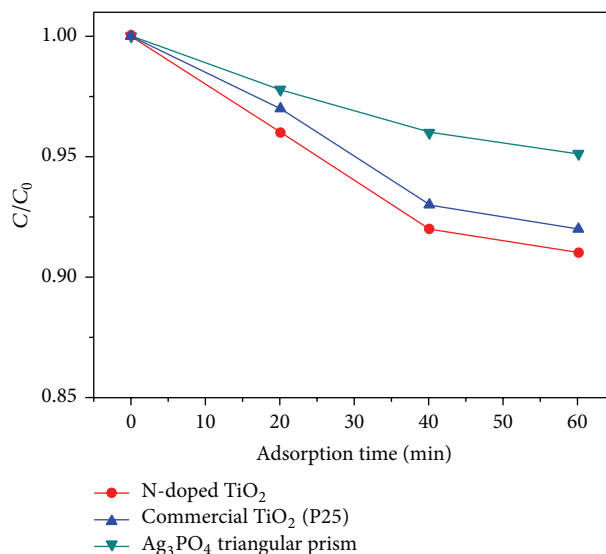
FIGURE 3: MB adsorption as a function of adsorption time over the as-prepared Ag_3PO_4 triangular prism, N-doped TiO_2, and commercial TiO_2 (P25) under a dark condition.

process speeds up the diffusion of Ag_3PO_4 nuclei in the reaction system, resulting in the formation of unique triangular-prism-shaped morphology, which can be attributed to the Ostwald ripening progress.

The chemical compositions of as-prepared Ag_3PO_4 triangular prism were examined by means of FTIR method. Figure 2(a) shows the FTIR spectrum of Ag_3PO_4 triangular prism. A strong and broad absorption around 3200 cm^{-1} and a sharp band at 1670 cm^{-1} are observed, which could be attributed to the stretching vibration of O–H and the bending vibration of H–O–H of residual water molecules, respectively. Besides that, two strong absorption bands are observed at 1012 and 560 cm^{-1}, which can be assigned to the molecular

(a)

(b)

(c)
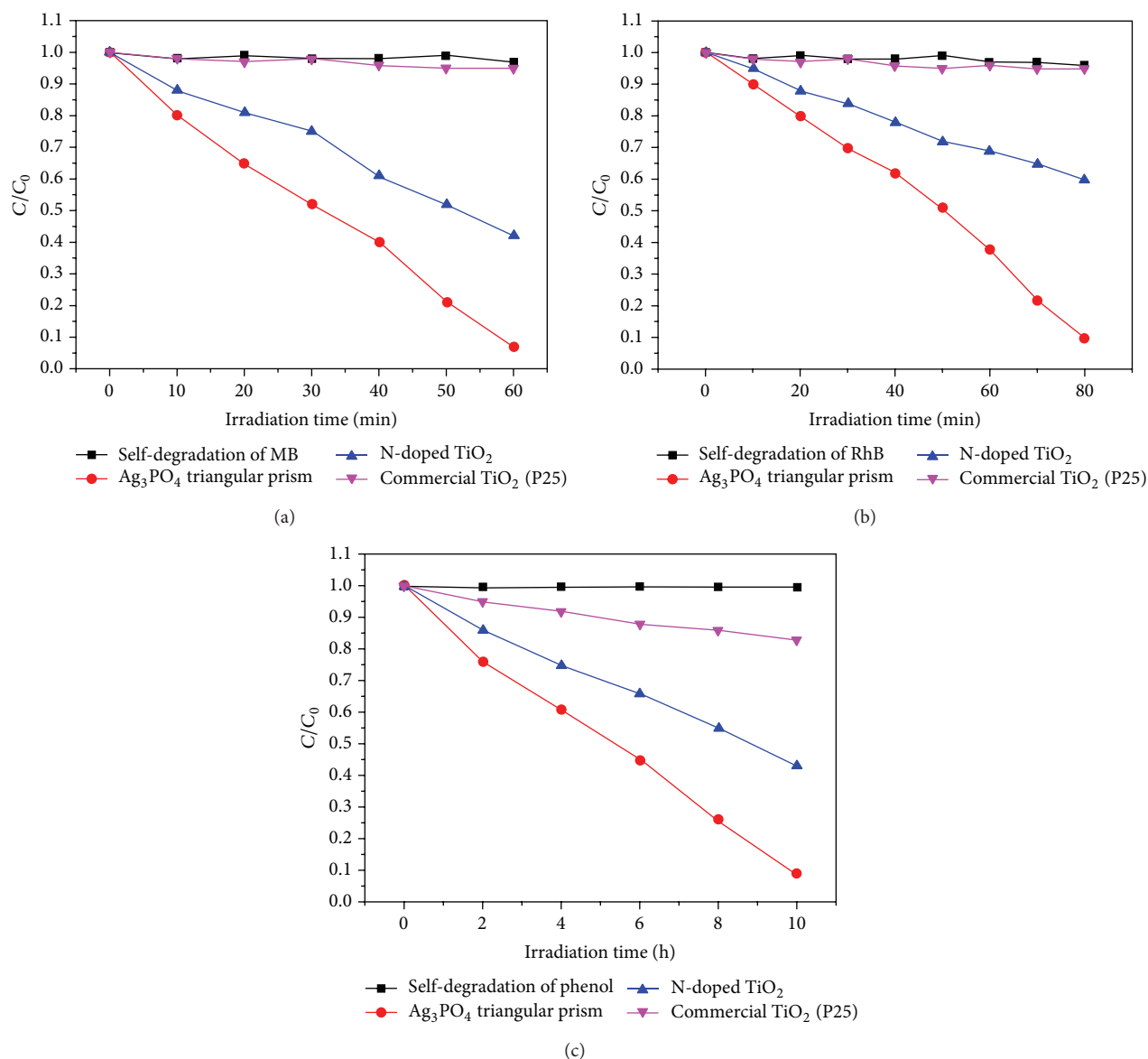
FIGURE 4: Variation of (a) MB, (b) RhB, and (c) phenol solution concentration against illumination time in the presence of Ag_3PO_4 triangular prism, N-doped TiO_2, and commercial TiO_2 (P25) under visible-light irradiation.

vibrations of phosphate (PO_4^{3-}) [25, 26]. This result confirms that there are no DMF molecules adsorbed on the surfaces of Ag_3PO_4 triangular prism. The UV-vis absorption spectrum of as-prepared Ag_3PO_4 triangular prism is displayed in Figure 2(b). It reveals that the absorption edge of Ag_3PO_4 triangular prism is around 525 nm, which means that it could strongly absorb a large part of visible light (400–525 nm).

Figure 3 shows the adsorption-desorption isotherms of as-prepared Ag_3PO_4 triangular prism, N-doped TiO_2, and commercial TiO_2 (P25) in the dark. It is found that most of the adsorption of dyes occur within 40 min, and the adsorption-desorption equilibrium can be achieved within 60 min. Moreover, it is observed that the adsorption affinity follows the order N-doped TiO_2 > commercial TiO_2 (P25) > Ag_3PO_4 triangular prism. Clearly, the Ag_3PO_4 triangular

prism shows lower adsorption affinity for MB compared to the N-doped TiO_2 and commercial TiO_2 (P25), which could be associated with the size of samples. The size of Ag_3PO_4 triangular prism is around several micrometers, while the size of N-doped TiO_2 and commercial TiO_2 (P25) is about 20~50 nanometers. Larger size of Ag_3PO_4 triangular prism leads to the poor adsorption of MB molecules on the surfaces of Ag_3PO_4 triangular prism, resulting in the lower adsorption affinity.

The photocatalytic activity of samples was then investigated after reaching the adsorption-desorption equilibrium in the dark. Figure 4 shows the photocatalytic degradation behavior. From Figures 4(a) and 4(b), it can be seen that self-degradation of MB and RhB was not obvious under visible-light irradiation, indicating that MB and RhB can be used as

the targeted pollutants. It is noted that the percentage of photocatalytic degradation of MB for Ag_3PO_4 triangular prism, N-doped TiO_2, and commercial TiO_2 (P25) is 93%, 58%, and 5%, respectively. Accordingly, the percentage of photocatalytic degradation of RhB for Ag_3PO_4 triangular prism, N-doped TiO_2, and commercial TiO_2 (P25) is 90%, 40%, and 5%, respectively. Therefore, the percentage of photocatalytic degradation of MB and RhB for the samples follows the following order: Ag_3PO_4 triangular prism > N-doped TiO_2 > commercial TiO_2 (P25). This result clearly indicates that the Ag_3PO_4 triangular prism shows higher photocatalytic activity under visible-light irradiation, which could attribute to the strong visible-light absorption of Ag_3PO_4 triangular prism. In contrast, N-doped TiO_2 could absorb a small part of visible light, and commercial TiO_2 (P25) cannot make use of visible light because of a large band gap (3.2 eV). Since the MB and RhB dyes may absorb visible light, the sensitization possibility for samples should be considered. Then, the photocatalytic activity of the samples was also evaluated by colorless phenol degradation to ensure the visible-light photocatalytic activity and exclude the dye sensitization under visible light. The degradation of phenol with Ag_3PO_4 triangular prism, N-doped TiO_2, and commercial TiO_2 (P25) under visible-light irradiation was presented in Figure 4(c). It is clear that the concentration of phenol decreases with the irradiation time. Moreover, the Ag_3PO_4 triangular prism sample shows slightly higher photocatalytic activity for colorless phenol degradation compared to N-doped TiO_2 and commercial TiO_2 (P25).

The enhanced photocatalytic activity of Ag_3PO_4 triangular prism could be ascribed to the optical absorption property and unique electronic structure of Ag_3PO_4 crystals. Since the optical absorption edge of Ag_3PO_4 triangular prism is around 525 nm, the sample of Ag_3PO_4 triangular prism could strongly absorb a large part of visible light (400–525 nm). In addition, the highest valence band edge potential of Ag_3PO_4 crystals is 2.67 V (versus normal hydrogen electrode), which has strong driving force for photocatalytic degradation of pollutants [27].

The photocatalytic stability of Ag_3PO_4 triangular prism was shown in Figure 5. It is observed that the photocatalytic activity of Ag_3PO_4 triangular prism is decreased slowly in five successive experimental runs. This result indicates that the photocatalytic activity of Ag_3PO_4 triangular prism is unstable, which needs to be improved in the later study.

4. Conclusions

A new morphology, Ag_3PO_4 triangular prism, was successfully synthesized in the mixture solvent of DMF and H_2O under ultrasonic condition within 4 h. This synthetic method does not need the assistance of any hard/soft template. Although the Ag_3PO_4 triangular prism shows lower adsorption affinity for MB molecules, the photocatalytic results indicate that Ag_3PO_4 triangular prism shows enhanced photocatalytic activity compared with N-doped TiO_2 and commercial TiO_2 (P25). In addition, the photocatalytic stability of Ag_3PO_4 triangular prism needs to be further improved by various methods in the later study.
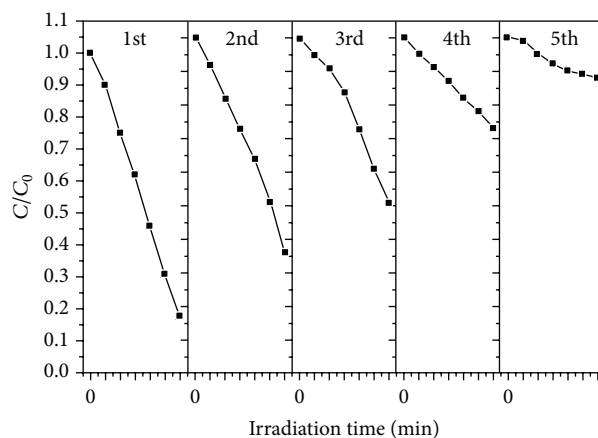
FIGURE 5: Repeated photocatalytic degradation of MB solution in the presence of Ag_3PO_4 triangular prism under visible-light irradiation.

Conflict of Interests

The authors declare that there is no conflict of interests regarding the publication of this paper.

Acknowledgments

References

[1] G.-F. Huang, Z.-L. Ma, W.-Q. Huang et al., "Ag_3PO_4 semiconductor photocatalyst: possibilities and challenges," *Journal of Nanomaterials*, vol. 2013, Article ID 371356, 8 pages, 2013.

[2] Z. Yi, J. Ye, N. Kikugawa et al., "An orthophosphate semiconductor with photooxidation properties under visible-light irradiation," *Nature Materials*, vol. 9, no. 7, pp. 559–564, 2010.

[3] W. Yao, B. Zhang, C. Huang, C. Ma, X. Song, and Q. Xu, "Synthesis and characterization of high efficiency and stable Ag_3PO_4/TiO_2 visible light photocatalyst for the degradation of methylene blue and rhodamine B solutions," *Journal of Materials Chemistry*, vol. 22, no. 9, pp. 4050–4055, 2012.

[4] Z. Wang, L. Yin, Z. W. Chen, G. W. Zhou, and H. X. Shi, "Photodegradation of methyl orange using magnetically recoverable AgBr@Ag_3PO_4/Fe_3O_4 photocatalyst under visible light," *Journal of Nanomaterials*, vol. 2014, Article ID 150150, 6 pages, 2014.

[5] Z. Xiu, Y. Wu, X. Hao, Q. Lu, and S. Liu, "Graphene oxide wrapped Ag_3PO_4 sub-microparticles with highly enhanced photocatalytic activity and stability under visible light irradiation," *Materials Research Bulletin*, vol. 59, pp. 192–198, 2014.

[6] P. Dong, E. Cui, G. Hou, R. Guan, and Q. Zhang, "Synthesis and photocatalytic activity of Ag_3PO_4/$TiOF_2$ composites with enhanced stability," *Materials Letters*, vol. 143, pp. 20–23, 2015.

[7] Y. Bi, H. Hu, S. Ouyang, Z. Jiao, G. Lu, and J. Ye, "Selective growth of Ag_3PO_4 submicro-cubes on Ag nanowires to fabricate necklace-like heterostructures for photocatalytic applications," *Journal of Materials Chemistry*, vol. 22, no. 30, pp. 14847–14850, 2012.

[8] W. Liu, M. Wang, C. Xu, S. Chen, and X. Fu, "Ag_3PO_4/ZnO: an efficient visible-light-sensitized composite with its application in photocatalytic degradation of Rhodamine B," *Materials Research Bulletin*, vol. 48, no. 1, pp. 106–113, 2013.

[9] B. C. Cao, P. Y. Dong, S. Cao, and Y. H. Wang, "BiOCl/Ag_3PO_4 composites with highly enhanced ultraviolet and visible light photocatalytic performances," *Journal of the American Ceramic Society*, vol. 96, no. 2, pp. 544–548, 2013.

[10] P. Dong, Y. Wang, B. Cao et al., "Ag_3PO_4/reduced graphite oxide sheets nanocomposites with highly enhanced visible light photocatalytic activity and stability," *Applied Catalysis B: Environmental*, vol. 132-133, pp. 45–53, 2013.

[11] P. He, L. Song, S. Zhang, X. Wu, and Q. Wei, "Synthesis of g-C_3N_4/Ag_3PO_4 heterojunction with enhanced photocatalytic performance," *Materials Research Bulletin*, vol. 51, pp. 432–437, 2014.

[12] P. Hu, L. Yu, A. Zuo, C. Guo, and F. Yuan, "Fabrication of Monodisperse magnetite hollow spheres," *The Journal of Physical Chemistry C*, vol. 113, no. 3, pp. 900–906, 2009.

[13] P. Hu, X. Zhang, N. Han, W. Xiang, Y. Cao, and F. Yuan, "Solution-controlled self-assembly of ZnO nanorods into hollow microspheres," *Crystal Growth & Design*, vol. 11, no. 5, pp. 1520–1526, 2011.

[14] Y. Cao, J. Fan, L. Bai, F. Yuan, and Y. Chen, "Morphology evolution of Cu_2O from octahedra to hollow structures," *Crystal Growth & Design*, vol. 10, no. 1, pp. 232–236, 2010.

[15] Y. Bi, S. Ouyang, N. Umezawa, J. Cao, and J. Ye, "Facet effect of single-crystalline Ag3PO4 sub-microcrystals on photocatalytic properties," *Journal of the American Chemical Society*, vol. 133, no. 17, pp. 6490–6492, 2011.

[16] P. Dong, J. Hu, Y. Huang, E. Cui, and G. Hou, "Synthesis of Ag_3PO_4 nanorods with enhanced photocatalytic activity," *Energy and Environment Focus*, vol. 4, pp. 1–5, 2015.

[17] H. Wang, Y. Bai, J. Yang, X. Lang, J. Li, and L. Guo, "A facile way to rejuvenate Ag_3PO_4 as a recyclable highly efficient photocatalyst," *Chemistry*, vol. 18, no. 18, pp. 5524–5529, 2012.

[18] Q. Liang, W. Ma, Y. Shi, Z. Li, and X. Yang, "Hierarchical Ag_3PO_4 porous microcubes with enhanced photocatalytic properties synthesized with the assistance of trisodium citrate," *CrystEngComm*, vol. 14, no. 8, pp. 2966–2973, 2012.

[19] Z.-M. Yang, Y.-Y. Liu, L. Xu, G.-F. Huang, and W.-Q. Huang, "Facile shape-controllable synthesis of Ag_3PO_4 photocatalysts," *Materials Letters*, vol. 133, pp. 139–142, 2014.

[20] X.-Z. Li, K.-L. Wu, C. Dong, S.-H. Xia, Y. Ye, and X.-W. Wei, "Size-controlled synthesis of Ag_3PO_4 nanorods and their high-performance photocatalysis for dye degradation under visible-light irradiation," *Materials Letters*, vol. 130, pp. 97–100, 2014.

[21] P. Dong, Y. Yin, N. Xu, R. Guan, G. Hou, and Y. Wang, "Facile synthesis of tetrahedral Ag_3PO_4 mesocrystals and its enhanced photocatalytic activity," *Materials Research Bulletin*, vol. 60, pp. 682–689, 2014.

[22] R. Asahi, T. Morikawa, T. Ohwaki, K. Aoki, and Y. Taga, "Visible-light photocatalysis in nitrogen-doped titanium oxides," *Science*, vol. 293, no. 5528, pp. 269–271, 2001.

[23] L. Zhu, X. Liu, J. Meng, and X. Cao, "Facile sonochemical synthesis of single-crystalline europium fluorine with novel nanostructure," *Crystal Growth and Design*, vol. 7, no. 12, pp. 2505–2511, 2007.

[24] J. H. Bang and K. S. Suslick, "Applications of ultrasound to the synthesis of nanostructured materials," *Advanced Materials*, vol. 22, no. 10, pp. 1039–1059, 2010.

[25] L. M. Miller, V. Vairavamurthy, M. R. Chance et al., "In situ analysis of mineral content and crystallinity in bone using infrared micro-spectroscopy of the ν_4 PO_4^{3-} vibration," *Biochimica et Biophysica Acta—General Subjects*, vol. 1527, no. 1-2, pp. 11–19, 2001.

[26] S. J. Gadaleta, E. P. Paschalis, F. Betts, R. Mendelsohn, and A. L. Boskey, "Fourier transform infrared spectroscopy of the solution-mediated conversion of amorphous calcium phosphate to hydroxyapatite: new correlations between X-ray diffraction and infrared data," *Calcified Tissue International*, vol. 58, no. 1, pp. 9–16, 1996.

[27] J. J. Liu, X. L. Fu, S. F. Chen, and Y. F. Zhu, "Electronic structure and optical properties of Ag_3PO_4 photocatalyst calculated by hybrid density functional method," *Applied Physics Letters*, vol. 99, no. 19, Article ID 191903, 2011.

Review Article

Hybrid Organic-Inorganic Perovskites Open a New Era for Low-Cost, High Efficiency Solar Cells

Guiming Peng,[1,2,3] **Xueqing Xu,**[2] **and Gang Xu**[2]

[1]*Department of Chemical and Petroleum Engineering, University of Pittsburgh, Pittsburgh, PA 15261, USA*
[2]*CAS Key Laboratory of Renewable Energy, Guangzhou Institute of Energy Conversion, Chinese Academy of Sciences, Guangzhou 510640, China*
[3]*University of Chinese Academy of Sciences, Beijing 100049, China*

Correspondence should be addressed to Xueqing Xu; xuxq@ms.giec.ac.cn and Gang Xu; xugang@ms.giec.ac.cn

Received 12 October 2014; Revised 14 December 2014; Accepted 14 December 2014

Academic Editor: Cao Yuebin

The ramping solar energy to electricity conversion efficiencies of hybrid organic-inorganic perovskite solar cells during the last five years have opened new doors to low-cost solar energy. The record power conversion efficiency has climbed to 19.3% in August 2014 and then jumped to 20.1% in November. In this review, the main achievements for perovskite solar cells categorized from a viewpoint of device structure are overviewed. The challenges and prospects for future development of this field are also briefly presented.

1. Introduction

The energy crisis and environment pollution are two main worldwide challenges that would restrain the society development. Solar energy, as a clean and vast energy source, is widely believed to be a promising way to address these global issues. Converting solar energy into electricity is thought to be an effective way to harness this abundant energy source. To date, single-crystalline silicon solar cells have shown optimistic power conversion efficiency (PCE) above 24%. However, the cost of manufacturing process is still very high. Searching for low-cost materials with high PCE always attracts extensive efforts from the scientists.

Fortunately, the past five years have seen hybrid organic-inorganic perovskite solar cells (PSCs) performing promisingly on a low-cost avenue to the clean and vast solar energy. The ease of fabrication, abundant material source, and high PCE rapidly caught the attention of scientists.

PSCs first emerged as a liquid electrolyte based solar cell in 2009 with the PCE of only 3.8% [1]. However, perovskite was found to be unstable in liquid electrolyte [1, 2]. In 2012, solid-state dye-sensitized solar cell with a PCE of 10.2% [3], which was obtained by using tin containing perovskite $CsSnI_3$ as a cosensitizer and hole conductor, N719 as a sensitizer, and

the $CH_3NH_3PbI_3$ perovskite sensitized solar cell on Al_2O_3 scaffold with a PCE of 10.9% are the considerable millstone and herald the coming era of perovskite solar cells [4]. Since then, PSCs have been developed at an unprecedented rate. The PCEs of PSCs have evolved rapidly during the past five years. As shown in Figure 1(a), the PCE of perovskite had been boosted up to 15% in 2013 [5, 6]. Then a confirmed efficiency of 17.9% was achieved in early 2014 [7]. Subsequently, the PCE climbed to 19.3% by engineering the interface on a planar device [8, 9]. By November 2014, a new record certified nonstabilized efficiency of 20.1% was achieved by KRICT [10].

A schematic illustration of the crystal structure of perovskite is shown in Figure 1(b). The general formula for hybrid perovskites is ABX_3, where A is methyl ammonium, B is Pb(II) or Sn(II), and X is Cl, Br, or I, or a coexistence of several halogens. As an exciting material for solar cells, hybrid perovskites combine many in-built advantageous properties. As shown in Figure 2(d) [11], optical properties of perovskites can be tuned by varying the ratio between different halogen elements [11–13]. The most widely studied $CH_3NH_3PbI_3$ is a direct bandgap semiconductor with a bandgap of 1.55 eV, which determines its absorption offset up to 800 nm [14]. The weak photogenerated exciton binding energy of merely 0.03 eV facilitates the charge separation at
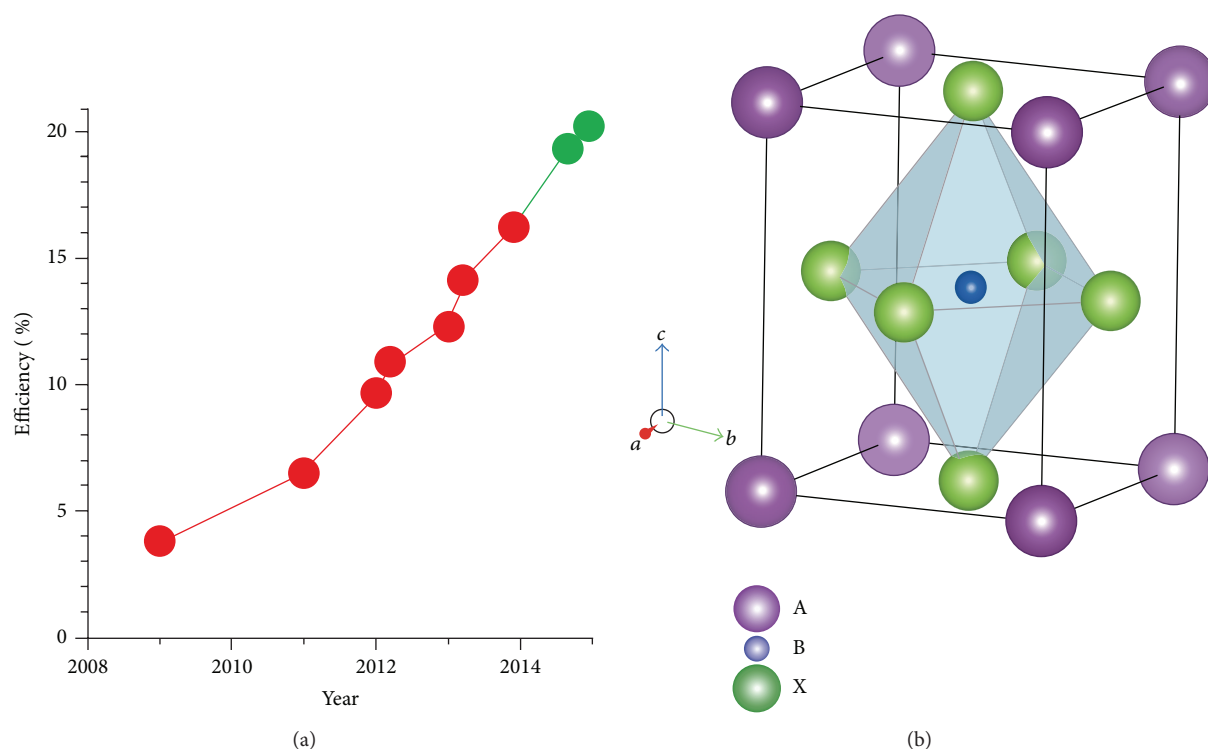
(a)

A

B

X

(b)

FIGURE 1: (a) PCE record plot of perovskite solar cells. Red plot is cited from the National Renewable Energy Laboratory (NREL) of the USA. Green PCE value is added according to [9, 10]. (b) Crystal structure of perovskite adopting the form of ABX_3, where A is methyl ammonium, B is Pb(II) or Sn(II), and X is Cl, Br, or I, or a coexistence of several halogen elements. Reprinted with permission from [5]. Copyright: Nature Publishing Group.

ambient temperature [15]. In addition, the small effective masses of electrons and holes generated in $CH_3NH_3PbI_3$ promote rapid transport of these carriers [16]. The lifetime of the carriers is in the hundreds of nanoseconds' range, leading to much slower recombination and much longer diffusion length from 100 nm to 1000 nm [15, 17, 18]. Apart from acting by light absorbing, hole-transporting material- (HTM-) free perovskite solar cell showing a PCE of 5.5% highlights the efficient hole-transporting ability of $CH_3NH_3PbI_3$ [19]. Furthermore, long range ambipolar charge transport was found in $CH_3NH_3PbI_3$ [20]. All these material properties make perovskites attractive for photovoltaic applications.

To date, each individual layer of organic-inorganic perovskite solar cells has been investigated and optimized intensively. As the rapid development of PSCs goes on, there is a strong demand for a summary of what achievements the scientists have realized. A summary is also necessary for looking forward to address the existing issues. In this review, we would like to overview the PSCs from the following aspects: perovskite synthesis methods, hole transport materials (HTMs), and photoanode morphologies. Some outlook and challenges for PSCs also will be briefly discussed.

2. Perovskite Synthesis and Optimization

Two synthesis methods of hybrid perovskite are widely used in solar cell applications. The precursor CH_3NH_3I is synthesized by reacting equimolar methylamine with hydroiodic acid under stirring at $0°C$ for 2 h. Rotary evaporation is often

used to recover the CH_3NH_3I from the reaction mixture. The recovered CH_3NH_3I is washed with diethyl ether.

For the one-step method, $CH_3NH_3PbI_3$ is synthesized by mixing equimolar CH_3NH_3I and PbI_2 in γ-butyrolactone, N,N-dimethylformamide (DMF), or dimethylsulfoxide (DMSO) at $60°C$ for 12 hours [2]. To synthesize the mixed halides containing perovskite, the ratios between CH_3NH_3I and PbX_2 are varied according to the target perovskite formula [4, 12]. So far, the most successful one-step method case is $CH_3NH_3PbI_{3-x}Cl_x$ which is well illustrated by Yang group with the cell PCE of 19.3% and is summarized in Figure 2(c) [9].

The two-step method, named sequential deposition as well, is a method similar to successive ionic layer adsorption and reaction method (SILAR) for quantum dot synthesis and was developed by Burschka et al. [6]. Typically in this method, PbI_2 is first dissolved in a solvent, such as N,N-dimethylformamide, under stirring at $70°C$. Then the photoanodes or substrates are spin-coated with the PbI_2 solution maintained at $70°C$, followed by drying at $70°C$ for 30 min. After cooling to room temperature, the films are dipped into a CH_3NH_3I solution (usually 10 mg/mL in 2-propanol) for 20 s and then rinsed with 2-propanol and dried at $70°C$ for 30 min [6].

Other novel synthesis methods have been attempted as well. For example, vacuum condition is employed to increase the perovskite purity and uniformity [13, 24]. Vacuum deposition, which involves evaporating and depositing organic

(a)

(b)

FIGURE 2: Continued.

(c)

(d)
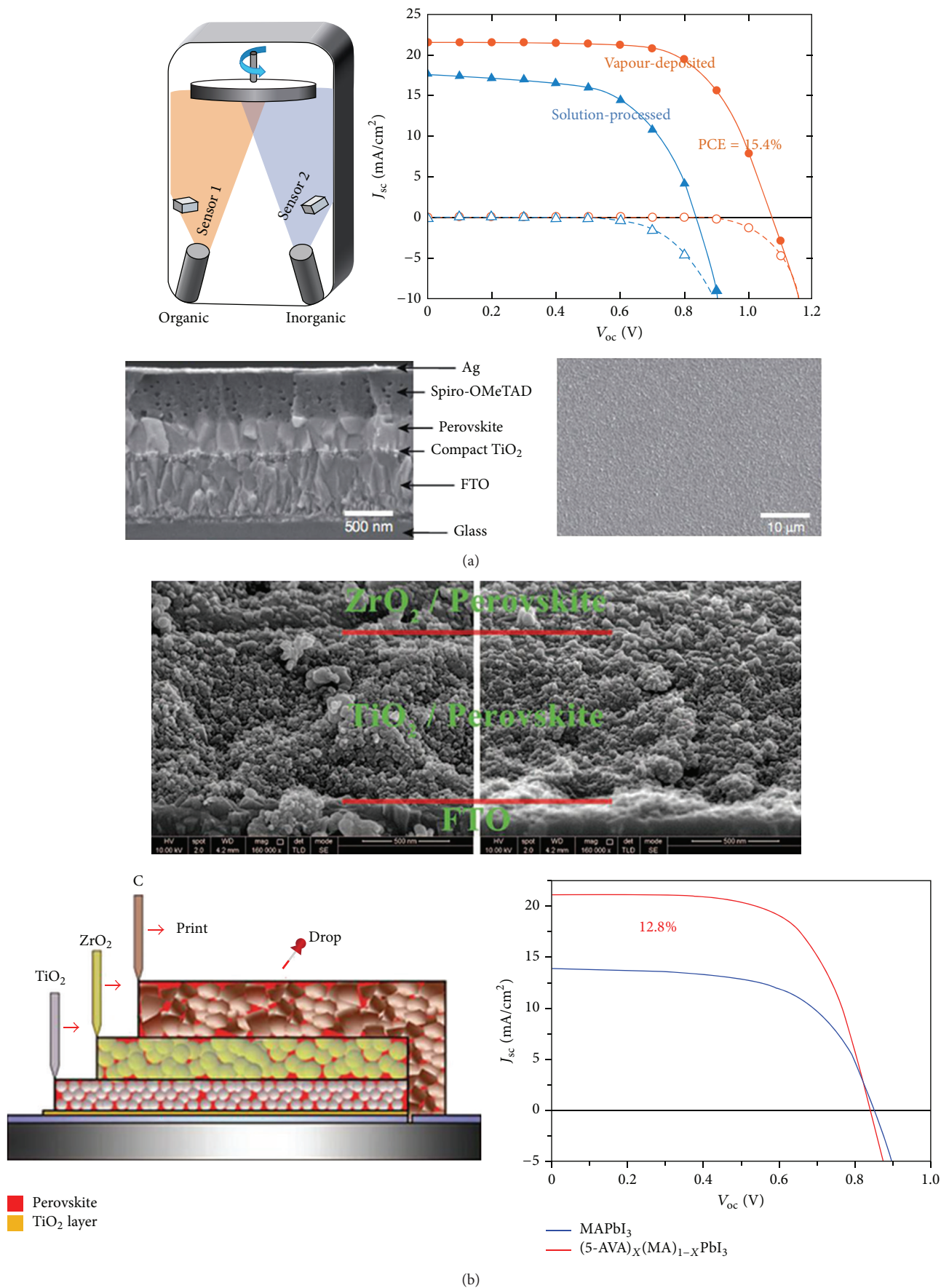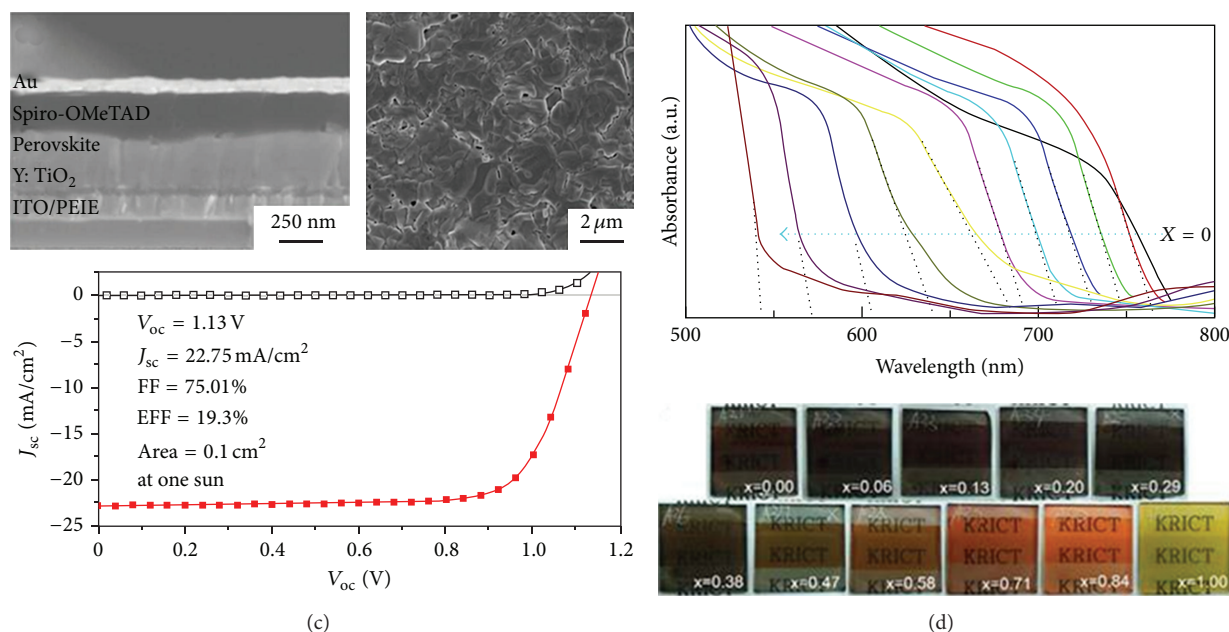
FIGURE 2: Perovskite synthesis methods and light absorption tuning. (a) Vapour deposition of $CH_3NH_3PbI_{3-x}Cl_x$. Reprinted from [5]. Copyright: Nature Publishing Group. (b) Mixed cation perovskite $((5\text{-}AVA)_x(MA)_{1-x}PbI_3)$ prepared by drop-casting a solution of PbI_2, methylammonium (MA) iodide, and 5-ammoniumvaleric acid (5-AVA) iodide onto a double layer of TiO_2 and ZrO_2 through a carbon film. Reproduced with permission from [21]. Copyright: Science. (c) Solution processed $CH_3NH_3PbI_{3-x}Cl_x$ with interface engineering. Reproduced with permission from [9]. Copyright: Science. (d) Colorful $CH_3NH_3Pb(I_{1-x}Br_x)_3$ obtained by tuning the chemical composition. Reprinted from [11]. Copyright: the American Chemical Society.

and inorganic sources to form perovskite, was introduced by Snaith et al. (Figure 2(a)). Such vapour-deposited planar device showed a PCE of 15.4%, which was higher than that of the solution deposited device, 8.6% [5]. In addition, planar device fabricated via a vapor-assisted solution processing generated a PCE of 12.1% by Yang group [25]. More recently, hybrid chemical vapour deposition was employed to synthesize perovskite. Such device yielded 19% PCE according to the report [26].

Due to the nature of perovskites, finding the optimal conditions and methods necessary to obtain a dense, uniform, and high quality perovskite film still remains a challenge. There are considerable efforts by different groups to optimize the deposition conditions for high quality perovskite films. For example, Carnie et al. codeposited an Al_2O_3/perovskite layer at $T < 110°C$ by adding 5% Al_2O_3 suspension to the $CH_3NH_3PbI_3$ precursor and a solar cell was fabricated with a PCE of 7.2% [27]. In order to improve the film quality and enhance light harvesting, three ways are attempted: firstly, doping other halide atoms into $CH_3NH_3PbI_3$ to improve its surface coverage and light absorption. By doping chlorine element into $CH_3NH_3PbI_3$ while fabricating a planar device, perovskite annealed at 95°C exhibited a PCE over 10% [28]. Colorful light absorbers based on $CH_3NH_3Pb(I_{1-x}Br_x)_3$ were synthesized by changing the I to Br ratio (Figure 2(d)). The cells using $CH_3NH_3Pb(I_{1-x}Br_x)_3$ with x value from 0 to 0.2 exhibited an average PCE of more than 10% and a maximum PCE of 12.3% [11]. Extremely uniform and dense

$CH_3NH_3Pb(I_{1-x}Br_x)_3$ ($x = 0.1$–0.15) film was obtained by using a mixed solvent of γ-butyrolactone and dimethyl-sulphoxide (DMSO) followed by a toluene drop-casting process when spin-coating the precursor solution [7]. Secondly, methylammonium group could be substituted by other moieties to change its bandgap and film evolution behavior [21, 29]. $NH_2CH=NH_2PbI_3$ with its bandgap of 1.4 eV showed 7.5% in PSC [29]. More recently, mixed organic cation perovskite was produced by drop-casting a solution of PbI_2, methylammonium (MA) iodide, and 5-ammoniumvaleric acid (5-AVA) iodide onto a double layer of TiO_2 and ZrO_2 through a carbon film. This structured PSC led to a more stable device (>1000 h) with a PCE of 12.8% (Figure 2(b)) [21]. The deep relationship between bandgap and substituents of MA was also investigated. The bandgap of $CsPbI_3$ is 1.67 eV [30]. The bandgap seems to gradually increase as the size of the substituents of methylammonium group increases [31]. Thirdly, light absorption onset of perovskites could also be tuned by substituting part of the toxic lead with other nontoxic metal elements. $CH_3NH_3Sn_{1-x}Pb_xI_3$ with series of different metal ratios were synthesized. Their bandgaps were located between 1.17 and 1.55 eV. Consequently, the light absorption could be extended from the visible region to the near-infrared region (~1060 nm), and finally the PSC using $CH_3NH_3Sn_{0.5}Pb_{0.5}I_3$ had a 4.18% PCE [32]. Moreover, lead-free solid-state perovskite solar cells based on $CH_3NH_3SnI_3$ as the light harvester were first reported by Hao et al. with a PCE of 5.73% [33].

3. HTMs for PSCs

HTMs, just as the name implies, transport the holes to the back electrode when the excitons are dissociated into electrons and holes. Apart from the fast hole transport rate, direct contact to the sensitizer allows HTMs to coexist with the sensitizer and not cause any sensitizer degradation.

3.1. Organic HTMs. The first PSCs adopted $CH_3NH_3PbI_3$ and $CH_3NH_3PbBr_3$ as the light absorber and LiI and I_2 containing methoxyacetonitrile as electrolyte. Such PSCs yielded PCEs of 3.8% and 3.1%, respectively [1]. However, perovskite was found to rapidly dissolve into the organic solvent. Much progress was achieved by changing the electrolyte composition and improving the perovskite deposition method. The resultant PSC achieved a PCE of 6.5%, but the devices still lasted for only several minutes [2]. To resolve this dissolution issue, scientists tried to replace liquid electrolyte with solid HTMs. Perovskite $CsSnI_{2.95}F_{0.05}$ was the first perovskite employed to act as both solid HTM and light absorber. Impressively, such PSC construct significantly lifted its PCE to 10.2% [3]. 2,2′,7,7′-Tetrakis-(N,N-dimethoxyphenyl-amine)-9,9′-spirobifluorene (spiro-OMeTAD) was incorporated with mesoporous TiO_2 and Al_2O_3, which showed PCE of 10.9% and generated open-circuit photovoltage up to 1.1 V [4, 34]. By electron coupling with fullerene monolayer on the surface of TiO_2, the device using poly(3-hexylthiophene-2,5-diyl) (P3HT) as HTM realized a PCE of 6.7%, while the device using spiro-OMeTAD as HTM output a PCE of 11.7% [35]. In addition, behaviors of three HTMs, spiro-OMeTAD, P3HT, and 4-(diethylamino)-benzaldehyde diphenylhydrazone (DEH), were compared in $CH_3NH_3PbI_3$ sensitized solar cells [36]. Hole transfer from $CH_3NH_3PbI_3$ to HTMs was observed after excitation of $CH_3NH_3PbI_3$. The electron lifetime in these devices was in the order spiro-OMeTAD > P3HT > DEH, while the charge transport time was similar. Besides, PSC incorporated with spiro-OMeTAD showed the best performances [36]. Tris[2-(1H-pyrazol-1-yl)-4-tert-butylpyridine) cobalt(III) tris(bis (trifluoromethylsulfonyl) imide)] as an additive in spiro-OMeTAD is believed to improve PSC PCE from 8.1% to 10.4% [37]. Moreover, several other organic HTMs were also employed with perovskite to fabricate PSCs. Poly(triarylamine) is another efficient organic HTM. PSCs of $CH_3NH_3PbI_3$ and $CH_3NH_3Pb(I_{1-x}Br_x)_3$ incorporated with poly(triarylamine) realized PCE over 12% [11, 20]. When using conjugated quinolizino acridine as HTM, $CH_3NH_3PbI_3$ sensitized TiO_2 mesoporous PSC output a better PCE of 12.8% than using spiro-OMeTAD as HTM [38]. With *o*-methoxy substituents in spiro-OMeTAD as HTM, planar PSC achieved PCE of 16.7% [39]. Carbazole derivatives were adopted as HTMs and fabricated with $CH_3NH_3PbI_3$ into PSC yielding a remarkable PCE of 14.79% [40].

3.2. Inorganic HTMs. However, the cost of organic HTMs is still high. Low-priced HTMs for reducing the cost of PSCs appear appealing. Compared to organic HTMs, inorganic HTMs are less expensive and attract less attention. PSCs using copper iodide realized a PCE over 6.0% but with an inferior V_{oc} of 0.55 V [41]. The small V_{oc} for the copper iodide based PSCs originated from the unfavorable bandgap. Copper thiocyanate is a more efficient HTM for PSCs. Qin et al. adopted copper thiocyanate to incorporate with $CH_3NH_3PbI_3$, and the device showed PCE of 12.4% [42]. Nickel oxide is another inorganic HTM due to its large bandgap and deep valance band (5.4 eV). NiO was employed as HTM and the corresponding PSC yielded a PCE of 7.3% [43]. PCE of 11.6% was obtained on a $NiO/CH_3NH_3PbI_3$ device via introducing NiO_x as electron blocking layer [44]. By employing NO as hole-collecting and hole-conducting layer, $CH_3NH_3PbI_3$ on planar NiO film output a PCE of 7.6% with the V_{oc} of 1.05 V [45]. By doping NiO_x thin film with copper, the hole transport ability of the resultant film increased remarkably. For the copper-doped NiO_x based PSCs, the environmental stability was much improved, and the PCE was impressively elevated to 15.40% [46].

3.3. HTM-Free PSCs. The device using Al_2O_3 as scaffold stimulated the deep thought of the property of $CH_3NH_3PbI_3$ [4]. Due to the larger band gap of Al_2O_3, it could not conduct electron from perovskite to the TiO_2 underlayer. The high device performance implies the high electron transport ability of the material [47, 48]. On the other hand, the HTM-free device that generated PCE of 5.5% confirmed the hole transport ability of the perovskite [19]. Theoretically, the high hole transport ability of $CH_3NH_3PbI_3$ voids the need for using an HTM, which prompts the development of new nanocomposite solar cells: mesoporous scaffold based solar cells (Figure 3(b)). In these structured solar cells, $CH_3NH_3PbI_3$ is fully infiltrated between the TiO_2, and no additional space is mandatorily needed for HTMs. Such structure could save the thickness of the film to 200–300 nm. Poly(triarylamine) was used as HTM for this new PSC and attained PCE of 12%, suggesting the carrier collection by hole transport through the perovskite was quite effective [20]. By using hybrid composite of single-wall carbon nanotube-PMMA and P3HT as HTM, planar PSC achieved a PCE up to 15.3% and resistance to degradation by water was remarkably improved [49]. Ambipolar structure of $CH_3NH_3PbI_3$ was verified by transistor measurement [4, 19]. Both electron and hole transport ability pave the way for the planar device.

4. Photoanode Morphologies for PSCs

Photoanodes, as the support for sensitizer loading, play a vital role in the performance of PSCs. So far, several kinds of PSCs have been developed, such as nanoparticle based PSCs, one-dimensional nanomaterial-based PSCs, planar devices, and flexible devices.

4.1. Nanoparticle Based PSCs. TiO_2 nanoparticles (NPs) are the most common scaffolds that are used for PSCs. Due to the ambipolar charge transport nature of perovskite, as shown in Figures 3(a) and 3(b), the NPs-based PSCs can be categorized into two structural PSCs. The one similar to traditional solid-state semiconductor sensitized solar cells is
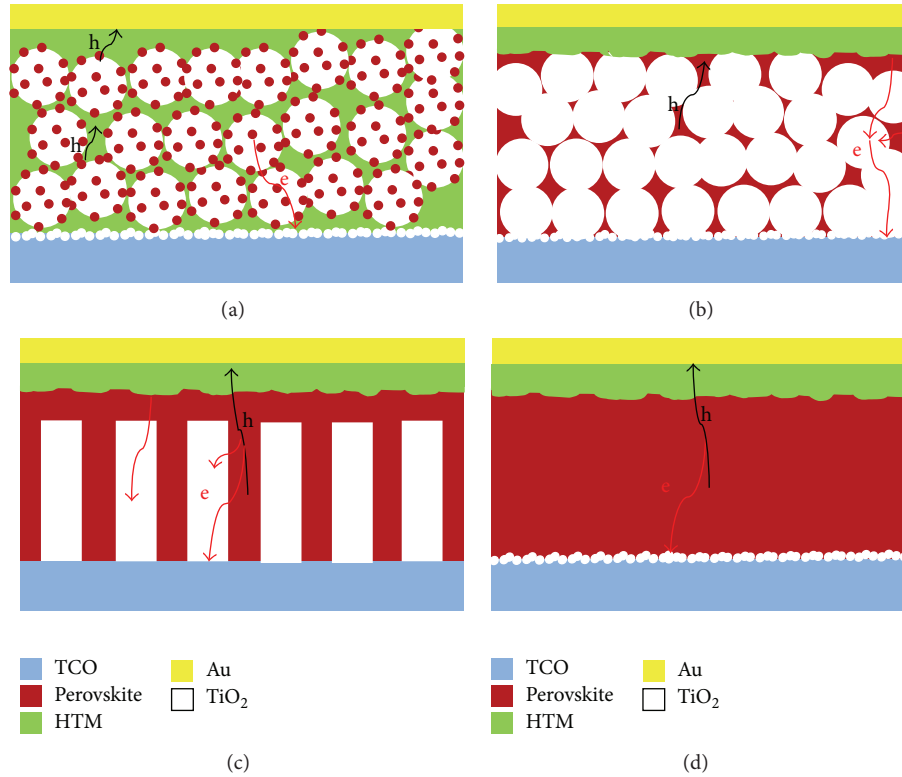
FIGURE 3: Schematic illustrations of perovskite sensitized solar cells PSCs. (a) Perovskite anchored on nanoparticles. (b) Perovskite penetrated through nanoparticles. (c) 1D nanomaterials-based PSCs. (d) Planar PSCs. Charge transport routes are schematically depicted. Red arrows are for electron. Black arrows are for holes.

shown in Figure 3(a). In this structure, the mesoporous TiO_2 film usually acts as an electron extraction layer, transporting photogenerated electrons to the electron collector electrode (as the red arrow shown in Figure 3(a)), while the perovskite mainly acts as a sensitizer. The holes are primarily transported by the penetrated HTM (black arrow shown in Figure 3(a)). A representative PSC of this structure is the mesoporous Al_2O_3 based PSC, which has a PCE of 10.9%, while the mesoporous TiO_2 based PSC has a PCE of 7.6% [4]. The PCE of the mesoporous TiO_2 based PSC was improved to 9% [34] and to 12.8% [38] subsequently. By using commercial carbon as the counter electrode, $CH_3NH_3PbI_3$ sensitized mesoporous TiO_2 solar cell achieved a PCE of 8.31% with a good stability [50]. Theoretically, the liquid electrolyte based PSCs also belong to this kind of PSCs. The first reported liquid electrolyte based $CH_3NH_3PbI_3$ and $CH_3NH_3PbBr_3$ sensitized solar cells employed ~15 nm sized, 8–12 μm TiO_2 NP films which provided a large surface area for perovskite loading [1].

According to the literatures summarized in the *Hole Transport Materials* section, the unique ambipolar charge transport property of perovskites renders the photoanode no longer needed to spare much space for HTMs in the PSC architecture. Therefore, a new kind of PSC, which had the interstitial spaces between the photoanode NPs being completely filled with perovskite (Figure 3(b)), is developed. In this kind of PSCs, photogenerated electrons in the perovskite diffuse through the perovskite to the nearest TiO_2

NPs and then are transported along the TiO_2 skeleton to the electron collector electrode (the red arrow in Figure 3(b)). Holes are transported by the perovskite (the black arrow in Figure 3(b)). The first HTM-free PSC was fabricated using TiO_2 nanosheets as a support, and $CH_3NH_3PbI_3$ was deposited on TiO_2 nanosheets. Such device generated a PCE of 5.5%. In this architecture, $CH_3NH_3PbI_3$ was believed to act as both light harvester and HTM [19]. The Au@SiO_2 nanoparticle (NP) based PSC delivering a device efficiency of up to 11.4% was reported, in which the enhanced photocurrent was attributed to the reduced exciton binding energy due to the incorporation of metal NPs rather than the enhanced light absorption [51]. V_{oc} of ~1.3 V was obtained by a $CH_3NH_3PbBr_3$ PSC on the TiO_2 NP scaffold [52]. In addition, mesoporous TiO_2 film was used to anchor $CH_3NH_3Pb(I_{1-x}Br_x)_3$ to tune its light absorbing property and such device achieved the highest PCE of 12.3% [11]. To date, a certified PCE of 17.9% was realized by the $CH_3NH_3PbI_{3-x}Br_x$ (x = 0.1–0.15) PSC on a TiO_2 NP scaffold [7]. Up to now, this is the highest reported PCE for mesoporous NP-based PSC.

Unlike the dye-sensitized solar cells and other semiconductor-sensitized solar cells, different shaped TiO_2 NPs are not the focus for PSCs. However, as is introduced above, NPs-based PSCs show a great prospect to exhibit high PCE.

4.2. NR Based PSCs. One-dimensional nanomaterials are believed to promote electron transport, elongate electron lifetime, increase diffusion length, and slow down the electron
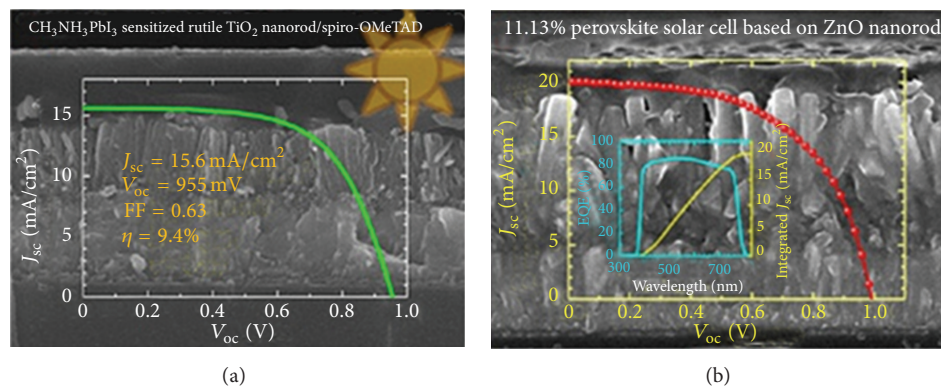
CH$_3$NH$_3$PbI$_3$ sensitized rutile TiO$_2$ nanorod/spiro-OMeTAD

J_{sc} = 15.6 mA/cm^2
V_{oc} = 955 mV
FF = 0.63
η = 9.4%

11.13% perovskite solar cell based on ZnO nanorod

(a)

(b)

FIGURE 4: 1D nanomaterials-based PSCs. (a) CH$_3$NH$_3$PbI$_3$ sensitized TiO$_2$ NRs solar cells. Reprinted from [22]. Copyright: the American Chemical Society. (b) CH$_3$NH$_3$PbI$_3$ sensitized ZnO NRs solar cells. Reprinted from [23]. Copyright: the American Chemical Society.

and hole recombination [53–56]. A PCE of 9.4% was achieved on a 600 nm thick TiO$_2$ nanorod array photoanode. Results showed that longer NRs deteriorated the V_{oc} and the charge generation efficiency (Figure 4(a)) [22]. Qiu et al. reported a PSC with a PCE of 4.87% using CH$_3$NH$_3$PbI$_2$Br as light absorber with TiO$_2$ nanowire arrays. The PCE of this PSC was higher than that of CH$_3$NH$_3$PbI$_3$ solar cell [57]. The device using 1D ZnO incorporated with CH$_3$NH$_3$PbI$_3$ also showed a PCE of 11.13% with the short-circuit current density J_{sc} of 20.08 mA/cm^2, the open-circuit voltage V_{oc} of 991 mV, and fill factor of 0.56 (Figure 4(b)) [23].

Although the literatures on 1D nanomaterial-based PSCs are not as many as those of the NP-based or planar PSCs, the superior ambipolar charge transport of perovskite does not require the large specific surface area from the scaffolds, which would compensate for the drawbacks of 1D nanomaterials. Owing to the superior charge transport of 1D nanomaterials, they might function synergistically with perovskites in PSCs application.

4.3. Planar Devices. The ambipolar charge transport property of CH$_3$NH$_3$PbI$_3$ simplifies the architectures of PSCs. Because of the self-charge transport property towards electrons and holes together with the light absorbing property, the PSCs can work without the scaffold and HTMs. A simple planar heterojunction solar cell was fabricated without the metal oxide scaffold, incorporating vapour-deposited perovskite as the absorbing layer and spiro-OMeTAD as the HTM. Such PSC had a PCE up to 15.4% (Figure 2(a)) [5]. Planar CH$_3$NH$_3$PbI$_3$ perovskite/fullerene planar heterojunction hybrid solar cell was developed with a PCE of 3.9%, and its interfaces were tuned by conducting polymers, where CH$_3$NH$_3$PbI$_3$/fullerene interface was verified as the donor-acceptor interface [58]. By evaporating CH$_3$NH$_3$I at 150°C to react with the PbI$_2$ film, Chen et al. developed a vapor-assisted solution process to fabricate a full coverage and small roughness planar heterojunction CH$_3$NH$_3$PbI$_3$ device, which yielded a PCE of 12.1% [25]. Another newly structured planar PSC, which had CH$_3$NH$_3$PbI$_3$ sandwiched between two thin organic charge-transporting layers, reached a high PCE over 12% [24]. By tuning the interface states and matching the

band diagram, a record PCE of 19.3% on a planar device was obtained by Zhou et al. recently [9].

The PSC PCE race joined by scientists all over the world is still ongoing. It is too early to draw any conclusion to what record PCE of PSCs can be achieved. However, the surging PCEs of planar PSCs and ease of fabrication of planar devices imply that future PSCs may adopt such simple configuration.

4.4. Flexible PSCs. PSCs on flexible substrates are advantageous for a few reasons. Such PSCs are much more portable and practical for mobile electronics, such as cell phones and laptops. They can also save more space and are not easy to break. The low processing temperature of perovskites will promote the realization of flexible PSCs.

As a part of PSCs research, lots of efforts are put into designing flexible PSCs. The PSC with substrate/PEDOT: PSS/CH$_3$NH$_3$PbI$_{3-x}$Cl$_x$/PCBM/TiO$_x$/Al configuration was fabricated on ITO-coated plastic foil with a PCE over 6% [59]. The PCE of flexible PSC was subsequently improved to 9.2% by Yang group [60]. Carbon nanotubes were used as the hole collector and the support for CH$_3$NH$_3$PbI$_3$ loading. Such HTM-free device realized PCE of 6.87%. By using spiro-OMeTAD as the HTM, the PCE was improved to 9.90% [61]. By replacing the TiO$_2$ dense electron transport layer with ZnO on conducting flexible substrate and adopting spiro-OMeTAD as the HTM, CH$_3$NH$_3$PbI$_3$ PSC fabricated at 100°C yielded a PCE of 15.7%, which is close to the record PCE [62]. However, these achievements still seem far away for practical applications.

5. Challenges and Perspective

Even now, rapid progress takes place every day, faster than ever in photovoltaic field. The PCE of 19.3% realized by Yang group [9] is a huge step towards real life applications. Scientists anticipate that PCEs of 28 to 30% are feasible in the near future by fabricating perovskite and crystalline silicon cells in a tandem configuration [47].

Nevertheless, stability is still a big challenge for PSCs. CH$_3$NH$_3$PbI$_3$ is very sensitive to polar solvents such as water. It readily dissolves and decomposes into PbI$_2$ rapidly. Up

to now, only a few studies on stability have been reported [6]. These reports concluded that the HTM with long alkyl chains and without deliquescent additives would reduce the water filtration and prevent sensitizer corrosion and improve the humidity stability [63]. Carbon material used as the back contact is believed to act as a water-retaining layer as well. The PCE of the device did not show a decrease after exposure to air for over 1000 hours [21]. However, there is still a long way to go to meet the rigid requirement for long-term outdoor practical applications. On the other hand, the longtime UV exposure stability is another problem for PSCs. Snaith et al. investigated the effect of longtime exposure towards UV light on the performance of PSCs. The performance of PSCs would decay due to the light-induced desorption of surface-adsorbed oxygen on mesoporous TiO_2. However, TiO_2-free PSCs are protected from this instability [64].

Toxicity of heavy metal lead to people and the environment is another big concern for scaling up production of PSCs. Scientists are attempting to synthesize lead-free perovskites [5, 64]. The PSC incorporating $CH_3NH_3SnI_{3-x}Br_x$, a lead-free perovskite, and spiro-OMeTAD produced a PCE of 5.73% [33]. Another alternative is $CH_3NH_3SnI_3$ on a TiO_2 scaffold, which achieved a PCE of 6.4% [65]. To prevent environmental pollution from lead, perovskites made from lead-free composition are likely to be the next widely researched area for PSCs. In general, before making full use of the PSC technology, all the above issues need to be addressed.

Conflict of Interests

The authors declare no competing financial interests.

Acknowledgments

References

[1] A. Kojima, K. Teshima, Y. Shirai, and T. Miyasaka, "Organometal halide perovskites as visible-light sensitizers for photovoltaic cells," *Journal of the American Chemical Society*, vol. 131, no. 17, pp. 6050–6051, 2009.

[2] J.-H. Im, C.-R. Lee, J.-W. Lee, S.-W. Park, and N.-G. Park, "6.5% efficient perovskite quantum-dot-sensitized solar cell," *Nanoscale*, vol. 3, no. 10, pp. 4088–4093, 2011.

[3] I. Chung, B. Lee, J. He, R. P. H. Chang, and M. G. Kanatzidis, "All-solid-state dye-sensitized solar cells with high efficiency," *Nature*, vol. 485, no. 7399, pp. 486–489, 2012.

[4] M. M. Lee, J. Teuscher, T. Miyasaka, T. N. Murakami, and H. J. Snaith, "Efficient hybrid solar cells based on meso-superstructured organometal halide perovskites," *Science*, vol. 338, no. 6107, pp. 643–647, 2012.

[5] M. Liu, M. B. Johnston, and H. J. Snaith, "Efficient planar heterojunction perovskite solar cells by vapour deposition," *Nature*, vol. 501, no. 7467, pp. 395–398, 2013.

[6] J. Burschka, N. Pellet, S. J. Moon et al., "Sequential deposition as a route to high-performance perovskite-sensitized solar cells," *Nature*, vol. 499, no. 7458, pp. 316–319, 2013.

[7] N. J. Jeon, J. H. Noh, Y. Kim, W. S. Yang, S. Ryn, and S. I. Seok, "Solvent engineering for high-performance inorganic-organic hybrid perovskite solar cells," *Nature Materials*, vol. 13, pp. 897–903, 2014.

[8] R. F. Service, "Perovskite solar cells keep on surging," *Science*, vol. 344, no. 6183, p. 458, 2014.

[9] H. Zhou, Q. Chen, G. Li et al., "Interface engineering of highly efficient perovskite solar cells," *Science*, vol. 345, no. 6196, pp. 542–546, 2014.

[10] http://www.nrel.gov/ncpv/images/efficiency_chart.jpg.

[11] J. H. Noh, S. H. Im, J. H. Heo, T. N. Mandal, and S. I. Seok, "Chemical management for colorful, efficient, and stable inorganic-organic hybrid nanostructured solar cells," *Nano Letters*, vol. 13, no. 4, pp. 1764–1769, 2013.

[12] G. E. Eperon, S. D. Stranks, C. Menelaou, M. B. Johnston, L. M. Herz, and H. J. Snaith, "Formamidinium lead trihalide: a broadly tunable perovskite for efficient planar heterojunction solar cells," *Energy and Environmental Science*, vol. 7, no. 3, pp. 982–988, 2014.

[13] L. K. Ono, S. Wang, Y. Kato, S. R. Raga, and Y. Qi, "Fabrication of semi-transparent perovskite films with centimeter-scale superior uniformity by the hybrid deposition method," *Energy & Environmental Science*, vol. 7, pp. 3989–3993, 2014.

[14] T. Baikie, Y. Fang, J. M. Kadro et al., "Synthesis and crystal chemistry of the hybrid perovskite (CH_3NH_3)PbI_3 for solid-state sensitised solar cell applications," *Journal of Materials Chemistry A*, vol. 1, no. 18, pp. 5628–5641, 2013.

[15] C. S. Ponseca Jr., T. J. Savenije, M. Abdellah et al., "Organometal halide perovskite solar cell materials rationalized: ultrafast charge generation, high and microsecond-long balanced mobilities, and slow recombination," *Journal of the American Chemical Society*, vol. 136, no. 14, pp. 5189–5192, 2014.

[16] D. B. Mitzi, "Templating and structural engineering in organic–inorganic perovskites," *Journal of the Chemical Society, Dalton Transactions*, pp. 1–12, 2001.

[17] G. Xing, N. Mathews, S. Sun et al., "Long-range balanced electron-and hole-transport lengths in organic-inorganic $CH_3NH_3PbI_3$," *Science*, vol. 342, no. 6156, pp. 344–347, 2013.

[18] S. D. Stranks, G. E. Eperon, G. Grancini et al., "Electron-hole diffusion lengths exceeding 1 micrometer in an organometal trihalide perovskite absorber," *Science*, vol. 342, no. 6156, pp. 341–344, 2013.

[19] L. Etgar, P. Gao, Z. Xue et al., "Mesoscopic $CH_3NH_3PbI_3$/TiO_2 heterojunction solar cells," *Journal of the American Chemical Society*, vol. 134, no. 42, pp. 17396–17399, 2012.

[20] J. H. Heo, S. H. Im, J. H. Noh et al., "Efficient inorganic-organic hybrid heterojunction solar cells containing perovskite compound and polymeric hole conductors," *Nature Photonics*, vol. 7, no. 6, pp. 486–491, 2013.

[21] A. Mei, X. Li, L. Liu et al., "A hole-conductor-free, fully printable mesoscopic perovskite solar cell with high stability," *Science*, vol. 345, no. 6194, pp. 295–298, 2014.

[22] H. S. Kim, J. W. Lee, N. Yantara et al., "High efficiency solid-state sensitized solar cell-based on submicrometer rutile TiO_2 nanorod and $CH_3NH_3PbI_3$ perovskite sensitizer," *Nano Letters*, vol. 13, no. 6, pp. 2412–2417, 2013.

[23] D.-Y. Son, J.-H. Im, H.-S. Kim, and N.-G. Park, "11% efficient perovskite solar cell based on ZnO nanorods: an effective charge collection system," *The Journal of Physical Chemistry C*, vol. 118, no. 30, pp. 16567–16573, 2014.

[24] S. Pan, Z. Yang, H. Li, L. Qiu, H. Sun, and H. Peng, "Efficient dye-sensitized photovoltaic wires based on an organic redox electrolyte," *The Journal of the American Chemical Society*, vol. 135, no. 29, pp. 10622–10625, 2013.

[25] Q. Chen, H. Zhou, Z. Hong et al., "Planar heterojunction perovskite solar cells via vapor-assisted solution process," *Journal of the American Chemical Society*, vol. 136, no. 2, pp. 622–625, 2014.

[26] M. R. Leyden, L. K. Ono, S. R. Raga, Y. Kato, S. Wang, and Y. Qi, "High performance perovskite solar cells by hybrid chemical vapor deposition," *Journal of Materials Chemistry A*, vol. 2, no. 44, pp. 18742–18745, 2014.

[27] M. J. Carnie, C. Charbonneau, M. L. Davies et al., "A one-step low temperature processing route for organolead halide perovskite solar cells," *Chemical Communications*, vol. 49, no. 72, pp. 7893–7895, 2013.

[28] G. E. Eperon, V. M. Burlakov, P. Docampo, A. Goriely, and H. J. Snaith, "Morphological control for high performance, solution-processed planar heterojunction perovskite solar cells," *Advanced Functional Materials*, vol. 24, no. 1, pp. 151–157, 2014.

[29] Z. Cheng and J. Lin, "Layered organic-inorganic hybrid perovskites: structure, optical properties, film preparation, patterning and templating engineering," *CrystEngComm*, vol. 12, no. 10, pp. 2646–2662, 2010.

[30] C. C. Stoumpos, C. D. Malliakas, and M. G. Kanatzidis, "Semiconducting tin and lead iodide perovskites with organic cations: phase transitions, high mobilities, and near-infrared photoluminescent properties," *Inorganic Chemistry*, vol. 52, no. 15, pp. 9019–9038, 2013.

[31] B. Wang, X. Xiao, and T. Chen, "Perovskite photovoltaics: a high-efficiency newcomer to the solar cell family," *Nanoscale*, vol. 6, no. 21, pp. 12287–12297, 2014.

[32] Y. Ogomi, A. Morita, S. Tsukamoto et al., "$CH_3NH_3SnxPb_{(1-x)}I_3$ perovskite solar cells covering up to 1060 nm," *Journal of Physical Chemistry Letters*, vol. 5, no. 6, pp. 1004–1011, 2014.

[33] F. Hao, C. C. Stoumpos, D. H. Cao, R. P. H. Chang, and M. G. Kanatzidis, "Lead-free solid-state organic-inorganic halide perovskite solar cells," *Nature Photonics*, vol. 8, no. 6, pp. 489–494, 2014.

[34] H.-S. Kim, C.-R. Lee, J.-H. Im et al., "Lead iodide perovskite sensitized all-solid-state submicron thin film mesoscopic solar cell with efficiency exceeding 9%," *Scientific Reports*, vol. 2, article 591, 2012.

[35] A. Abrusci, S. D. Stranks, P. Docampo, H. L. Yip, A. K. Y. Jen, and H. J. Snaith, "High-performance perovskite-polymer hybrid solar cells via electronic coupling with fullerene monolayers," *Nano Letters*, vol. 13, no. 7, pp. 3124–3128, 2013.

[36] D. Bi, L. Yang, G. Boschloo, A. Hagfeldt, and E. M. J. Johansson, "Effect of different hole transport materials on recombination in $CH_3NH_3PbI_3$ perovskite-sensitized mesoscopic solar cells," *Journal of Physical Chemistry Letters*, vol. 4, no. 9, pp. 1532–1536, 2013.

[37] J. H. Noh, N. J. Jeon, Y. C. Choi, M. K. Nazeeruddin, M. Grätzel, and S. I. Seok, "Nanostructured $TiO_2/CH_3NH_3PbI_3$ heterojunction solar cells employing spiro-OMeTAD/Co-complex as hole-transporting material," *Journal of Materials Chemistry A*, vol. 1, no. 38, pp. 11842–11847, 2013.

[38] P. Qin, S. Paek, M. I. Dar et al., "Perovskite solar cells with 12.8% efficiency by using conjugated quinolizino acridine based hole transporting material," *Journal of the American Chemical Society*, vol. 136, no. 24, pp. 8516–8519, 2014.

[39] N. J. Jeon, H. G. Lee, Y. C. Kim et al., "*o*-Methoxy substituents in spiro-OMeTAD for efficient inorganic-organic hybrid perovskite solar cells," *Journal of the American Chemical Society*, vol. 136, no. 22, pp. 7837–7840, 2014.

[40] H. J. Snaith, A. Abate, J. M. Ball et al., "Anomalous hysteresis in perovskite solar cells," *Journal of Physical Chemistry Letters*, vol. 5, no. 9, pp. 1511–1515, 2014.

[41] J. A. Christians, R. C. M. Fung, and P. V. Kamat, "An inorganic hole conductor for Organo-lead halide perovskite solar cells. improved hole conductivity with copper iodide," *Journal of the American Chemical Society*, vol. 136, no. 2, pp. 758–764, 2014.

[42] P. Qin, S. Tanaka, S. Ito et al., "Inorganic hole conductor-based lead halide perovskite solar cells with 12.4% conversion efficiency," *Nature Communications*, vol. 5, article 3834, 2014.

[43] A. S. Subbiah, A. Halder, S. Ghosh, N. Mahuli, G. Hodes, and S. K. Sarkar, "Inorganic hole conducting layers for perovskite-based solar cells," *Journal of Physical Chemistry Letters*, vol. 5, no. 10, pp. 1748–1753, 2014.

[44] K. C. Wang, P. S. Shen, M. H. Li et al., "Low-temperature sputtered nickel oxide compact thin film as effective electron blocking layer for mesoscopic $NiO/CH_3NH_3PbI_3$ perovskite heterojunction solar cells," *ACS Applied Materials & Interfaces*, vol. 6, no. 15, pp. 11851–11858, 2014.

[45] L. Hu, J. Peng, W. Wang et al., "Sequential deposition of $CH_3NH_3PbI_3$ on planar NiO film for efficient planar perovskite solar cells," *ACS Photonics*, vol. 1, no. 7, pp. 547–553, 2014.

[46] J. H. Kim, P.-W. Liang, S. T. Williams et al., "High-performance and environmentally stable planar heterojunction perovskite solar cells based on a solution-processed copper-doped nickel oxide hole-transporting layer," *Advanced Materials*, 2014.

[47] M. Grätzel, "The light and shade of perovskite solar cells," *Nature Materials*, vol. 13, no. 9, pp. 838–842, 2014.

[48] J. M. Ball, M. M. Lee, A. Hey, and H. J. Snaith, "Low-temperature processed meso-superstructured to thin-film perovskite solar cells," *Energy and Environmental Science*, vol. 6, no. 6, pp. 1739–1743, 2013.

[49] S. N. Habisreutinger, T. Leijtens, G. E. Eperon, S. D. Stranks, R. J. Nicholas, and H. J. Snaith, "Carbon nanotube/polymer composites as a highly stable hole collection layer in perovskite solar cells," *Nano Letters*, vol. 14, no. 10, pp. 5561–5568, 2014.

[50] F. Zhang, X. Yang, H. Wang, M. Cheng, J. Zhao, and L. Sun, "Structure engineering of hole-conductor free perovskite-based solar cells with low-temperature-processed commercial carbon paste as cathode," *ACS Applied Materials & Interfaces*, vol. 6, no. 18, pp. 16140–16146, 2014.

[51] W. Zhang, M. Saliba, S. D. Stranks et al., "Enhancement of perovskite-based solar cells employing core-shell metal nanoparticles," *Nano Letters*, vol. 13, no. 9, pp. 4505–4510, 2013.

[52] E. Edri, S. Kirmayer, D. Cahen, and G. Hodes, "High open-circuit voltage solar cells based on organic-inorganic lead bromide perovskite," *Journal of Physical Chemistry Letters*, vol. 4, no. 6, pp. 897–902, 2013.

[53] G. Peng, X. Xu, F. Mei et al., "Substrate placement angle-dependent growth of dandelion-like TiO_2 nanorods for solid-state semiconductor-sensitized solar cells," *RSC Advances*, vol. 4, no. 95, pp. 53335–53343, 2014.

[54] B. Liu and E. S. Aydil, "Growth of oriented single-crystalline rutile TiO_2 nanorods on transparent conducting substrates for dye-sensitized solar cells," *Journal of the American Chemical Society*, vol. 131, no. 11, pp. 3985–3990, 2009.

[55] W.-T. Sun, Y. Yu, H.-Y. Pan, X.-F. Gao, Q. Chen, and L.-M. Peng, "CdS quantum dots sensitized TiO_2 nanotube-array photoelectrodes," *Journal of the American Chemical Society*, vol. 130, no. 4, pp. 1124–1125, 2008.

[56] G. Peng, J. Wu, Y. Zhao, X. Xu, G. Xu, and A. Star, "Ultra-small TiO_2 nanowire forests on transparent conducting oxide for solid-state semiconductor-sensitized solar cells," *RSC Advances*, vol. 4, pp. 46987–46991, 2014.

[57] J. Qiu, Y. Qiu, K. Yan et al., "All-solid-state hybrid solar cells based on a new organometal halide perovskite sensitizer and one-dimensional TiO_2 nanowire arrays," *Nanoscale*, vol. 5, no. 8, pp. 3245–3248, 2013.

[58] J.-Y. Jeng, Y.-F. Chiang, M.-H. Lee et al., "$CH_3NH_3PbI_3$ perovskite/fullerene planar-heterojunction hybrid solar cells," *Advanced Materials*, vol. 25, no. 27, pp. 3727–3732, 2013.

[59] P. Docampo, J. M. Ball, M. Darwich, G. E. Eperon, and H. J. Snaith, "Efficient organometal trihalide perovskite planar-heterojunction solar cells on flexible polymer substrates," *Nature Communications*, vol. 4, article 2761, 2013.

[60] Y. Yang, J. You, Z. Hong et al., "Low-temperature solution-processed perovskite solar cells with high efficiency and flexibility," *ACS Nano*, vol. 8, no. 2, pp. 1674–1680, 2014.

[61] Z. Li, S. A. Kulkarni, P. P. Boix et al., "Laminated carbon nanotube networks for metal electrode-free efficient perovskite solar cells," *ACS Nano*, vol. 8, no. 7, pp. 6797–6804, 2014.

[62] D. Liu and T. L. Kelly, "Perovskite solar cells with a planar heterojunction structure prepared using room-temperature solution processing techniques," *Nature Photonics*, vol. 8, no. 2, pp. 133–138, 2014.

[63] J. Liu, Y. Wu, C. Qin et al., "A dopant-free hole-transporting material for efficient and stable perovskite solar cells," *Energy & Environmental Science*, vol. 7, no. 9, pp. 2963–2967, 2014.

[64] T. Leijtens, G. E. Eperon, S. Pathak, A. Abate, M. M. Lee, and H. J. Snaith, "Overcoming ultraviolet light instability of sensitized TiO_2 with meso-superstructured organometal trihalide perovskite solar cells," *Nature Communications*, vol. 4, article 2885, 2013.

[65] N. K. Noel, S. D. Stranks, A. Abate et al., "Lead-free organic-inorganic tin halide perovskites for photovoltaic applications," *Energy & Environmental Science*, vol. 7, no. 9, pp. 3061–3068, 2014.

Research Article

Hydrolysis of Straw in Ionic Liquids with Acid as Catalyst under Microwave Irradiation

Yuanjing Zhang, Gang Wei, Guangyi Yu, and Ning Qiao

State Key Laboratory of Chemical Resource Engineering, Beijing University of Chemical Technology, Beijing 100029, China

Correspondence should be addressed to Ning Qiao; qiaoning_buct@163.com

With ionic liquids as solvents and corn straw as raw material, different processes of lignocellulose pretreatment with acid as catalyst were studied under conventional heating/microwave irradiation and the reducing sugar was measured. The results indicated that acid can accelerate hydrolysis reaction of corn straw into reducing sugar with ionic liquids as solvent, and microwave irradiation was more efficient in pretreatment of corn straw than conventional heating. The influences of different acid catalysts, the concentration of acid, temperature, mass ratio of straw/[Bmim]Cl, and the amount of refill water were mainly tested, and the optimum experimental conditions are thus determined.

1. Introduction

Biomass resource is a kind of renewable resources to meet the requirements of sustainable development, which has attracted considerable attention [1]. Lignocellulose, as the most abundant and cheapest biomass resources on the earth, can be turned into commodity chemicals and a variety of biological fuels [2] such as biodiesel, ethanol, and butanol, by biological or chemical means, which is considered an effective way to replace fossil energy and alleviate the problem of energy crisis. It is difficult for reagent to reach cellulose because of high crystallinity of lignocellulose in natural biomass. Therefore, pretreatment of lignocellulosic biomass prior to use as feedstock for biofuel and chemical production is required to either disrupt the crystalline structure of cellulose, remove hemicellulose, or remove or modify the lignin, to increase the exposure of the cellulosic substrate to hydrolytic enzymes, decrease cellulosic substrate recalcitrance for enzyme attack, and thus increase glucose yield [3–5].

Since Rogers found that the ionic liquids (ILs) can dissolve cellulose in 2002 [6], in the use of ILs dissolving cellulose, a lot of fruitful works have been carried out both at home and abroad [7–9]. Recently, new attention has been focused on the pretreatment of lignocellulosic biomass in ILs [7, 10] because of the ability of some ILs to dissolve cellulose under moderate conditions and the possibility of recovering nearly 100% of the IL in its initial purity [11]. ILs are liquids at room temperature or near room temperature composed of ions [10]. As a new type of green solvent, ILs are nonflammable and possess many good qualities such as a very low vapor pressure, good thermal stability, and recycled performance. Depending upon the ILs used, lignocellulosic biomass may be completely dissolved by the ILs and subsequently regenerated by adding antisolvents such as water [7]. It has been demonstrated that cellulose reprecipitated after dissolution in ILs exhibits much higher enzymatic hydrolysis owing to its decreased crystallinity [12]. However, the high cost, high viscosity, and troublesome separation of ILs still hamper their commercialized application. To overcome these problems, several trials [13–16] were performed to develop the hydrolysis of cellulose catalyzed by some solid acids, but this heterogeneously catalytic process shows relatively low hydrolysis efficiency due to mass transfer resistance between solid acids and insoluble cellulose in water.

Microwave heating is based on an internal heating process based on the direct absorption of energy by polar molecules, which differs from conventional heating that is based on heat transfer. Some studies have showed that microwave irradiation enhances the dissolution of lignocellulosic materials in

IL and subsequent fractionation of cellulose and lignin [17–20]. Moreover, with regard to its application to IL-assisted biomass pretreatment for subsequent enzymatic hydrolysis, it has been recently demonstrated that microwave irradiation can facilitate the pretreatment of cellulose in IL [21, 22].

In the present study, with corn straw as raw material, a more effective lignocellulosic biomass pretreatment process was developed using a commonly researched IL, 1-butyl-3-methylimidazolium chloride (BMIMCl), as a model IL and an acid catalyst under microwave irradiation. The influence of different pretreatment scheme on straw hydrolysis was studied, and the role of heating mode played on lignocellulose conversion was examined with ILs as solvents; at the same time, the straw pretreatment process was optimized.

2. Materials and Methods

2.1. Material. Straw was used as a model lignocellulosic material (collected from Hebei province in China). The straw was washed with a lot of water, air-dried to constant weight, and milled and screened into powder with particle sizes between 2.50 and 5 mm and then was collected and stored at room temperature in a sealed container. N-Methylimidazole, chlorinated n-butane, sodium hydroxide, phenol, sodium sulfate, and potassium sodium tartrate were provided by Beijing chemical reagent factory. Nitrosalicylic acid and sulfuric acid were purchased from Beijing Chemical Works. All the chemicals used in this study were of analytical grade. Microwave heating device was self-designed, which included a microwave oven (MM721NG1-PW, purchased from Midea Corporation), a circular waveguide, and a stirrer device.

2.2. Preparation of 1-Butyl-3-methylimidazole Chloride ([Bmim]Cl) IL. The N-methylimidazole and chlorinated n-butane reacted for about 48 h in mole ratio of 1:1 at 70°C under nitrogen atmosphere. At the end of the reaction a layered mixture was obtained and then the mixture was filtered with a funnel and the lower liquid was product. After that the product was washed with ethyl acetate and purified under rotary evaporation, and the final product was obtained after vacuum drying and stored for use.

2.3. Acid Catalyzed Hydrolysis in IL. Hydrolysis reaction of straw in IL phase was carried out under the environment of airtight and constant pressure. The IL ([Bmim]Cl) and dry straw were added to a reactor in a certain ratio, then certain amount of water and acid catalyst were added, and the reactor was sealed and heated to certain temperature ((1) in water phase as conventional heating means; (2) under certain gear of microwave oven in an intermittent way and different gear corresponding to different power) and kept for 2 hours. (Adding acid to the preheated sample was determined as starting time for reaction.) Electromagnetic stirring speed was controlled at 300 r/min during reaction, and the speed may be increased (<600 r/min) if straw dissolution effect is not good or no monosaccharide is detected. A certain amount of hydrolysate was diluted with water after reaction, and contents of reducing sugar of the diluted solution were detected by using the DNS method.

2.4. DNS Analysis and Calculation of Total Reducing Sugar. The yield of TRS (total reducing sugar) was determined with 3,5-dinitrosalicylic acid colorimetric method (DNS method). (When glucose was used as standard, coefficient 0.9 was introduced in the TRS calculation formula to correct the concentration of reducing sugar because the type of sugar in actual product is more than that). Finally the proportion of the quality of reducing sugar to total straw was used as measurement:

$$\text{TRS} = \frac{m_1 \times n}{m_2} \times 0.9 \times 100\%, \tag{1}$$

where TRS is the yield of total reducing sugar, m_1 is the quality of reducing sugar, n is dilution ratio, and m_2 is the quality of sample straw.

2.5. SEM Analysis of Straw. SEM was used to record the surface morphological features of straw before and after pretreatment. The samples were coated with gold using a Leica EMS CD 005 system prior to analysis by S-4700 scanning electron microscope (magnification: 20~500,000 times; accelerating voltage: 0.5 kV~30 kV, Hitachi LTD., JP).

3. Results and Discussion

3.1. Comparison of Straw Acid Hydrolysis Experiment Scheme. Table 1 shows 7 groups of different experimental scheme by changing different system under different heating modes. In the above different experimental scheme the average reducing sugar yield and the time reached maximum reducing sugar yield were got under the same experimental condition groups.

The data of groups 1 and 4 and groups 2 and 3 show that reducing sugar yield of straw pretreated in IL is higher than that in water system, and data of groups 1 and 3 and groups 2 and 4 show that microwave heating way not only can greatly shorten the reaction time required but also can effectively improve the reducing sugar yield compared with the traditional heating mode, and the maximum TRS is 35.5 wt%. And data in group 5 shows that TRS can be 40.7 wt% if straw was first treated in IL and then hydrolyzed in water. According to data of group 6, a mixture of IL and water system has no advantage, and the reducing sugar yield is only 25.1 wt%.

In the system of [Bmim]Cl IL as solvent, Cl−, and hydrogen atoms of hydroxyl in cellulose macromolecular chain to form hydrogen bonding, hydrogen bonding network of cellulose is thus interrupted, and the cellulose chain is fully exposed in the attack of H+, so the reaction rate is faster and reducing sugar yield is high [23].

By microwave radiation heating hydrolysis of the reducing sugar yield increased significantly; this may be on the one hand because the microwave radiation heating does not depend on the temperature gradient, as a result the system is heated evenly, and on the other hand macromolecular ILs can absorb microwaves better, which heats up quickly, and the reducing sugar yield was increased [24]. Therefore, in the [Bmim]Cl, IL medium with microwave radiation heating can promote acid hydrolysis of the straw.

TABLE 1: Hydrolysis of straw in different ways.

	Solvent	Heat	Time [min]	$\text{Yield}_{\text{TRS}}$ [wt%]
1	IL	Microwave	7	35.5
2	Water	Traditional	240	19.8
3	IL	Traditional	120	30.5
4	Water	Microwave	45	24.4
5[a]	IL (first) + water (last)	Microwave	7 + 45	40.7
6[b]	Water (50 wt%) + IL (50 wt%)	Microwave	45	25.1

[a]Dealing in IL for 7 min and then in water phase system for 45 min.
[b]Dealing directly in the mixed system of IL and water with proportion 1 : 1 to each other.

TABLE 2: Hydrolysis of straw by different acid catalyst.

	Catalyst	Time [min]	$\text{Yield}_{\text{TRS}}$ [wt%]
1	HCl	30	34.4
2	HNO_3	30	26.7
3	H_2SO_4	30	35.5
4	H_3PO_4	30	13.6

At the end of the reaction a part of cellulose does not hydrolyze, but crystallinity is significantly lowered, and structure becomes loose, so hydrolysis in water can further improve the reducing sugar yield.

3.2. Effect of Different Factors on the Straw Hydrolysis. On the basis of the experiment scheme established in Section 3.1, namely, in IL system, with the method of microwave heating, different kind of acid catalyst, acid concentration, temperature, straw to IL mass ratio, and the influence of water supplement were investigated.

3.2.1. Influence of Different Kinds of Acid on the Straw Acid Hydrolysis System. Four different kinds of acids (H_2SO_4, HCl, HNO_3, and H_3PO_4) were used as catalysts in BMIMCl solutions for pretreatment of straw. The pretreatment was carried out under microwave heating, acid concentration 0.5 wt%, straw to IL mass ratio of 0.08, and the straw to filling water mass ratio of 0.25. Table 2 showed the average reducing sugar yield and the time needed for reaching maximum reducing sugar yield using different acid as a catalyst under the condition of six sets of experiments.

As shown in Table 2, in the same reaction time, the highest reducing sugar yield can be obtained when H_2SO_4 is used as catalyst. Similar effect can be found when HCl was used as catalysts. However, HCl is easy to be volatile because of the high temperature in the reaction system, and more water was added to the system since HCl is stored in the form of hydrochloric acid, the water content of which is more than 62.5 wt%. Moreover, the amount of hydrogen ions for 0.5% H_2SO_4 is higher than that of 0.5% HCl. HNO_3 and H_3PO_4 took the third and the fourth place. Because HNO_3 shows strong oxidation activity, side reactions may occur with some reducing sugar. And H_3PO_4 has poor H^+ donor ability due
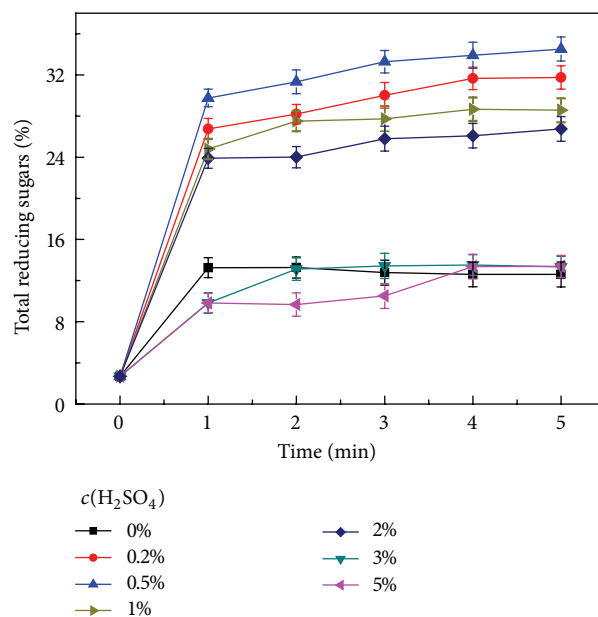

FIGURE 1: Influence of acidity on reducing sugar concentration.

to its subacidity. For the above reasons, we choose H_2SO_4 as catalyst in pretreatment of straw in ILs.

3.2.2. Influence of H_2SO_4 Concentration on the Straw Acid Hydrolysis System. Under the condition of ILs as solvent, microwave heating, reaction temperature 150°C, straw to IL mass ratio of 0.08, and the straw to filling water mass ratio of 0.25, influence of H_2SO_4 concentration was investigated (Figure 1). The yield of reducing sugar increased first and then decreased with the increase of acid concentration. Figure 1 showed that low H_2SO_4 concentration has an obvious advantage. The yield of reducing sugar was low without addition of H_2SO_4; with the increase of H_2SO_4 concentration, it got the maximum when H_2SO_4 concentration was 0.5 wt%. However, when H_2SO_4 concentration increased to 1%, TRS began to decrease. The yield was half the maximum when H_2SO_4 concentration reached 3 wt%, and when H_2SO_4 concentration is 5 wt%, the yield became lower. This indicated that H_2SO_4 concentration has optimum value, which may be 0.5% wt%. H^+ donated by acid played a role of catalyst during

(a)

(b)

(c)

(d)
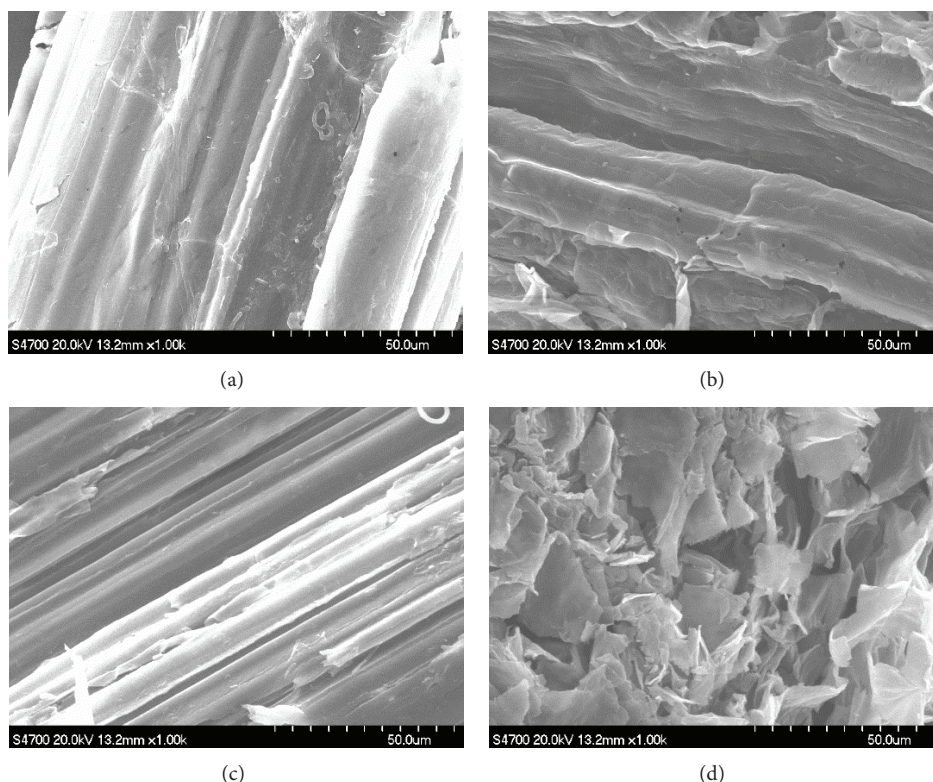
FIGURE 2: SEM of (a) untreated straw; (b) straw pretreated with water containing 0.5% H_2SO_4; (c) straw pretreated with IL; (d) straw pretreated with BMIMCl solution containing 0.5% H_2SO_4.

the reaction. Low concentration acid in the IL system has a high activity and could accelerate the cellulose hydrolysis.

Figure 2 showed the morphology of straw pretreated in different conditions. The structure of untreated straw surface is compact and orderly arranged, and the texture is hard, which resulted in the weak contact of solution with cellulose. Therefore hydrolysis reaction is weak. The surface of straw becomes cracking and the cross section is layered after being pretreated by 0.5 wt% H_2SO_4, and this structure helps solution contact with cellulose which is good for hydrolysis reaction. When pretreated with IL, the cracking in the surface of straw is more serious than that pretreated with 0.5 wt% H_2SO_4 and peels off, thus makes cellulose more exposed which is helpful for IL contact with cellulose and hemicellulose, and promotes the hydrolysis process. When pretreated with IL added with acid catalyst, the surface of straw is seriously damaged and is rupture in flocculent state, which further removes the lignin and hemicellulose shielding of cellulose and release cellulose to a great extent, and thus is advantageous to the hydrolysis reaction. From Figure 2 we can see that IL with acid as catalyst is a good solvent for the hydrolysis of straw.

3.2.3. Influence of Microwave Heating on the Straw Acid Hydrolysis System. Under the condition of ILs as solvent, microwave heating, H_2SO_4 concentration 0.5 wt%, straw to IL mass ratio of 0.08, and the straw to filling water mass ratio of 0.25, influence of reaction temperature was investigated
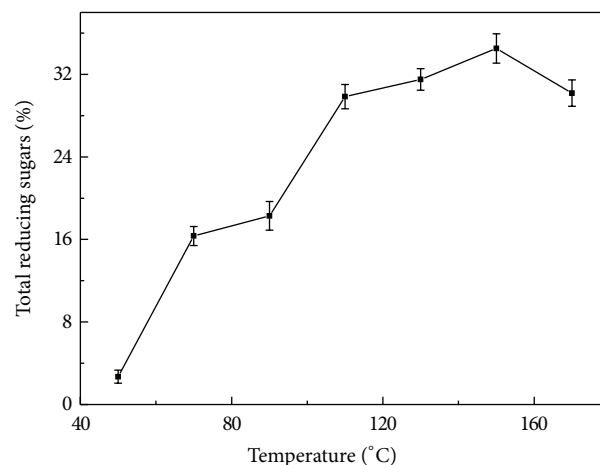

FIGURE 3: Influence of temperature on reducing sugar concentration.

(Figure 3). The yield of reducing sugar gets the maximum (35.5 wt%) at the reaction temperature 150°C. The yield is low under the temperature of 70°C because low temperature could not break the crystal structure of cellulose. When the temperature is higher than 100°C, the yield increases with the increasing of the temperature. This shows that the cellulose hydrolysis occurs obviously. However, when the temperature is higher than 170°C, the ILs are easy to decompose and
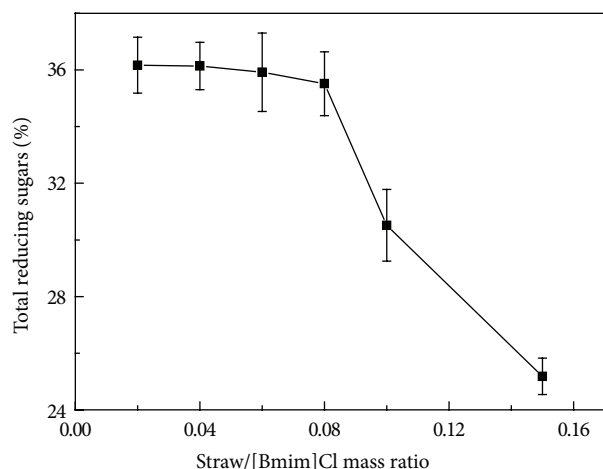
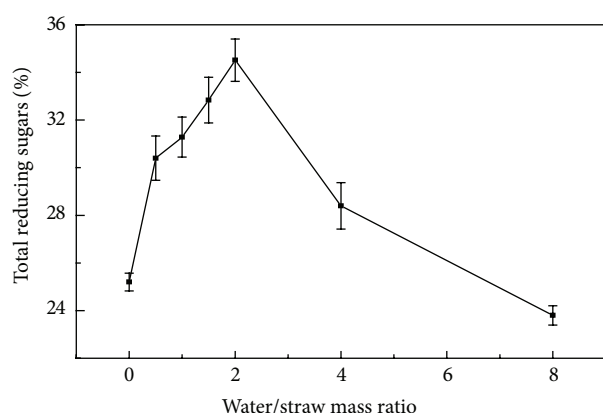FIGURE 4: Reducing sugar concentration in different straw/ [Bmim]Cl.

FIGURE 5: Influence of water/straw mass ratio on reducing sugar concentration.

the straw is easy to carbonize. Therefore the best hydrolysis reaction temperature is 150°C.

3.2.4. Influence of Straw to IL Mass Ratio on the Straw Acid Hydrolysis System. Under the condition of ILs as solvent, microwave heating, H_2SO_4 concentration 0.5 wt%, reaction temperature 150°C, and the straw to filling water mass ratio of 0.25, influence of straw to IL mass ratio was investigated (Figure 4). The yield of reducing sugar gets the maximum at straw to IL mass ratio of 0.08. No obvious change was obtained below this level. And the yield reduces quickly when the ratio is higher than 0.08.

3.2.5. Influence of the Straw to Filling Water Mass Ratio on the Straw Acid Hydrolysis System. Under the condition of ILs as solvent, microwave heating, H_2SO_4 concentration 0.5 wt%, reaction temperature 150°C, and the straw to IL mass ratio of 0.08, influence of straw to filling water mass ratio was investigated (Figure 5). The yield of reducing sugar gets the maximum at straw to filling water mass ratio of 0.25. The reaction system still can get a high yield when the filling

water is little. Even though no filling water is added, a yield of 25 wt% was got since the dehydration of oligosaccharides (e.g., monosaccharide and disaccharide) to 5-hydroxymethylfurfural (5-HMF) can provide water. An appropriate amount can accelerate the reaction and restrain the side reactions. The yield reduces sharply with the increase of filling water. Too much water would break the IL system and rebuild the hydrogen bond between the sugars.

4. Conclusion

We can get the conclusion as follows.

(1) In this experiment ILs with acid as catalyst, as a kind of solvent, can effectively accelerate the hydrolytic reaction of straw.

(2) The yield of reducing sugar is 35.5 wt% under the condition of ILs as solvent and microwave heating, while the yield is just 19.8 wt% under the condition of water as solvent and conventional heat treatment.

(3) The best operating conditions are as follows: atmospheric conditions in closed environment, IL [BMIM]Cl as solvent, H_2SO_4 (concentration 0.5 wt%) as catalyst, the straw to IL mass ratio of 0.08, the straw to filling water mass ratio of 0.25, and reaction temperature 150°C.

Conflict of Interests

The authors declare no conflict of interests.

Acknowledgment

References

[1] A. J. Ragauskas, C. K. William, B. H. Davision et al., "The path forward for biofuels and biomaterials," *Science*, vol. 311, pp. 484–489, 2006.

[2] J. Xiao, L. Shen, Y. Zhang, and J. Gu, "Integrated analysis of energy, economic, and environmental performance of biomethanol from rice straw in China," *Industrial and Engineering Chemistry Research*, vol. 48, no. 22, pp. 9999–10007, 2009.

[3] N. Mosier, C. Wyman, B. Dale et al., "Features of promising technologies for pretreatment of lignocellulosic biomass," *Bioresource Technology*, vol. 96, no. 6, pp. 673–686, 2005.

[4] Y. Z. Zheng, H. M. Lin, and G. T. Tsao, "Pretreatment for cellulose hydrolysis by carbon dioxide explosion," *Biotechnology Progress*, vol. 14, no. 6, pp. 890–896, 1998.

[5] P. Hu, N. Han, X. Zhang et al., "Fabrication of ZnO nanorod-assembled multishelled hollow spheres and enhanced performance in gas sensor," *Journal of Materials Chemistry*, vol. 21, no. 37, pp. 14277–14284, 2011.

[6] R. P. Swatloski, S. K. Spear, J. D. Holbrey, and R. D. Rogers, "Dissolution of cellose with ionic liquids," *Journal of the American Chemical Society*, vol. 124, no. 18, pp. 4974–4975, 2002.

[7] S. Zhu, Y. Wu, Q. Chen et al., "Dissolution of cellulose with ionic liquids and its application: a mini-review," *Green Chemistry*, vol. 8, no. 4, pp. 325–327, 2006.

[8] P. Hu, S. S. Pramana, S. Cao et al., "Ion-induced synthesis of uniform single-crystalline sulphide-based quaternary-alloy hexagonal nanorings for highly efficient photocatalytic hydrogen evolution," *Advanced Materials*, vol. 25, no. 18, pp. 2567–2572, 2013.

[9] N. Winterton, "Solubilization of polymers by ionic liquids," *Journal of Materials Chemistry*, vol. 16, no. 44, pp. 4281–4293, 2006.

[10] P. Alvira, E. Tomás-Pejó, M. Ballesteros, and M. J. Negro, "Pretreatment technologies for an efficient bioethanol production process based on enzymatic hydrolysis: a review," *Bioresource Technology*, vol. 101, no. 13, pp. 4851–4861, 2010.

[11] T. Heinze, K. Schwikal, and S. Barthel, "Ionic liquids as reaction medium in cellulose functionalization," *Macromolecular Bioscience*, vol. 5, no. 6, pp. 520–525, 2005.

[12] A. P. Dadi, S. Varanasi, and C. A. Schall, "Enhancement of cellulose saccharification kinetics using an ionic liquid pretreatment step," *Biotechnology and Bioengineering*, vol. 95, no. 5, pp. 904–910, 2006.

[13] M. Toda, A. Takagaki, M. Okamura et al., "Green chemistry: biodiesel made with sugar catalyst," *Nature*, vol. 438, no. 7065, p. 178, 2005.

[14] A. Onda, T. Ochi, and K. Yanagisawa, "Selective hydrolysis of cellulose into glucose over solid acid catalysts," *Green Chemistry*, vol. 10, no. 10, pp. 1033–1037, 2008.

[15] Z. Zhang and Z. K. Zhao, "Solid acid and microwave-assisted hydrolysis of cellulose in ionic liquid," *Carbohydrate Research*, vol. 344, no. 15, pp. 2069–2072, 2009.

[16] P. Hu, X. Zhang, N. Han, W. Xiang, Y. Cao, and F. Yuan, "Solution-controlled self-assembly of ZnO nanorods into hollow microspheres," *Crystal Growth & Design*, vol. 11, no. 5, pp. 1520–1526, 2011.

[17] X. Wang, H. Li, Y. Cao, and Q. Tang, "Cellulose extraction from wood chip in an ionic liquid 1-allyl-3-methylimidazolium chloride (AmimCl)," *Bioresource Technology*, vol. 102, no. 17, pp. 7959–7965, 2011.

[18] H. Wang, M. L. Maxim, G. Gurau, and R. D. Rogers, "Microwave-assisted dissolution and delignification of wood in 1-ethyl-3-methylimidazolium acetate," *Bioresource Technology*, vol. 136, pp. 739–742, 2013.

[19] K. Ninomiya, T. Yamauchi, C. Ogino et al., "Microwave pretreatment of lignocellulosic material in cholinium IL for efficient enzymatic saccharification," *Biochemical Engineering Journal*, vol. 90, no. 15, pp. 90–95, 2014.

[20] P. Hu, N. Han, D. Zhang, J. C. Ho, and Y. Chen, "Highly formaldehyde-sensitive, transition-metal doped ZnO nanorods prepared by plasma-enhanced chemical vapor deposition," *Sensors and Actuators B: Chemical*, vol. 169, pp. 74–80, 2012.

[21] L. Li, S.-T. Yu, F.-S. Liu, C.-X. Xie, and C.-Z. Xu, "Cellulose in aqueous-ionic liquid media by microwave pretreatment," *BioResources*, vol. 6, no. 4, pp. 4494–4504, 2011.

[22] S. H. Ha, N. L. Mai, G. An, and Y.-M. Koo, "Microwave-assisted pretreatment of cellulose in ionic liquid for accelerated enzymatic hydrolysis," *Bioresource Technology*, vol. 102, no. 2, pp. 1214–1219, 2011.

[23] Y. Zhang, H. Du, X. Qian, and E. Y.-X. Chen, "Ionic liquid-water mixtures: enhanced Kw for efficient cellulosic biomass conversion," *Energy & Fuels*, vol. 24, no. 4, pp. 2410–2417, 2010.

[24] A. De La Hoz, Á. Díaz-Ortiz, and A. Moreno, "Microwaves in organic synthesis. Thermal and non-thermal microwave effects," *Chemical Society Reviews*, vol. 34, no. 2, pp. 164–178, 2005.

Research Article

Effects of Preparation Conditions on the CuInS$_2$ Films Prepared by One-Step Electrodeposition Method

Rongfeng Guan,[1] Liu Cao,[2] Qian Sun,[1] and Yuebin Cao[1,3]

[1]*Key Laboratory for Advanced Technology in Environmental Protection of Jiangsu, Yancheng Institute of Technology, Jiangsu 224051, China*
[2]*Beijing Water Science Technology Institute, Beijing 100044, China*
[3]*Department of Chemical Engineering, Hanyang University, 55 Hanyangdaehak-ro, Sangnok-gu, Ansan, Gyeonggi-do 426-791, Republic of Korea*

Correspondence should be addressed to Yuebin Cao; hxxcyb@gmail.com

CuInS$_2$ thin films were prepared onto indium tin oxide (ITO) substrates by sulfurization of electrodeposited Cu$_x$In$_y$S$_z$ precursor films under S atmosphere. The influences of deposition potential, Cu^{2+}/In^{3+} ratio, sulfurization temperature, and sulfur content on the CuInS$_2$ thin films were investigated. Phases and structures were characterized by powder X-ray diffraction and Raman spectroscopy; surface morphology was characterized by Scanning Electron Microscopy; optical and electrical properties were characterized by UV-Vis absorption and Mott-Schottky curves, respectively. As a result, the optimal well-crystallized CuInS$_2$ films preparation parameters were determined to be deposition potential of −0.8 V, Cu^{2+}/In^{3+} ratio of 1.4, sulfur content of 1 g, and the sulfurization temperature of 550°C for 1 h; CuInS$_2$ thin films prepared by one-step electrodeposition present the p-type semiconductor, with thickness about 4-5 μm and their optical band gaps in the range of 1.53~1.55 eV.

1. Introduction

CuInS$_2$ is a promising material as absorber layer in photovoltaic devices owing to its direct band gap of about 1.5 eV and a high absorption coefficient, 10^5 cm^{-1} [1–3]. In addition, CuInS$_2$ is of particular interest for being environmentally friendly and cost-effective when compared to CuInSe$_2$ where the toxic and costly Se existed. Until now, the conversion efficiency of about 13% for CuInS$_2$-based solar cells has been achieved [4]. However, the value is still far below its theoretical value of 32% [5], which is mainly influenced by the quality of CuInS$_2$ film.

Preparation methods of CuInS$_2$ film mainly include sputtering [6], evaporation [7], spray pyrolysis [8, 9], chemical bath deposition [10], and electrodeposition [11–16]. Among these methods, sputtering and evaporation are two main methods for industrial production [7, 17–20]. However, expensive equipment is necessary for providing vacuum environment in the two methods, which limit their use in the production of large-area CuInS$_2$ films. Electrodeposition method has been shown to be desirable because of its advantages of low equipment cost, scalability, and manufacturability of large-area thin films. Recently, a high efficient solar cell based on electrodeposited CuInS$_2$ films is fabricated, in which the efficiency is already close to that fabricated by vacuum method [21]. There are two routes for electrodeposition method: for the one-step route, copper, indium, and sulfur are deposited simultaneously usually with sodium thiosulfate as sulfur source, metal salts as copper, and indium sources; for the two-step route, Cu-In precursor films are firstly formed by electrodeposition, and then they are sulfurized to CuInS$_2$ films in H$_2$S or S atmosphere. It seems that one-step route is more simple and environmentally benign, but the obtained CuInS$_2$ films do not always follow the exact stoichiometry of Cu : In : S = 1 : 1 : 2, usually with S deficiency in the films. Besides, easy formation of secondary phases (such as In$_2$CuO$_4$, Cu$_2$O/Cu$_2$S, CuO/CuS, and In$_2$S$_3$) is another disadvantage. Thus, it is still a challenge

to fabricate high-quality CuInS$_2$ thin films by using one-step electrodeposition route.

To solve S deficiency problem in one-step route, a further sulfurization of Cu$_x$In$_y$S$_z$ precursor films by using S powder or H$_2$S is usually conducted. To reduce the secondary phases, the operation conditions for CuInS$_2$ film fabrication such as electrodeposition potential, concentration of complexing agent, and Cu^{2+}/In^{3+} ratio need to be optimized. Until now, just few studies reported the effects of detailed operation conditions on the properties of CuInS$_2$ films prepared by one-step electrodeposition method [11, 22]. In the present study, Cu$_x$In$_y$S$_z$ precursor films firstly were electrodeposited on ITO substrates, and then they were further sulfurized in S vapor to CuInS$_2$ films. The effects of deposition potential, Cu^{2+}/In^{3+} ratio in the precursor solution, and sulfurization conditions (S content and heat treatment temperature), on the structure, morphology, and optical and electrical properties of the obtained CuInS$_2$ films were investigated in detail.

2. Experimental Section

Firstly, Cu$_x$In$_y$S$_z$ precursor films were grown on ITO glasses in a conventional three-electrode system using a PARSTAT 2273 Potentiostat. The working, counter, and reference electrodes were ITO-coated glass substrates, a platinum plate, and a saturated calomel electrode (SCE), respectively. The FTO substrates with sheet resistance of 15 Ω/square were cut into several pieces (1.5 cm × 2.5 cm) and ultrasonically cleaned in ethanol, deionized water, and acetone for 30 min, respectively. The solution bath contains 12 mM copper(II) chloride (CuCl$_2$·2H$_2$O), 6.7–10 mM indium chloride (InCl$_3$·4H$_2$O), 25 mM sodium thiosulfate (Na$_2$S$_2$O$_3$·5H$_2$O), 0.5 mM potassium chloride (KCl), and 0.1 M citric acid (C$_6$H$_8$O$_7$). C$_6$H$_8$O$_7$ was employed as a complexing agent, and KCl aqueous solution was used as a supporting electrolyte. pH of the bath solutions was adjusted to 6 using diluted ammonia solution. Deposition of the samples was carried out at room temperature for 30 min. Then the electrodeposited Cu$_x$In$_y$S$_z$ precursor films were further sulfurized by S powders at temperatures 400–550°C in a self-made sealed tubular furnace under the protection of Ar atmosphere.

Phases and crystal structures of the thin films were characterized by X-ray diffraction (XRD), with a German Bruker AXS D8 advanced diffractometer, and Cu Kα radiation at 40 kV and 40 mA. Raman spectroscopy was measured using an InVia laser confocal Raman spectroscopy system of England Renishaw company. Scanning Electron Microscopy (SEM) was measured using a JEOL JSM-6390 LV microscope. UV-Vis absorption spectrum was measured in the wavelength range of 300~900 nm using UV-2450 UV-visible spectroscopy system. Mott-Schottky curve was measured in a mixed solution of 0.2 M KCl and 0.5 M EDTA with frequency 1 KHz, scan range −0.9 to −0.4 V, and scan rate 3 mV/s.

3. Results and Discussions

3.1. Effects of Deposition Potential. In the one-step electrodeposition method, for depositing Cu-In-S simultaneously, complexing agent for narrowing the redox potentials is
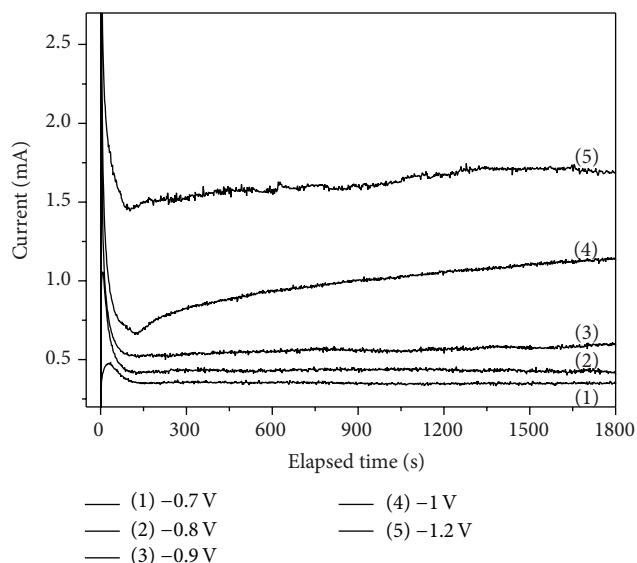

FIGURE 1: The deposition currents as a function of times at various deposition potentials (−0.7, −0.8, −0.9, −1.0, and −1.2 V).

needed. It was reported that citric acid can work as the complexing agent for narrowing the redox potentials of Cu^{2+}/Cu and In^{3+}/In [23]. Moreover, citric acid can complex with both Cu^{2+} and In^{3+}, which will prevent the precipitation of metal hydroxide over a wide pH range. We previously studied the effects of citric acid concentrations on the redox properties of Cu^{2+} and In^{3+}, and the optimal concentration was determined to be citric acid:Cu^{2+} 8.5 as we used here.

Figure 1 shows the deposition current as a function of time at various potentials. The deposition current increases with increasing deposition potentials. At any deposition potentials, the current decreases suddenly within initial 2 min, which is the result of concentration gradients developed in the boundary layer close to an electrode surface at short times at initial deposition period [16]. After initial period, the currents at deposition potentials −0.7, −0.8, and −0.9 V are stable, while the currents at potentials −1.0 and −1.2 V increased gradually. It may be because the large deposition rate at high potentials induces the roughness of the electrode surface and deposition area increases and hence the deposition current increases. At −1.0 and −1.2 V, upper layers of Cu$_x$In$_y$S$_z$ films exfoliated during the deposition process due to the weak adhesive force caused by their large deposition rate.

Figure 2 shows the morphology of Cu$_x$In$_y$S$_z$ films deposited at various potentials. All the films are composed of aggregated particles. The films deposited at −0.7 V contain two kinds of particles: secondary particles with large size of around 2-3 μm and primary particles in nanoscale. For the films deposited at −0.8 and −0.9 V, they both are composed of aggregated particles, with a relative uniform particles size distribution at around 1 μm. The films deposited at −0.8 V are more compact and smooth than that deposited at −0.9 V. Thus, the potential −0.8 V is more proper for Cu$_x$In$_y$S$_z$ film deposition. As the upper layers of Cu$_x$In$_y$S$_z$ films deposited

(a)

(b)

(c)
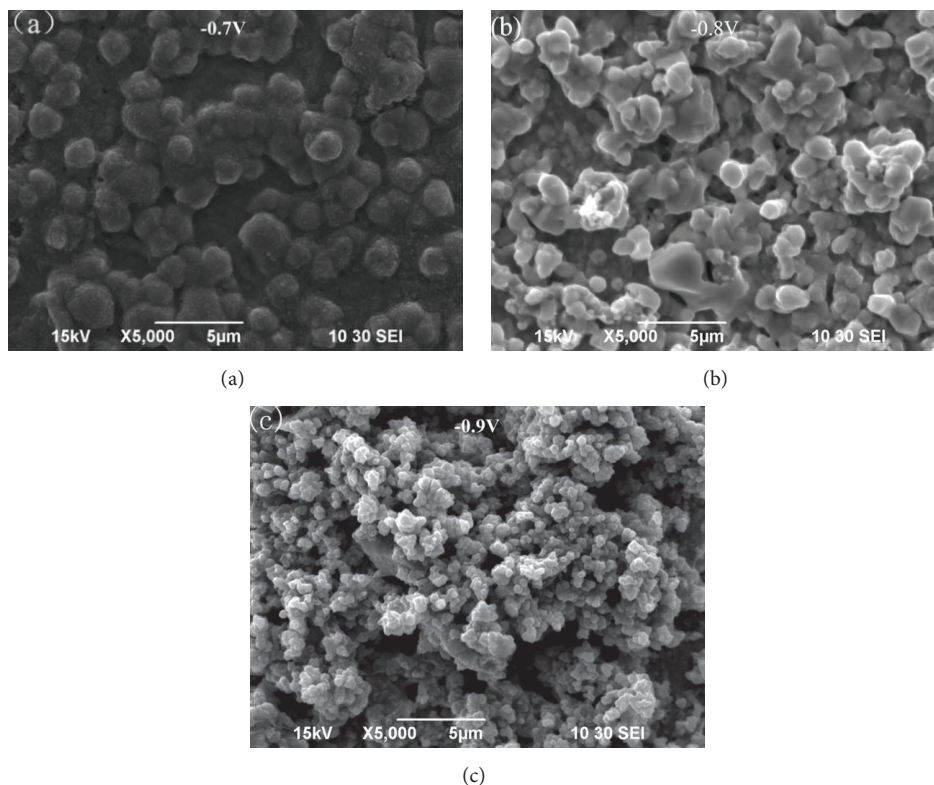
FIGURE 2: SEM images of CuInS$_2$ thin films obtained at deposition potentials −0.7 V (a), −0.8 V (b), and −0.9 V (c).

at −1.0 and −1.2 V are easily exfoliated, their SEM images are not shown here.

3.2. Effects of Sulfurization Parameters. As we mentioned above, CuInS$_2$ films were obtained through one-step electrodeposition method usually with S deficiency. Thus Cu$_x$In$_y$S$_z$ precursor films were further sulfurized, and the effects of sulfurization parameters on CuInS$_2$ film properties were investigated. Cu$_x$In$_y$S$_z$ precursor films were deposited together with a certain amount of S powders in a tube furnace with argon flow during the sulfurization process to avoid air oxidation.

3.2.1. Effects of S Content. Figure 3(a) presents the XRD pattern of CuInS$_2$ films sulfurized at various S contents with sulfurization temperature at 550°C. All CuInS$_2$ films were chalcopyrite structure, with no evidence of other phases, indicating that CuInS$_2$ films were near stoichiometric. All the films show the (112) plane preferred orientation. The peak intensity of CuInS$_2$ films obtained at S contents 0.5 and 1 g is much higher than that obtained at S contents 1.25 and 1.5 g, which indicates the higher crystallization of CuInS$_2$ films sulfurized at low S vapor concentrations.

Raman spectroscopy can be used as a complementary technique to XRD. For CuInS$_2$, there are three structure orders which belong to different space groups, chalcopyrite (CH) structure and CuAu (CA) and CuPt (CP) metastable structures. Because the formation energy of CP structure is

high, it is unlikely present in our CuInS$_2$ films. CA structure is undesirable, and it is difficult to identify it using XRD. The Raman A1 mode of CH structure is centered at 290 cm^{-1}, while the Raman A1 mode of metastable CA structure is centered at around 305 cm^{-1}. The chalcopyrite structure therefore can be identified using Raman analysis. Figure 3(b) shows the Raman spectra of CuInS$_2$ films obtained at various S contents. The peak of 287 cm^{-1} appearing at all samples is closer to the A1 mode of CH structure (290 cm^{-1}) [24], indicating the presence of CH structure. Similar to the XRD results, high peaks intensity of CuInS$_2$ films obtained at 0.5 and 1 g indicates their high crystallization. For all the films, there is no evidence for the presence of CA structure whose A1 mode appears at around 305 cm^{-1} [25]. The peak at 470 cm^{-1} for the film obtained at S content 0.5 g can be attributed to Cu$_{2-x}$S. Cu$_{2-x}$S phase which can be removed by etching the film in KCN solution.

Optical properties of the films were studied by absorption measurements with a UV/visible/NIR spectrophotometer. Figure 4 shows the absorption spectra of CuInS$_2$ films in the range of 400–900 nm. CuInS$_2$ film obtained at S content 1 g exhibits the largest absorption. All the films show a fundamental absorption wavelength at around 800–810 nm, which is similar to the reported values [15]. According to the absorbance spectra, the plots of $(\alpha h\nu)^2$ against $h\nu$ can be obtained, in which α is the absorbance coefficient. The band gap E_g can be estimated from the intercept of the linear portion of the plots on x-axis. Figure 4(b) shows $(\alpha h\nu)^2$ as a
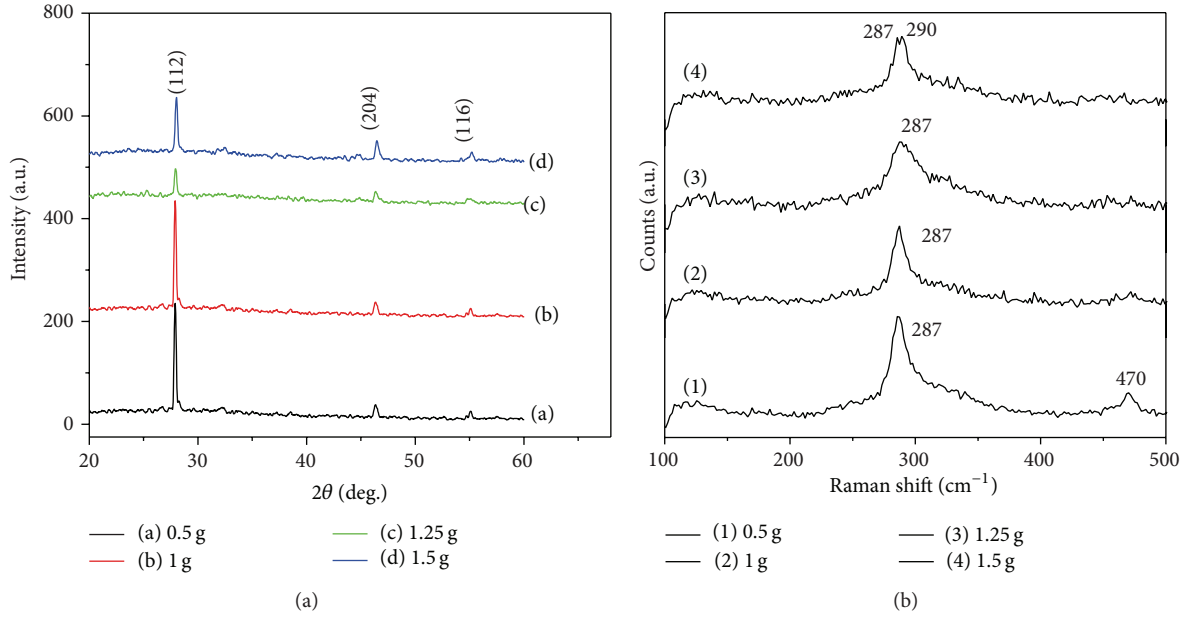
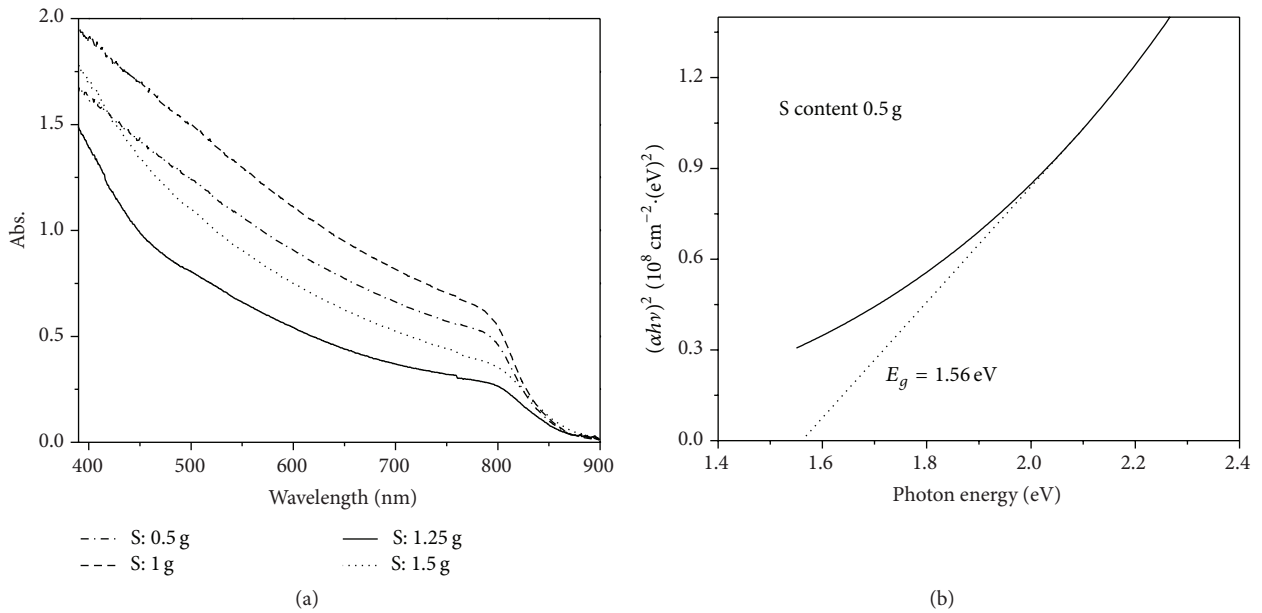FIGURE 3: XRD (a) and Raman spectra (b) of CuInS$_2$ films obtained at S contents 0.5, 1, 1.25, and 1.5 g.

FIGURE 4: (a) UV-Vis absorption spectra of CuInS$_2$ films obtained at S contents 0.5, 1, 1.25, and 1.5 g; (b) $(\alpha h\nu)^2$ of CuInS$_2$ film obtained at S content 0.5 g as a function of $h\nu$.

function of $h\nu$ for CuInS$_2$ film obtained at S content 0.5 g. E_g of CuInS$_2$ film obtained at S content 0.5 g is determined to be 1.56 eV.

3.2.2. Effects of Annealing Temperature.

Figure 5(a) shows the XRD patterns of CuInS$_2$ films heat treated at various temperatures with S content 1 g. When the temperature increased from 400 to 450°C, the intensity of CuInS$_2$ peak at (112) planes greatly enhanced, indicating its enhanced crystallization. When annealing temperature further increased to 500 and 550°C, the peak intensity decreased, which means the crystalization decreased at high temperature. Raman spectra of CuInS$_2$ films annealed at various temperatures are shown in Figure 5(b), in which all CuInS$_2$ films except the one annealed at 550°C contain Cu$_{2-x}$S phase. From the results of XRD and Raman, it can be concluded that 550°C is a prefferred annealing temperatre for Cu$_x$In$_y$S$_z$ films sulfurazation.
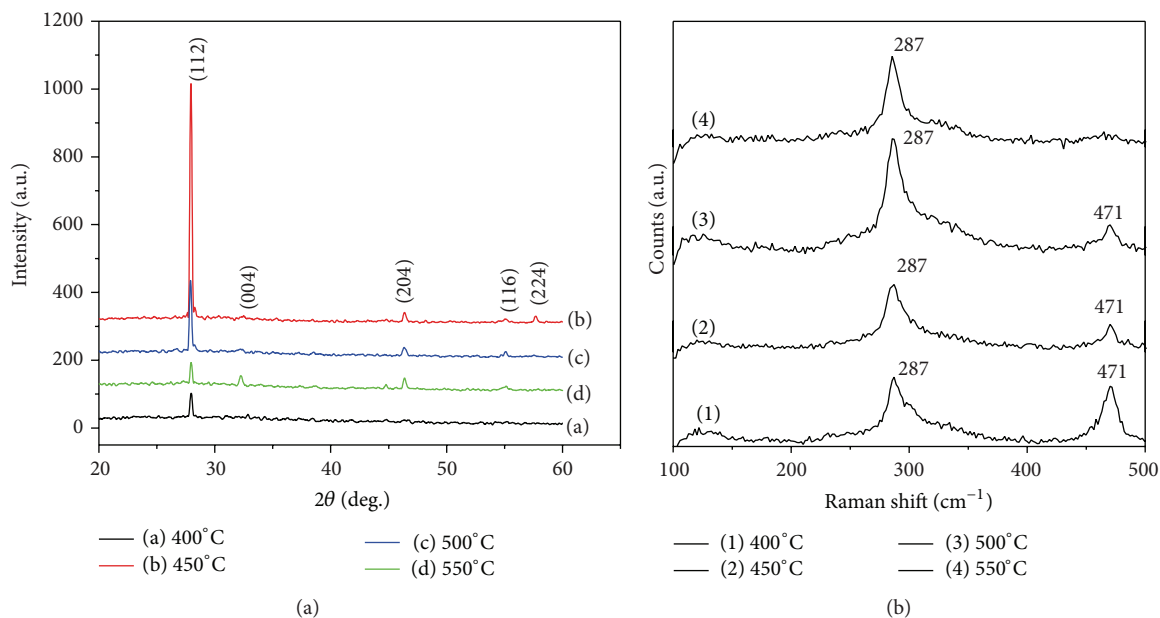
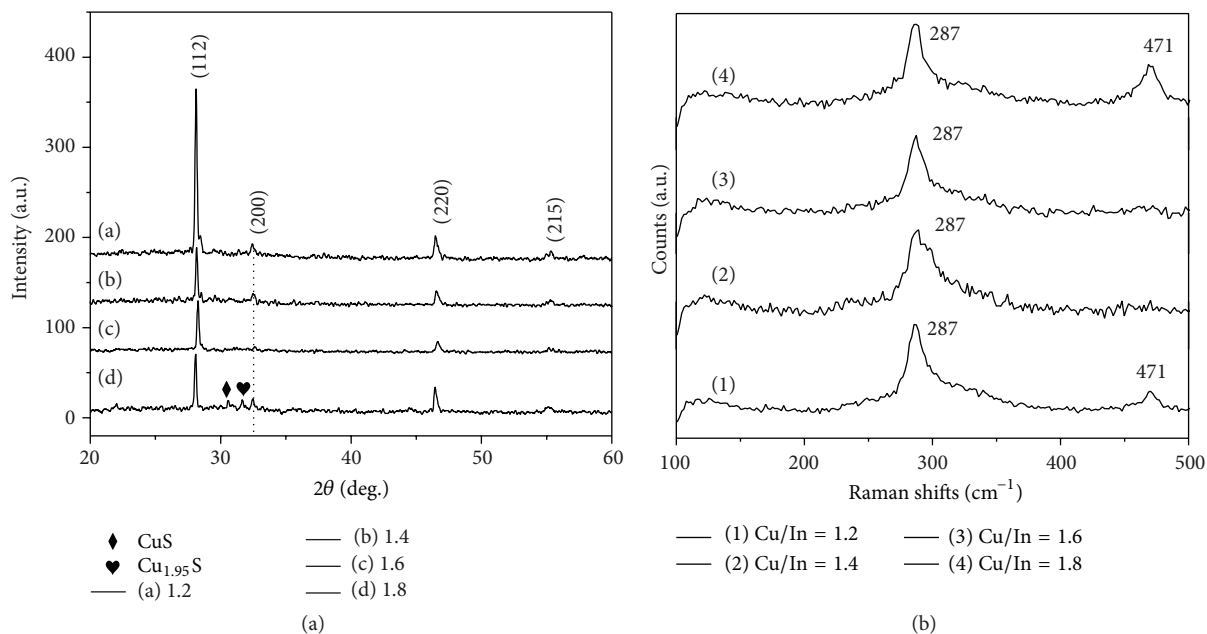FIGURE 5: XRD (a) and Raman (b) spectra of CuInS$_2$ films annealed at temperatures 400°C, 450°C, 500°C, and 550°C.

FIGURE 6: XRD (a) and Raman spectra (b) of CuInS$_2$ films obtained at Cu^{2+}/In^{3+} 1.2, 1.4, 1.6, and 1.8.

3.3. Effects of Cu^{2+}/In^{3+} Ratios. Cu^{2+}/In^{3+} ratio in precursor solution is a crucial parameter in determining the properties of synthesized CuInS$_2$ films. Here, the effects of Cu^{2+}/In^{3+} ratio in solution on CuInS$_2$ film phases, morphologies, and optical properties are investigated. **Figure 6(a)** shows the XRD patterns of CuInS$_2$ films prepared at various Cu^{2+}/In^{3+} ratios. All the films, except the film obtained at Cu^{2+}/In^{3+} ratio 1.8, are chalcopyrite structure without observable other phases. For CuInS$_2$ film obtained at Cu^{2+}/In^{3+} ratio 1.8, there are other phases including CuS and Cu$_{1.95}$S as labelled in

the (d) curve of **Figure 6(a)**. Raman spectra as shown in **Figure 5(b)** also indicate that Cu$_{2-x}$S phase is present in the film obtained at Cu^{2+}/In^{3+} ratio 1.8, as the peak at 471 cm^{-1} which is a typical peak from Cu$_{2-x}$S existed. From the Raman spectrum, it can be seen that the film obtained at Cu^{2+}/In^{3+} ratio 1.2 also contained Cu$_{2-x}$S, although it was not detected in XRD measurement.

SEM images of CuInS$_2$ films obtained at Cu^{2+}/In^{3+} ratios 1.4 and 1.6 are shown in **Figure 7**. The plane and cross-sectional images of CuInS$_2$ film obtained at Cu^{2+}/In^{3+} ratios
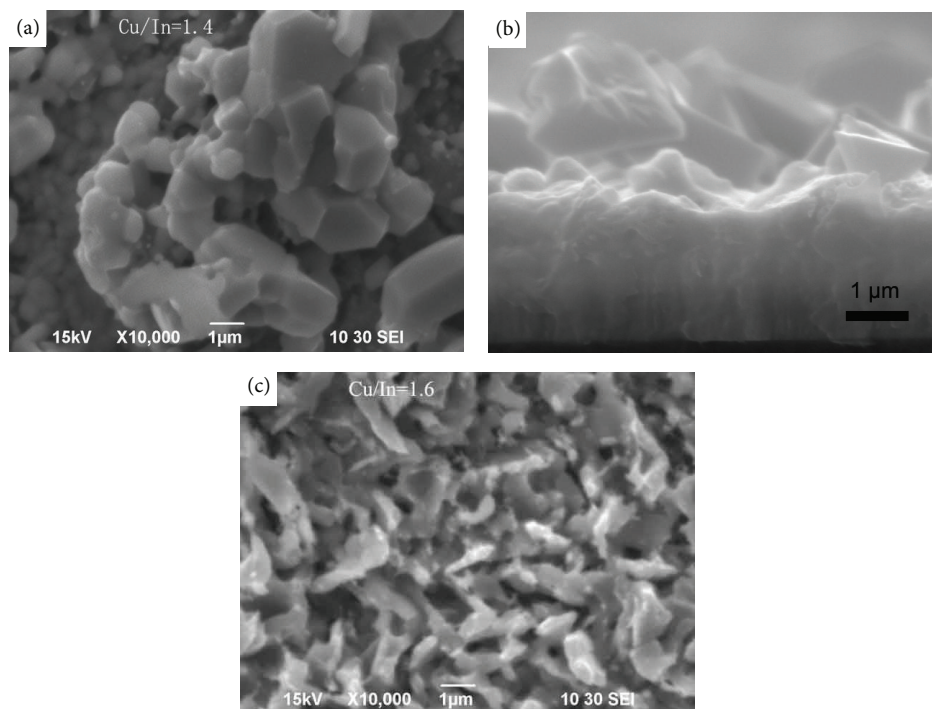
FIGURE 7: SEM images of CuInS$_2$ thin films obtained at Cu^{2+}/In^{3+} ratio 1.4 (a) plane view, (b) cross-section view, and Cu^{2+}/In^{3+} ratio 1.6 (c).
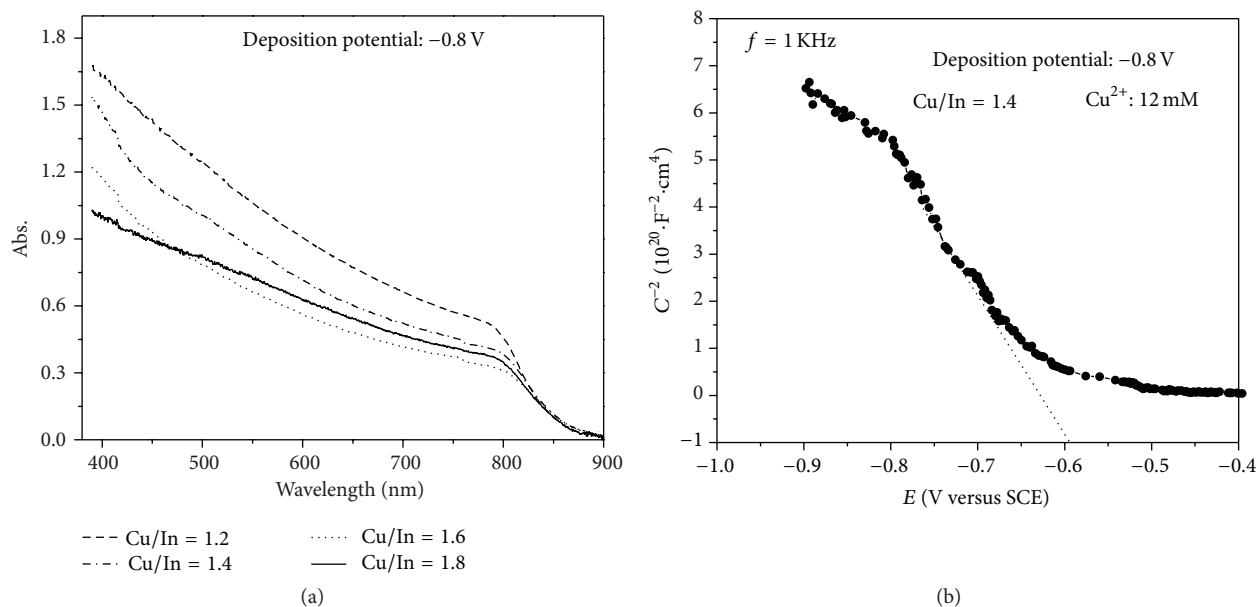

FIGURE 8: (a) UV-Vis absorption spectra of CuInS$_2$ films obtained at various Cu^{2+}/In^{3+} ratios; (b) Mott-Schottky curve of CuInS$_2$ thin films obtained at Cu^{2+}/In^{3+} ratio 1.4.

1.4 indicate that the film can be divided into two layers: the condensed bottom layer with thickness of around 2 μm and the incompact upper layer with large crystals. Large crystals of the upper layer may be caused by the sulfurization process. It can be seen from Figures 7(a) and 7(c) that crystal size of the film obtained at Cu^{2+}/In^{3+} ratio 1.4 is much larger than that obtained at Cu^{2+}/In^{3+} ratio 1.6 and the surface of

the film obtained at Cu^{2+}/In^{3+} ratio 1.4 is more condense than that obtained at Cu^{2+}/In^{3+} ratio 1.6. The condensed film and large crystals mean reduced cracks and grain boundaries in the film which will increase photocurrent because the traps for electrons and holes are reduced. Thus, the film obtained at Cu^{2+}/In^{3+} ratio 1.4 has the potential to be an effective absorber layer for solar cells. As there are Cu$_{2-x}$S phases in

the films obtained at Cu^{2+}/In^{3+} ratio 1.2 and 1.8, we did not show their SEM images here.

In solution-based processes carbon contamination is an important issue for $CuInS_2$ film fabrication. EDS was used to determine the carbon content, and it indicates that the carbon is 3.5 at% in $CuInS_2$ film obtained at Cu^{2+}/In^{3+} ratio 1.4. We estimate that the carbon contamination may come from citrate used in solution.

Figure 8(a) shows the absorption spectra of $CuInS_2$ films obtained at various Cu^{2+}/In^{3+} ratios. $CuInS_2$ film obtained at Cu^{2+}/In^{3+} ratio 1.2 shows the largest absorption; and all the films have a similar fundamental absorption wavelength at around 800–810 nm, caused by their band gaps. Figure 8(b) shows the Mott-Schottky (MS) plots for $CuInS_2$ film obtained at Cu^{2+}/In^{3+} ratio 1.4. It can be determined that the film is p-type semiconductor due to the negative slope of the curve. According to the intercept on the potential axis, the flat band potential is determined to be −0.6 V.

4. Conclusions

$CuInS_2$ films of chalcopyrite structure were prepared by one-step electrodeposition of $Cu_xIn_yS_z$ precursor films, followed by sulfurization. Effects of operation parameters including deposition potential, sulfurization conditions, Cu^{2+}/In^{3+} ratio on the structure, morphology, and optical and electrical properties of the obtained $CuInS_2$ films were studied. Based on the surface morphology, crystallization, phases purity, and optical absorption property, the optimized deposition potential was determined to be −0.8 V, Cu^{2+}/In^{3+} ratio 1.4, sulfur content 1 g, and sulfurization temperature 550°C. The obtained $CuInS_2$ thin films prepared here present p-type semiconductor, with thickness about 4-5 μm and optical band gaps 1.53–1.55 eV.

Conflict of Interests

The authors declare that there is no conflict of interests regarding the publication of this paper.

Acknowledgments

References

[1] S. M. Hosseinpour-Mashkani, M. Salavati-Niasari, and F. Mohandes, "$CuInS_2$ nanostructures: synthesis, characterization, formation mechanism and solar cell applications," *Journal of Industrial and Engineering Chemistry*, vol. 20, no. 5, pp. 3800–3807, 2014.

[2] B. D. Weil, S. T. Connor, and Y. Cui, "$CuInS_2$ solar cells by air-stable ink rolling," *Journal of the American Chemical Society*, vol. 132, no. 19, pp. 6642–6643, 2010.

[3] J. S. Ward, K. Ramanathan, F. S. Hasoon et al., "A 21·5% efficient Cu(In,Ga)Se$_2$ thin-film concentrator solar cell," *Progress in Photovoltaics: Research and Applications*, vol. 10, no. 1, pp. 41–46, 2002.

[4] H. Goto, Y. Hashimoto, and K. Ito, "Efficient thin film solar cell consisting of TCO/CdS/$CuInS_2$/CuGaS$_2$ structure," *Thin Solid Films*, vol. 451-452, pp. 552–555, 2004.

[5] T. Nakabayashi, T. Miyazawa, Y. Hashimoto, and K. Ito, "Over 10% efficient $CuInS_2$ solar cell by sulfurization," *Solar Energy Materials & Solar Cells*, vol. 49, no. 1–4, pp. 375–381, 1997.

[6] J. Schulte, S. Brunken, and K. Ellmer, "Nucleation and phase formation during reactive magnetron co-sputtering of Cu(In,Ga)S$_2$ films, investigated by *in situ* EDXRD," *Journal of Crystal Growth*, vol. 384, pp. 114–121, 2013.

[7] P. Rao, S. Kumar, and N. K. Sahoo, "Growth of copper indium sulphide films by thermal evaporation of mixtures of copper sulphide and indium sulphide powders," *Materials Research Bulletin*, vol. 48, no. 8, pp. 2915–2921, 2013.

[8] R. R. Prabhakar, S. S. Pramana, K. R. G. Karthik, C. H. Sow, and K. B. Jinesh, "Ultra-thin conformal deposition of CuInS2 on ZnO nanowires by chemical spray pyrolysis," *Journal of Materials Chemistry*, vol. 22, no. 28, pp. 13965–13968, 2012.

[9] J. C. W. Ho, T. Zhang, K. K. Lee, S. K. Batabyal, A. I. Y. Tok, and L. H. Wong, "Spray pyrolysis of CuIn(S,Se)$_2$ solar cells with 5.9% efficiency: a method to prevent Mo oxidation in ambient atmosphere," *ACS Applied Materials and Interfaces*, vol. 6, no. 9, pp. 6638–6643, 2014.

[10] F. Cui, L. Wang, Z. Xi, Y. Sun, and D. Yang, "Fabrication and characterization of $CuInS_2$ films by chemical bath deposition in acid conditions," *Journal of Materials Science: Materials in Electronics*, vol. 20, no. 7, pp. 609–613, 2009.

[11] L. Lu, Y. Wang, and X. Li, "Influence of processing parameters on the preparation of $CuInS_2$ thin film by one-step electrodeposition as the solar cell absorber," *Surface & Coatings Technology*, vol. 212, pp. 55–60, 2012.

[12] S. M. Lee, S. Ikeda, T. Yagi, T. Harada, A. Ennaoui, and M. Matsumura, "Fabrication of CuInS2 films from electrodeposited Cu/In bilayers: effects of preheat treatment on their structural, photoelectrochemical and solar cell properties," *Physical Chemistry Chemical Physics*, vol. 13, no. 14, pp. 6662–6669, 2011.

[13] X. Xu, F. Wang, J. Liu, and J. Ji, "Effect of potassium hydrogen phthalate ($C_8H_5KO_4$) on the one-step electrodeposition of single-phase $CuInS_2$ thin films from acidic solution," *Electrochimica Acta*, vol. 55, no. 15, pp. 4428–4435, 2010.

[14] K.-W. Cheng and W.-H. Chiang, "Effect of [Cu]/[Cu + In] ratio in the solution bath on the growth and physical properties of $CuInS_2$ film using one-step electrodeposition," *Journal of Electroanalytical Chemistry*, vol. 661, no. 1, pp. 57–65, 2011.

[15] Y.-C. Chen, J.-B. Shi, P.-F. Wu, C.-J. Chen, and S.-Y. Yang, "Synthesis and optical properties of CuInS2 thin films prepared by sulfurization of electrodeposited Cu-In layers," *Crystal Research and Technology*, vol. 47, no. 9, pp. 991–996, 2012.

[16] J. L. Yuan, C. Shao, L. Zheng et al., "Fabrication of $CuInS_2$ thin film by electrodeposition of Cu-In alloy," *Vacuum*, vol. 99, pp. 196–203, 2014.

[17] R. F. Guan, X. X. Wang, and Q. Sun, "Structural and optical properties of $CuInS_2$ thin films prepared by magnetron sputtering and sulfurization heat treatment," *Journal of Nanomaterials*, In press.

[18] R. Cayzac, F. Boulc'h, M. Bendahan, P. Lauque, and P. Knauth, "Direct preparation of crystalline $CuInS_2$ thin films by radiofrequency sputtering," *Materials Science and Engineering B*, vol. 157, no. 1–3, pp. 66–71, 2009.

[19] M. Nie and K. Ellmer, "Growth and morphology of thin $Cu(In,Ga)S_2$ films during reactive magnetron co-sputtering," *Thin Solid Films*, vol. 536, pp. 172–178, 2013.

[20] C.-H. Tsai, D. K. Mishra, C.-Y. Su, and J.-M. Ting, "Effects of sulfurization and Cu/In ratio on the performance of the $CuInS_2$ solar cell," *International Journal of Energy Research*, vol. 38, no. 4, pp. 418–428, 2014.

[21] C. Broussillou, M. Andrieux, M. Herbst-Ghysel et al., "Sulfurization of Cu-In electrodeposited precursors for $CuInS_2$-based solar cells," *Solar Energy Materials and Solar Cells*, vol. 95, no. 1, pp. S13–S17, 2011.

[22] Y. Tang, Y. H. Ng, and R. Amal, "Investigating the preparation parameters during the synthesis of CuInS2 thin film photoelectrodes," in *Proceedings of the International Conference on Nanoscience and Nanotechnology (ICONN '14)*, pp. 7–9, February 2014.

[23] J. Herrero and J. Ortega, "Electrodeposition of Cu-In alloys for preparing $CuInS_2$ thin films," *Solar Energy Materials*, vol. 20, no. 1-2, pp. 53–65, 1990.

[24] J. Álvarez-García, J. Marcos-Ruzafa, A. Pérez-Rodríguez, A. Romano-Rodríguez, J. R. Morante, and R. Scheer, "MicroRaman scattering from polycrystalline $CuInS_2$ films: structural analysis," *Thin Solid Films*, vol. 361, pp. 208–212, 2000.

[25] J. Alvarez-García, A. Pérez-Rodríguez, B. Barcones et al., "Polymorphism in $CuInS_2$ epilayers: origin of additional Raman modes," *Applied Physics Letters*, vol. 80, no. 4, pp. 562–564, 2002.

Research Article

Structural and Optical Properties of CuInS$_2$ Thin Films Prepared by Magnetron Sputtering and Sulfurization Heat Treatment

Rongfeng Guan,[1] Xiaoxue Wang,[2] and Qian Sun[1]

[1]*Laboratory for Advanced Technology in Environmental Protection of Jiangsu Province, Yancheng Institute of Technology, Yancheng, Jiangsu 224051, China*
[2]*School of Physics and Chemistry, Henan Polytechnic University, Jiaozuo, Henan 454000, China*

Correspondence should be addressed to Rongfeng Guan; rongfengg@163.com

CuInS$_2$ thin films were prepared by sulfurization of Cu-In precursor films through magnetron sputtering and the resulting films characterized using X-ray diffraction, Raman spectrometry, and UV-Vis spectrophotometry. The results demonstrate that a sputtering power of 80–120 W is more suitable for sputtered Cu-In precursor films and can be used to obtain CuInS$_2$ films with good crystallinity through vulcanization heat treatment. The sputtering gas pressure and sulfurization temperature were shown to impact on the film quality due to improper processes during the CuInS$_2$ phase. Some of the CuIn$_{11}$S$_{17}$ and CuS$_2$ impurities were observed in the composition of the prepared CuInS$_2$ thin films. Optimization of process parameters obtained from the experimental data was determined as a sputtering power of 80~120 W, a sputtering gas pressure of 0.6–0.8 Pa, a heat treatment temperature of 450~470°C, and a holding time of 2~3 hours. The optical band gap obtained for CuInS$_2$ thin films is between 1.48 and 1.5 eV.

1. Introduction

Copper indium disulfide (CuInS$_2$) is a ternary (I–III–VI) semiconductor with a direct band gap and a sulfide fullerene-like structure which belongs to groups II–VI replacing the copper and indium ions in group II. It has a chalcopyrite configuration with a phase transition temperature of 980°C. CuInS$_2$ has various advantages with a narrow band gap of 1.50 eV making it insensitive to temperature with good stability. It has high absorption coefficients, mostly at 10^5/cm, and can absorb 90% of sunlight for films of 1 to 2 μm thickness. All these advantages make CuInS$_2$ one of the most promising alternative absorbing semiconductor materials for the development of thin film solar cells [1–3].

CuInS$_2$ has anti-interference properties, a strong ability to resist radiation, a long service life, and lower toxic species compared to CuInSe$_2$. It has much potential as a thin film solar cell absorption material of the chalcopyrite semiconductors [4]. The theoretical efficiency for a CuInS$_2$ thin film solar cell is between 28 and 32% [5], but the

highest conversion efficiency observed in the laboratory is only 13% [6, 7], which is significantly less than the predicted theoretical value. In the past few years, various methods of CuInS$_2$ synthesis have been reported including magnetron sputtering [8], spray pyrolysis [9, 10], ion layer gas reaction [11], chemical bath deposition [12], and electrodeposition [13–15]. For each of the above methods, magnetron sputtering has shown the most promise for the realization of thin film solar cells based on CuInS$_2$ for large-scale production. It is reported that Germany have established a thin film solar cell production line with battery conversion efficiency reaching 7.6% [16]. There are two main techniques of magnetron sputtering to obtain CuInS$_2$ thin film [17, 18]; one is the sputtering deposition of CuInS$_2$ thin film also containing the target Cu-In-S under the high vacuum. Under the same sputtering power and sputtering pressure, different elements of sputtering energy can be different, so it is therefore difficult to control the chemical composition. The other technique is sputtering Cu-In thin film with appropriate H$_2$S flow using a flow meter to control flow rate. The copper and indium atoms

TABLE 1: Different process parameters of samples synthesized by different sputtering power.

Sputtering power/W	Gas pressure/Pa	Target voltage/V	Target current/A	Deposition time/min	Treating temperature/°C	Holding time/h	Sulfur weight/g
80	0.4	566	0.14	20	500	2	1
100	0.4	531	0.19	20	500	2	1
120	0.4	573	0.21	20	500	2	1
140	0.4	560	0.25	20	500	2	1
160	0.4	570	0.28	20	500	2	1

continue to react with H_2S whilst sputtering on the substrate and finally forming a sulfide film. The difficulty associated with this method is the influence of the temperature and that H_2S is an inflammable, explosive, toxic gas which increases associated risks. In this paper, $CuInS_2$ thin films were prepared by sulfurization of Cu-In preformed films created by magnetron sputtering onto glass substrates. In the sulfurization process, solid sulfur powder was used as the sulfur source instead of H_2S. The effects of sputtering power, gas pressure, sulfurization temperature, and sulfurization time on the structural and optical properties of the $CuInS_2$ samples were determined.

2. Materials and Methods

2.1. Preparation of CuInS$_2$ Thin Film. The substrate was a high purity glass (99.99%) target with Cu-In alloy at a Cu/In atomic ratio of 1 : 1. This was in the size of $\Phi50\,mm * 4\,mm$. Argon was used as the sputtering gas with a distance of 8 cm between the target and substrate. First, the Cu-In precursor films were deposited on the substrate. The prepared precursor films were placed at high temperature in a tubular resistance furnace to prepare a $CuInS_2$ thin film by sulfurization heat treatment using argon gas as a protective gas to ventilate the tubular furnace.

2.2. Characterization. The crystalline phases of the samples were identified by laser confocal Raman spectroscopy system (Renishaw) and powder X-ray diffraction (XRD) measurements obtained using a D8 ADVANCE diffractometer with a Cu K_α radiation source (λ = 0.15406 nm). Data were collected over 2θ = 5–90°. The absorption spectra were investigated using a UV-Vis spectrometer (UV-2450) and the thickness of the films was investigated using a metallographic microscope (Olympus, ck40-M-F200) with image analyzer (Vms-2000).

3. Results and Discussion

3.1. The Influence of DC Sputtering Power on CuInS$_2$ Thin Films. The divided voltage of sputtering gas, the distance between target material and substrate, and the sputtering power were shown to be the influential factors on sputtering rate. Under the same conditions, with increasing sputtering power, the energy of incident ions was shown to increase. The deposition rate concerns the energy, quality, and incidence direction of the incident ions. Therefore, sputtering power
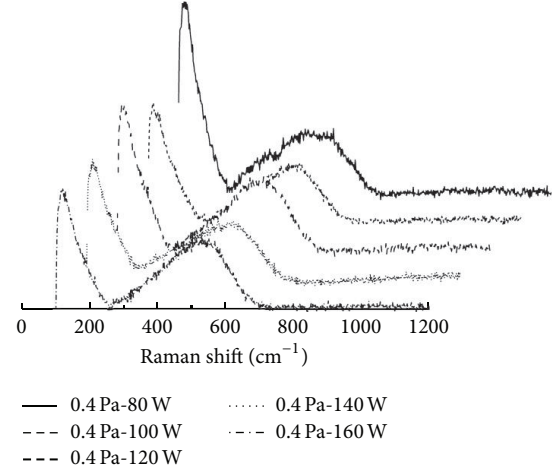

FIGURE 1: Raman spectra of the Cu-In thin films with different sputtering power before sulfuration.

is the main influential factor in controlling the deposition rate. In order to optimize the sputtering power, a working pressure of 0.4 Pa, and argon gas flow of 11 SCCM (standard mL/min), changes in sputtering power of 80, 100, 120, 140, and 160 W were observed. Table 1 shows the process parameters of coating and heat treatment.

Figure 1 shows the Raman spectra of Cu-In precursor films deposited at different sputtering powers. From the figure, it can be seen that the Raman spectra of Cu-In films have similar shapes, with wide spectra with wave numbers ranging from $230\,cm^{-1}$ to $700\,cm^{-1}$. The results show low crystallinity as the Raman spectra are generated by molecular vibrations and atomic and interatomic forces acting on the alloy film. Consequently, some peaks are wide and the crystallinity is low. Cu-In films are required to react with sublimed sulfur during heat treatment making the sulfur be embedded into the films to form new phases and allow the crystals to regrow.

Figure 2 shows the Raman spectra of $CuInS_2$ thin films during sulfurization. Compared with Figure 1, new peaks with wave numbers in the range of $250\sim400\,cm^{-1}$ are evident. For a sputtering power of 80 W, the Raman peak located at $298\,cm^{-1}$ is consistent with the $CuInS_2$ chalcopyrite phase. When the sputtering powers are set to 100 and 120 W, corresponding Raman peaks occur at $313\,cm^{-1}$ and $313\,cm^{-1}$. When the sputtering power is changed to 140 and 160 W,

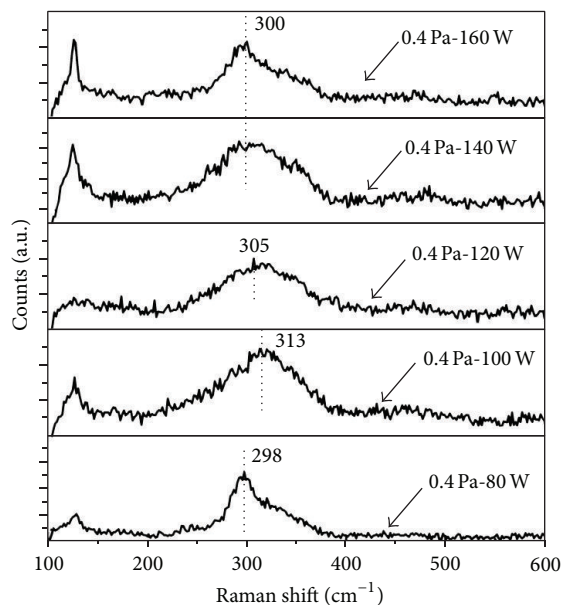FIGURE 2: Raman spectra of the CuInS$_2$ thin films with different sputtering power.
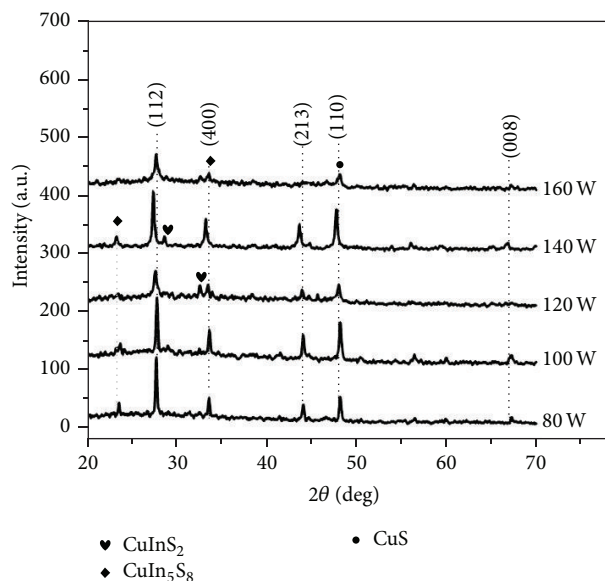

♥ CuInS$_2$ • CuS
♦ CuIn$_5$S$_8$

FIGURE 3: XRD spectra of the CuInS$_2$ thin films with different sputtering power (80 W, 100 W, 120 W, 140 W, and 160 W).

the Raman peaks are both located at 300 cm^{-1}, with a large FWHM (Full Width at Half Maximum) indicating more impurity in the phases and lower crystallinity compared with chalcopyrite CuInS$_2$.

Figure 3 shows the XRD spectra of the CuInS$_2$ thin films with different sputtering power (specifically 80, 100, 120, 140, and 160 W). The peaks in the XRD patterns for the samples are well matched with CuInS$_2$ (JCPDS number 65-1572), CuIn$_5$S$_8$ (JCPDS number 54-0554), and CuS (JCPDS number 65-3928). At sputtering powers of 80, 100, and 120 W, the $2\theta = 27.8°$, 44°, and 67.3° are consistent with 112, 213, and

008 of CuInS$_2$ in the indices of lattice planes. For a sputtering power of 140 W, $2\theta = 28.9°$, 44°, and 67.3° are consistent with 103, 213, and 008 of CuInS$_2$ in the indices of lattice planes. At a sputtering power of 160 W, $2\theta = 27.8°$, 67.3° are consistent with 112 and 008 of CuInS$_2$ in the indices of lattice planes.

In addition to the characteristic diffraction peak of CuInS$_2$, the diffraction peaks of the CuS and CuIn$_5$S$_8$ phases are shown in Figure 3. All diffraction data were collected over $2\theta = 33.3°$ with the crystal face index 400 consistent with the characteristic diffraction peak of CuIn$_5$S$_8$. Other diffraction data were collected over $2\theta = 48.2°$ with the crystal face index 110 being consistent with the characteristic diffraction peak of CuS. There is not only the CuInS$_2$ phase but also CuS and CuIn$_5$S$_8$ phases that coexist in the film. This is due to Cu and S combining to form the CuS phase and In and S combining to form the In$_2$S$_3$ phase. CuS and In$_2$S$_3$ then further react on the surface of the thin film to form the CuS and CuIn$_5$S$_8$ phases. The diffraction spectra obtained at sputtering powers of 140 and 160 W have significant differences compared to the diffraction spectra of CuInS$_2$ (JCPDS number 65-1572). This may be due to the high sputtering power causing Cu and In to be accumulated too rapidly with uneven distribution of the elements. The formation of new phase disorders results in more lattice defects being produced when sulfur is embedded into the defective lattice and consequently generates the impurity phases. In conclusion, sputtering powers from 80 to 120 W are suitable to sputter the Cu-In precursor.

3.2. The Influence of Sputtering Gas Pressure on the Crystalline of Thin Films. As argon is used as the sputtering gas, the sputtering gas pressure is the partial pressure of argon in the vacuum chamber, the flow rate of which is controlled by a mass flow controller. The greater the argon flow rate value, the greater the sputtering gas pressure which is associated with the quality of thin films. The sputtering gas pressure ranges from 0.3 Pa to 0.8 Pa in the experiment. The process parameters of Cu-In preformed films were as follows: sputtering power was 80 W, the target voltage was 500 V, the target current was 0.16 A, and the argon gas flow was controlled at 11 SCCM, 16 SCCM, and 19 SCCM, which is consistent with the sputtering gas pressures of 0.4, 0.6, and 0.8 Pa in the coating chamber. The heat treating parameters were as follows: sulfurization temperature was 450°C, holding time was 3 hours, and the mass of sulfur was 2 g.

Figure 4 shows the Raman spectra of the CuInS$_2$ thin films obtained at different sputtering gas pressures. The Raman peak located at 298 cm^{-1} is consistent with the typical CuInS$_2$ chalcopyrite structure. When the sputtering gas pressure was set to 0.4 Pa, a Raman peak of 301 cm^{-1} which is next to the right side of 298 cm^{-1} emerged illustrating that the thin films prepared with the sputtering power in 0.4 Pa are a solid mixture of chalcopyrite and Cu-Au phases as the Raman FWHM value of Cu-Au phase is in the range of 290 cm^{-1} to 305 cm^{-1}. Compared with the other two curves (obtained at 0.4, 0.6 Pa), the Raman peak of 0.8 Pa sample has the highest intensity, the lowest FWHM values, and least defective structure.
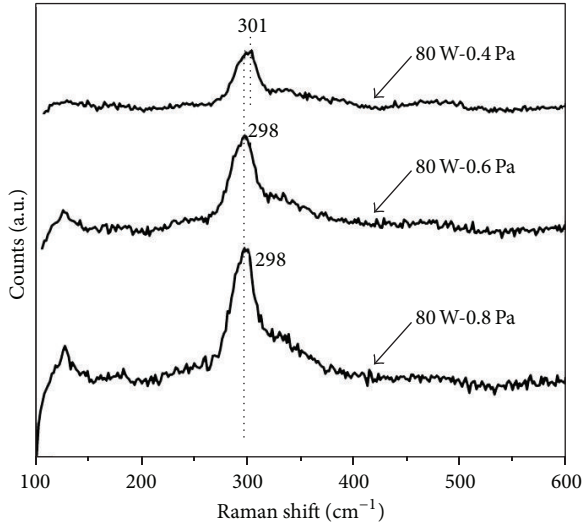
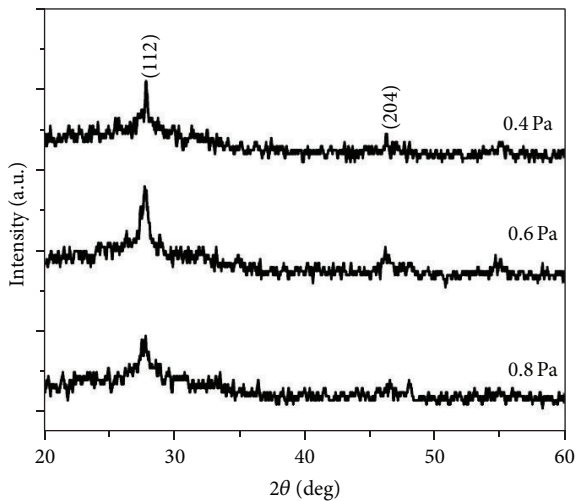FIGURE 4: Raman spectra of the CuInS$_2$ thin films with different sputtering gas pressure (sputtering power of 80 W).

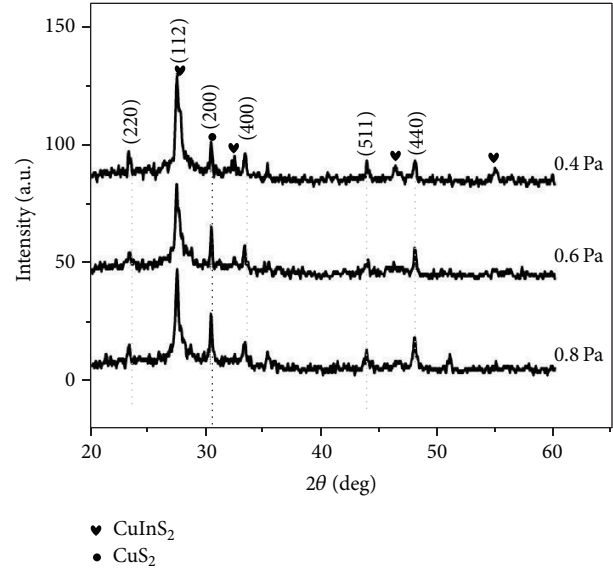FIGURE 5: XRD spectra of the CuInS$_2$ thin films with different sputtering gas pressure (sputtering power of 80 W).

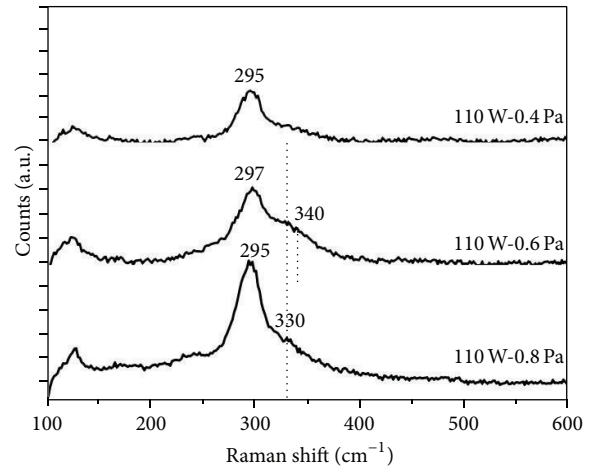FIGURE 6: XRD spectra of the CuInS$_2$ thin films with different sputtering gas pressure (sputtering power of 110 W).

FIGURE 7: Raman spectra of the CuInS$_2$ thin films with different sputtering gas pressure (sputtering power of 110 W).

Figure 5 shows the XRD spectra for the vulcanized Cu-In thin films of different sputtering gas pressure. Compared with the CuInS$_2$ standard card (JCPSD number 65-1572), the intensity of peaks in the XRD pattern is low and the characteristic peaks located at $2\theta = 27.8°$, $32.3°$, and $46.3°$ are consistent with the crystal face indices 112, 004, and 204, respectively. The reason for the reduced diffraction intensity may be incomplete crystallization creating more impurity phases, resulting in more defective structures in the sulfurization process of the heat treatment.

In order to improve the crystallinity of the films, certain parameters were varied and the experiments repeated. The sputtering power was increased to 110 W; heat treatment temperature was increased to 470°C whilst keeping the other process parameters unchanged. These results are shown in Figures 6 and 7. Figure 6 shows the XRD spectra for the

vulcanized Cu-In thin films of different sputtering pressures (specifically 0.4, 0.6, and 0.8 Pa). The information on the XRD patterns was obtained by comparing with the standard card CuInS$_2$ (JCPDS number 65-1572), CuIn$_{11}$S$_{17}$ (JCPDS number 34-0797), and CuS$_2$ (JCPDS number 65-4850). It can be seen from Figure 6 that the main diffraction peaks ($2\theta = 27.8°$) can be attributed to CuInS$_2$. The thin films exhibit the preferred orientation along the 112 plane and better structure. For the 2θ of $32.3°$, $43.8°$, and $54.7°$, each of these small diffraction peaks in the spectra is the characteristic peak of CuInS$_2$.

In addition, the other crystal face indices 220, 400, 511, and 440, which were marked in the spectra, are consistent with $2\theta = 23.5°$, $33.4°$, $43.8°$, and $48°$, respectively, and are attributed to CuIn$_{11}$S$_{17}$. For the $2\theta = 30.8°$, this is attributed to CuS$_2$ with the crystal face index of 200. An

explanation of the form of the $CuIn_{11}S_{17}$ and CuS_2 phase is the uneven distribution of Cu and In in the thin films. Under the same conditions, the energy required to remove Cu and In out of the target material by sputtering is different and so different sputtering rates result in rich In being deposited on the substrate. Due to the small radius of the Cu atom and its disordered arrangement on the substrate, a part of it is embedded into In atoms. For the sulfurization process, the Cu and S atoms are naked on the surface of thin films and combine with nucleation to grow and form copper sulfides, such as CuS and CuS_2. Combined with S forms indium sulfides, copper sulfides then react with indium sulfides to form the $CuInS_2$ phase, where the Cu atoms are surrounded by In atoms that can combine with In and S atoms to form the new $CuIn_{11}S_{17}$ phase.

Figure 7 shows the Raman spectra of $CuInS_2$ thin films obtained in the second experiments. The Raman peaks located at 295 cm^{-1} and 297 cm^{-1} correspond to the structure of $CuInS_2$ chalcopyrite. When the sputtering pressure is at 0.6 Pa there is a less obvious Raman peak located at 340 cm^{-1}. According to the literature and XRD spectra, we can conclude that the peak is attributed to $CuIn_{11}S_{17}$ phase. With a sputtering pressure of 0.6 and 0.8 Pa, the intensity of the small Raman peak located at 330 cm^{-1} is low; according to the XRD spectra (Figure 6) it can be concluded that a CuS_2 phase is contained in the thin films. In contrast, when the sputtering pressure is at 0.6–0.8 Pa, the intensity of Raman peaks is higher and the FWHM value is lower with better crystallization and less phase impurity.

3.3. The Influence of Sulfurization Temperature on Crystallinity of the $CuInS_2$ Thin Films.

The vulcanization heat treatment process is the key stage for Cu-In crystallization. Under the same conditions of sputtering power (110 W), the same sputtering pressure (0.6 Pa), and the same sputtering time of 20 minutes, sputtering batches of Cu-In prefabricated films were carried out using vulcanization heat treatment at temperatures of 450°C, 470°C, and 500°C. A holding time of 3 hours and sulfur amount of 2 g remained unchanged. The experimental results are shown in Figures 8 and 9.

Figure 8 shows the XRD spectra for Cu-In thin films of different temperatures. The diffraction peaks in the XRD patterns for the samples are well matched with the standard card of $CuInS_2$ (JCPDS number 65-1572), $CuIn_5S_8$ (JCPDS number 54-0554), and CuS (JCPDS number 65-4850), respectively. As shown, the main diffraction peaks ($2\theta = 27.8°$) are attributed to $CuInS_2$. The thin films exhibited the preferred orientation along the 112 plane. The other diffraction peaks with the crystal face indices 220, 311, 400, 511, and 440 which were marked in the spectra are consistent with $2\theta = 23.5°, 27.7°, 33.6°, 43.9°,$ and $48.1°$, respectively; these are the characteristic peaks of $CuIn_5S_8$ and the 311 plane ($2\theta = 27.7°$) overlapping with the 112 plane ($2\theta = 27.8°$) of $CuInS_2$. In addition, diffraction peaks of the CuS_2 phase emerged in the XRD spectra at different temperatures corresponding to the $2\theta = 30.8°$ and the crystal face index is 200. Compared with the other two spectra shown in Figure 8, when the heat treatment is 470°C, the crystallization of the $CuInS_2$ thin films is improved with less phase impurity.
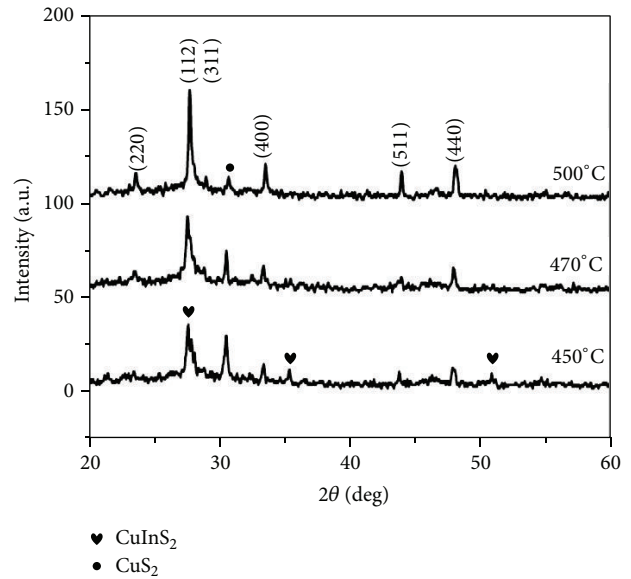

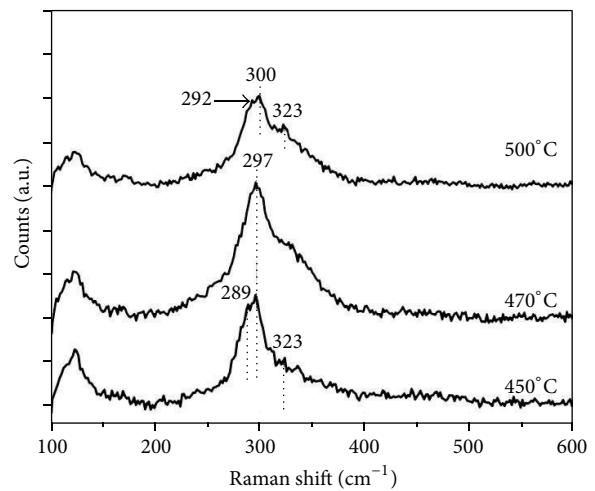FIGURE 8: The XRD spectra of the $CuInS_2$ thin films with different sulfuration temperature.

FIGURE 9: Raman spectra of the $CuInS_2$ thin films with different sulfuration temperature.

Figure 9 shows the Raman spectra of the thin films obtained at different sulfide heat treatment temperatures for three hours, the two main Raman peaks 289 cm^{-1} and 297 cm^{-1} corresponding to the $CuInS_2$ chalcopyrite phase, and another peak 323 cm^{-1} which corresponds to the β-In_2S_3 phase. At a sulfurization temperature of 470°C, the Raman peak located at 297 cm^{-1} corresponds to the symbionts of $CuInS_2$ chalcopyrite and Cu-Au phases. At the sulfurization temperature of 500°C, the two main Raman peaks located at 292 cm^{-1} and 300 cm^{-1} show that the structure is not a single chalcopyrite phase but the symbionts of the $CuInS_2$ chalcopyrite and Cu-Au phases. There is also a peak located at 323 cm^{-1} corresponding to the β-In_2S_3 phase, similar to that at 450°C. In contrast to the Raman peak of $CuInS_2$ thin film
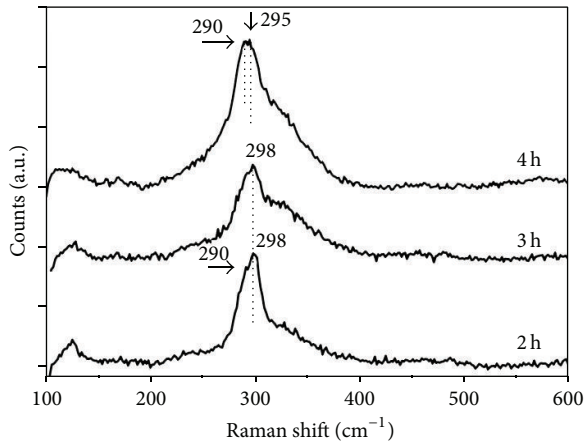
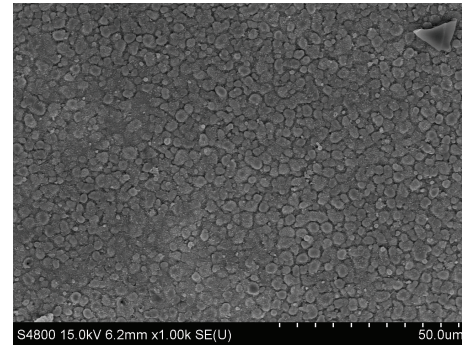FIGURE 10: Raman spectra of the CuInS$_2$ thin films with different holding time.

(a)

(b)

FIGURE 11: SEM micrographs of the samples prepared under the optimized condition: the holding time is 2 h; the sulfurization temperature is 470°C; the sputtering pressure is 0.8 Pa; the sputtering power is 80 W.

of 470°C, the FWHM values are reduced, the chalcopyrite structure is unitary, and the crystallinity is improved.

3.4. The Influence of Heat Treatment Time on Crystallinity of the CuInS$_2$ Thin Films.

The experimental results are shown in Figure 10 for sputtering out a batch of Cu-In prefabricated films and carrying on vulcanization heat treatment at different holding times of 2 hours, 3 hours, and 4 hours. Other parameters were at a sputtering power of 80 W, a sputtering gas pressure of 0.4 Pa, a sputtering time of 20 minutes, a sulfurization temperature of 500°C, and a sulfur amount of 2 g.

Figure 10 is the Raman spectra of the CuInS$_2$ thin films with different holding times. The two main Raman peaks at 290 cm^{-1} and 298 cm^{-1} correspond to holding times of 2 hours during the CuInS$_2$ chalcopyrite phase. At a holding time of 3 hours, a single main Raman peak is observed located at 298 cm^{-1}. At a holding time of 4 hours, there are two Raman peaks located at 290 cm^{-1} and 295 cm^{-1}, both of which are the characteristic peaks of chalcopyrite structure. Therefore, at a holding time of 2 hours, the intensity of the Raman peak is higher, the FWHM value is decreased, and the crystallinity is improved.

3.5. The Morphology and Optical Properties of CuInS$_2$ Thin Films.

The optical band gap is calculated using the following equation: $\alpha h\nu = A(h\nu - E_g)^n$. In this equation, $h\nu$ is the photon energy, α is the absorption coefficient of the thin film, E_g is the optical band gap, and A is the bandwidth coefficient, which is connected with refractive index and the direct transition oscillator strength; it is a constant value and for the direct band gap semiconductor materials n is 1/2. According to this equation, the optical band gap of the thin films can be estimated.

Figure 11 shows the SEM micrographs of CuInS$_2$ thin films synthesized under the optimized process conditions (the holding time of 2 hours; the sulfurization temperature of 470°C; a sputtering pressure of 0.8 Pa; a sputtering power of 80 W). The micrographs shown in Figure 11(a) suggest that
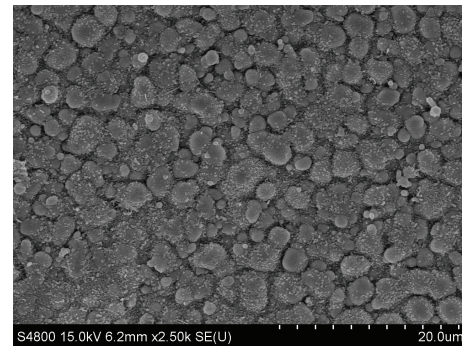
the grains are relatively evenly distributed and consist mostly of grains around 2–5 μm. This data also shows that the grains are spherical; however, Figure 11(b) suggests that the spherical grains are deposited by many small particles. It is known that smaller, nanosized particles can easily and spontaneously agglomerate to form larger particles.

Figure 12 shows the optical band gap of CuInS$_2$ thin films at process parameters indicated. The optical band gap values of the CuInS$_2$ thin films are 1.48 eV and 1.5 eV, respectively. In addition, metallographic microscope and metallographic image analysis were applied to measure the thickness of the thin films, with the average thickness ranging from 4 to 7 μm.

4. Conclusions

Using magnetron sputtering and sulfurization heat processes is an effective method to prepare CuInS$_2$ thin film. The sputtering pressure and sulfurization temperatures have a large influence on the quality of thin films. When improperly choosing process parameters, these will affect not only the CuInS$_2$ phase but also the CuIn$_{11}$S$_{17}$ and CuS$_2$ phases. The optical band gaps of prepared CuInS$_2$ thin film are around 1.48–1.5 eV. Based on the experiment results, the optimized process parameters are as follows: a sputtering power ranging from 80 to 120 W, a sputtering pressure of 0.6–0.8 Pa with the heat treatment temperature in the range of 450 to 470°C, and
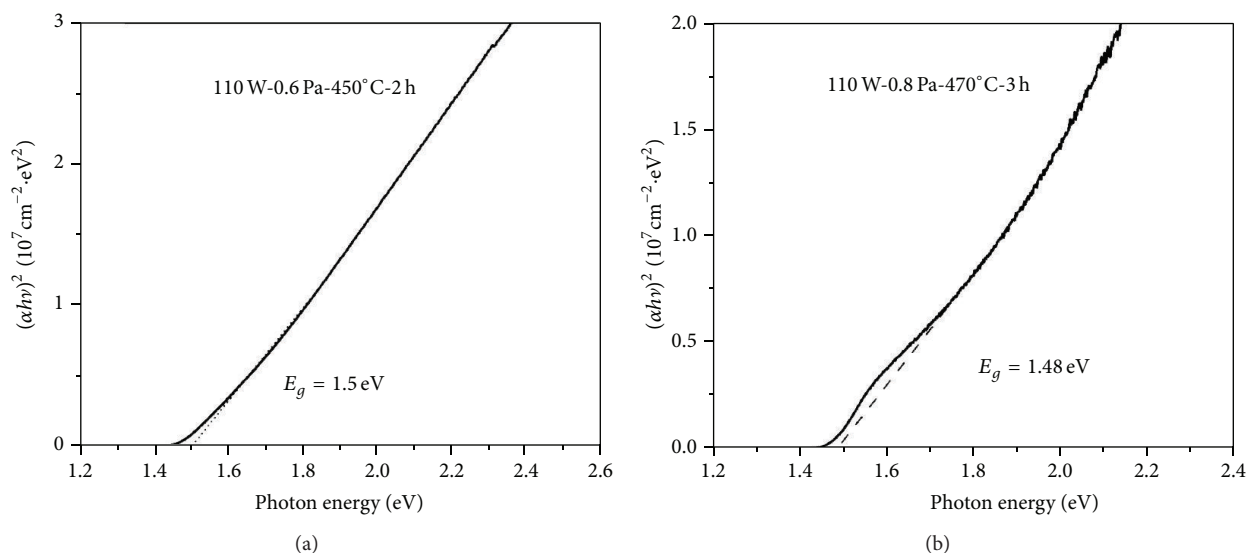
FIGURE 12: The optical band gap of CuInS$_2$ thin films synthetized by different sulfuration conditions.

a holding time ranging from 2 to 3 hours. The thickness of the CuInS$_2$ thin film is between 6 and 10 μm.

Conflict of Interests

The authors declare that there is no conflict of interests regarding the publication of this paper.

Acknowledgments

References

[1] W. Yao, Y. Wang, X. Wang, J. Zhu, Z. Zhang, and X. Yuan, "CuInS$_2$ thin films obtained by solid-state sulfurization," *Materials Science in Semiconductor Processing*, vol. 26, no. 1, pp. 175–181, 2014.

[2] Z. Peng, Y. Liu, Y. Zhao et al., "ZnSe passivation layer for the efficiency enhancement of CuInS$_2$ quantum dots sensitized solar cells," *Journal of Alloys and Compounds*, vol. 587, pp. 613–617, 2014.

[3] T. Li, X. Li, Q. Zhao, Y. Shi, and W. Teng, "Fabrication of n-type CuInS$_2$ modified TiO$_2$ nanotube arrays heterostructure photoelectrode with enhanced photoelectrocatalytic properties," *Applied Catalysis B: Environmental*, vol. 156-157, pp. 362–370, 2014.

[4] K. Siemer, J. Klaer, I. Luck, J. Bruns, R. Klenk, and D. Bräunig, "Efficient CuInS$_2$ solar cells from a rapid thermal process (RTP)," *Solar Energy Materials and Solar Cells*, vol. 67, no. 1–4, pp. 159–166, 2001.

[5] J. J. M. Binsma, L. J. Giling, and J. Bloem, "Luminescence of CuInS$_2$. I. The broad band emission and its dependence on the defect chemistry," *Journal of Luminescence*, vol. 27, no. 1, pp. 35–53, 1982.

[6] H. Goto, Y. Hashimoto, and K. Ito, "Efficient thin film solar cell consisting of TCO/CdS/CuInS$_2$/CuGaS$_2$ structure," *Thin Solid Films*, vol. 451-452, pp. 552–555, 2004.

[7] T. Nakabayashi, T. Miyazawa, Y. Hashimoto, and K. Ito, "Over 10% efficient CuInS2 solar cell by sulfurization," *Solar Energy Materials & Solar Cells*, vol. 49, no. 1–4, pp. 375–381, 1997.

[8] S. Seeger and K. Ellmer, "Reactive magnetron sputtering of CuInS$_2$ absorbers for thin film solar cells: problems and prospects," *Thin Solid Films*, vol. 517, no. 10, pp. 3143–3147, 2009.

[9] A. S. Cherian, K. B. Jinesh, Y. Kashiwaba et al., "Double layer CuInS$_2$ absorber using spray pyrolysis: a better candidate for CuInS$_2$/In$_2$S$_3$ thin film solar cells," *Solar Energy*, vol. 86, no. 6, pp. 1872–1879, 2012.

[10] D.-Y. Lee and J. Kim, "Deposition of CuInS$_2$ films by electrostatic field assisted ultrasonic spray pyrolysis," *Solar Energy Materials and Solar Cells*, vol. 95, no. 1, pp. 245–249, 2011.

[11] C.-H. Fischer, N. A. Allsop, S. E. Gledhill et al., "The spray-ILGAR (ion layer gas reaction) method for the deposition of thin semiconductor layers: process and applications for thin film solar cells," *Solar Energy Materials & Solar Cells*, vol. 95, no. 6, pp. 1518–1526, 2011.

[12] G.-T. Pan, M.-H. Lai, R.-C. Juang, T.-W. Chung, and T. C.-K. Yang, "The preparation and characterization of Ga-doped CuInS$_2$ films with chemical bath deposition," *Solar Energy Materials & Solar Cells*, vol. 94, no. 10, pp. 1790–1796, 2010.

[13] S. M. Lee, S. Ikeda, Y. Otsuka, W. Septina, T. Harada, and M. Matsumura, "Homogeneous electrochemical deposition of in on a Cu-covered Mo substrate for fabrication of efficient solar cells with a CuInS$_2$ photoabsorber," *Electrochimica Acta*, vol. 79, pp. 189–196, 2012.

[14] S. Ebrahim, I. Morsi, M. Soliman, M. Elsharkawi, and A. Elzaem, "Preparation and characterization of chalcopyrite compound for thin film solar cells," *Alexandria Engineering Journal*, vol. 50, no. 1, pp. 35–42, 2011.

[15] C. Broussillou, M. Andrieux, M. Herbst-Ghysel et al., "Sulfurization of Cu–In electrodeposited precursors for CuInS$_2$-based

solar cells," *Solar Energy Materials & Solar Cells*, vol. 95, no. 1, pp. S13–S17, 2011.

[16] N. Meyer, A. Meeder, and D. Schmid, "Pilot production of large-area $CuInS_2$-based solar modules," *Thin Solid Films*, vol. 515, no. 15, pp. 5979–5984, 2007.

[17] Y. B. He, A. Krost, J. Bläsing et al., "Quasi-epitaxial growth of thick $CuInS_2$ films by RF reactive sputtering with a thin epilayer buffer," *Thin Solid Films*, vol. 451-452, pp. 229–232, 2004.

[18] Y. B. He, W. Kriegseis, T. Krämer et al., "Deposition of $CuInS_2$ thin films by RF reactive sputtering with a ZnO:Al buffer layer," *Journal of Physics and Chemistry of Solids*, vol. 64, no. 9-10, pp. 2075–2079, 2003.

Research Article

The Luminescence Properties and Energy Transfer from Ce³⁺ to Pr³⁺ for YAG:Ce³⁺Pr³⁺ Phosphors

Rongfeng Guan,[1] Liu Cao,[2] Yajun You,[1] and Yuebin Cao[1,3]

[1]*Key Laboratory for Advanced Technology in Environmental Protection of Jiangsu, Yancheng Institute of Technology, Jiangsu 224051, China*
[2]*Beijing Water Science Technology Institute, Beijing 100044, China*
[3]*Department of Chemical Engineering, Hanyang University, Ansan 426791, Republic of Korea*

Correspondence should be addressed to Yuebin Cao; hxxcyb@gmail.com

$Y_{2.94-x}Al_5O_{12}$ (YAG):$Ce_{0.06}Pr_x$ phosphors with various Pr^{3+} concentrations ($x = 0$, 0.006, 0.01, 0.03, 0.06, and 0.09) were synthesized by using a coprecipitation method. The phases, luminescent properties, and energy transfer phenomenon from Ce^{3+} to Pr^{3+} were investigated. The results indicated that the doping of Pr^{3+} ($x \leq 0.09$) did not produce any new phases but caused a slight lattice parameters increase. After Pr^{3+} doping, the YAG:CePr phosphor emits red light at 610 nm, which was regarded helpful for improving the colour rendering index of the phosphor. With Pr^{3+} concentration increase from 0.006 to 0.01 mol, the intensity of red light emission increased slightly; further increasing Pr^{3+} concentration from 0.01 to 0.09, the red light emission intensity decreased gradually. Excitation at 340, and 460 nm could not lead to the direct electronic excitation of Pr^{3+} ions; however, when YAG:CePr was excited at 340 nm a red light emission at 610 nm appeared, which implied the energy transfer phenomenon from Ce^{3+} to Pr^{3+}.

1. Introduction

As the fourth generation lighting sources, white-light emitting diodes (LEDs) have the following advantages: high efficiency to convert electrical energy to light, high reliability, and long operating lifetime (about 100000 h). They have been employed in the devices such as solid-state lasers, traffic lights, and field-emission displays [1–3]. Usually, white LEDs are fabricated by the combination of blue InGaN chips and yellow-emitting phosphor (YAG:Ce) [4–6]. However, the combined InGaN chips and YAG:Ce suffers from a low colour rendering index (<80) because of red light shortage in its emission spectrum. There are two methods to solve this problem: first, add an amount of red phosphor to yellow phosphor YAG:Ce to improve its colour rendering [7]; second, dope YAG:Ce phosphors to improve the red light emission [8–11]. As the ionic radius of Pr^{3+} is similar to Y^{3+}, it has been used to dope YAG:Ce phosphor to improve its red spectrum emission. Jang et al. [12] synthesized YAG:CePr phosphors with various Pr concentrations through a high temperature solid-state reaction. The obtained YAG:CePr phosphors used for white LEDs improved the colour rendering index between 80 and 83. Yang et al. [13] synthesized Pr^{3+} doped YAG:Ce nanopowder by polymer-assisted sol-gel method, which also showed a high colour rendering index of 83 in white LEDs. However, the researches on Pr^{3+} doped YAG:CePr are still limited; particularly, the energy transfer phenomenon from Ce^{3+} to Pr^{3+} is seldom researched. Here, we report the synthesis of YAG:CePr phosphors by a coprecipitation method, and the effects of Pr^{3+} doping concentrations on the properties of YAG:CePr including phases, light absorption, and luminescent properties are researched. In addition, the energy transfer from Ce^{3+} to Pr^{3+} is characterized and proved through luminescent and fluorescence lifetime measurements.

2. Experiments

YAG:$Ce_{0.06}Pr_x$ ($x = 0$, 0.006, 0.01, 0.03, 0.06, and 0.09) phosphors were prepared by coprecipitation method.

Stoichiometric amounts of source materials Y_2O_3(AR), $Al(NO_3)_3\cdot9H_2O$(AR), $Ce(NO_3)_3\cdot6H_2O$(AR), Pr_6O_{11}(AR), NH_4HCO_3(AR), $NH_3\cdot H_2O$(AR), and HNO_3(AR) were thoroughly mixed in solution. The Y^{3+} and Pr^{3+}/Pr^{4+} solution was obtained by dissolving Y_2O_3 and Pr_6O_{11} in HNO_3 aqueous solution, and this solution was denoted as solution A; $Al(NO_3)_3\cdot9H_2O$ and $Ce(NO_3)_3\cdot6H_2O$ were dissolved in a suitable amount of deionized water to obtain solution B; NH_4HCO_3 was also dissolved in deionized water, and the solution was denoted as C. Solutions A and B were mixed to obtain solution D, and then solution D was added (dropwise) to solution C at a rate of 1 mL/min. After finishing the dropping process, the system was adjusted to pH of 8 by using $NH_3\cdot H_2O$ and stirred for 2 h, and then the obtained precipitate was aged for 12 h. The white precipitate was filtered and then washed for 3 times by using deionized water and anhydrous ethanol, respectively. The filtered product was dried at 120°C for 12 h, ground, and mixed together with NaF (6 wt%) to form the precursor. The precursor was annealed at 1600°C for 3 h in a reductive atmosphere (with 95% N_2 and 5% H_2) to get the target product.

The phase characterization of the synthesised materials was conducted with X-ray powder diffraction (XRD) on a D8 Advance diffractometer (Bruker) operating at 40 kV, 200 mA, using Cu Kα radiation with a scanning rate of 1°/min and scanning range of $10° \leq 2\theta \leq 80°$.

The photoluminescence spectra were measured on powder samples at room temperature using Hitachi F-4500 luminescence spectrometer with a xenon discharge lamp (150 W) as the excitation source. The excitation spectra were obtained over the range of 200 to 550 nm and emission spectra were obtained over the range of 450 to 665 nm. Both excitation and emission splits were 5.0 nm, and the scanning interval was 0.2 nm. UV-visible absorption and diffuse reflectance spectra were monitored by a SHIMADAZU Japan UV 2700, with wavelength range from 200 to 800 nm and scanning interval of 0.5 nm.

3. Results and Discussion

3.1. Phases Analysis.
Figure 1 shows XRD patterns of the YAG:$Ce_{0.06}Pr_x$ (x = 0, 0.006, 0.01, 0.03, 0.06, and 0.09) annealed at 1600°C for 3 h. All the diffraction peaks can be indexed to standard data of $Y_3Al_5O_{12}$ (JCPDS 33-0040), without the possible intermediate phases such as $Y_4Al_2O_9$ or YAlO$_3$. It means the samples were phase-pure and doping of the activator ions Pr^{3+} did not cause any observable new phases. Lattice parameters of YAG:$Ce_{0.06}Pr_x$ are calculated and the results are listed in Table 1. With increase of Pr^{3+} doping concentration, diffraction peaks of the phosphors shifted to lower degree and lattice parameters increased slightly, which can be explained by the larger radius of Pr^{3+} (r = 126.6 pm) than that of Y^{3+} (r = 115.9 pm).

3.2. Spectral Analysis

3.2.1. Ultraviolet-Visible Absorption and Diffuse Reflectance Spectra.
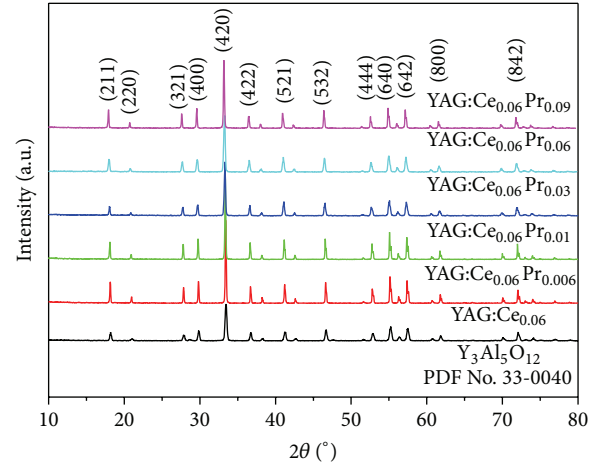Figure 2(a) shows the absorption spectra of YAG:Ce. The excitation (absorption) peaks at 245, 340, and 457 nm

FIGURE 1: XRD patterns of YAG:$Ce_{0.06}Pr_x$ (x = 0, 0.006, 0.01, 0.03, 0.06, and 0.09) samples.

were attributed to 4f → 5d transitions of the Ce^{3+} ions. The strong absorption peak located at 460 nm matched well with blue-light LED chips, which means the prepared YAG:Ce phosphors can absorb blue light from LED chips efficiently.

Figures 2(b)–2(e) show the absorption spectra of YAG:$Ce_{0.06}Pr_x$ phosphors with x = 0.01, 0.03, 0.06, and 0.09 mol, respectively. With increase of Pr^{3+} concentration, the two narrow absorption peaks appeared at 239 and 289 nm which correspond to the $4f^2(^3H_4) \rightarrow 4f5d$ transition of Pr^{3+} [9] increased significantly. When part Y^{3+} sites were substituted by Pr^{3+} ions, lattice parameters of the crystal became larger, causing subtle changes around the field of Ce^{3+} luminescence centre. Therefore, it is possible that the doping of Pr^{3+} will change absorption properties of Ce^{3+}. After Pr^{3+} doping, the typical absorption peaks of Ce^{3+} ions still exist in YAG:CePr phosphors, indicating the doping of Pr^{3+} has little effects on the absorption properties of Ce^{3+}. Presence of absorption peak at 457 nm means that YAG:CePr can absorb blue light from LED chips.
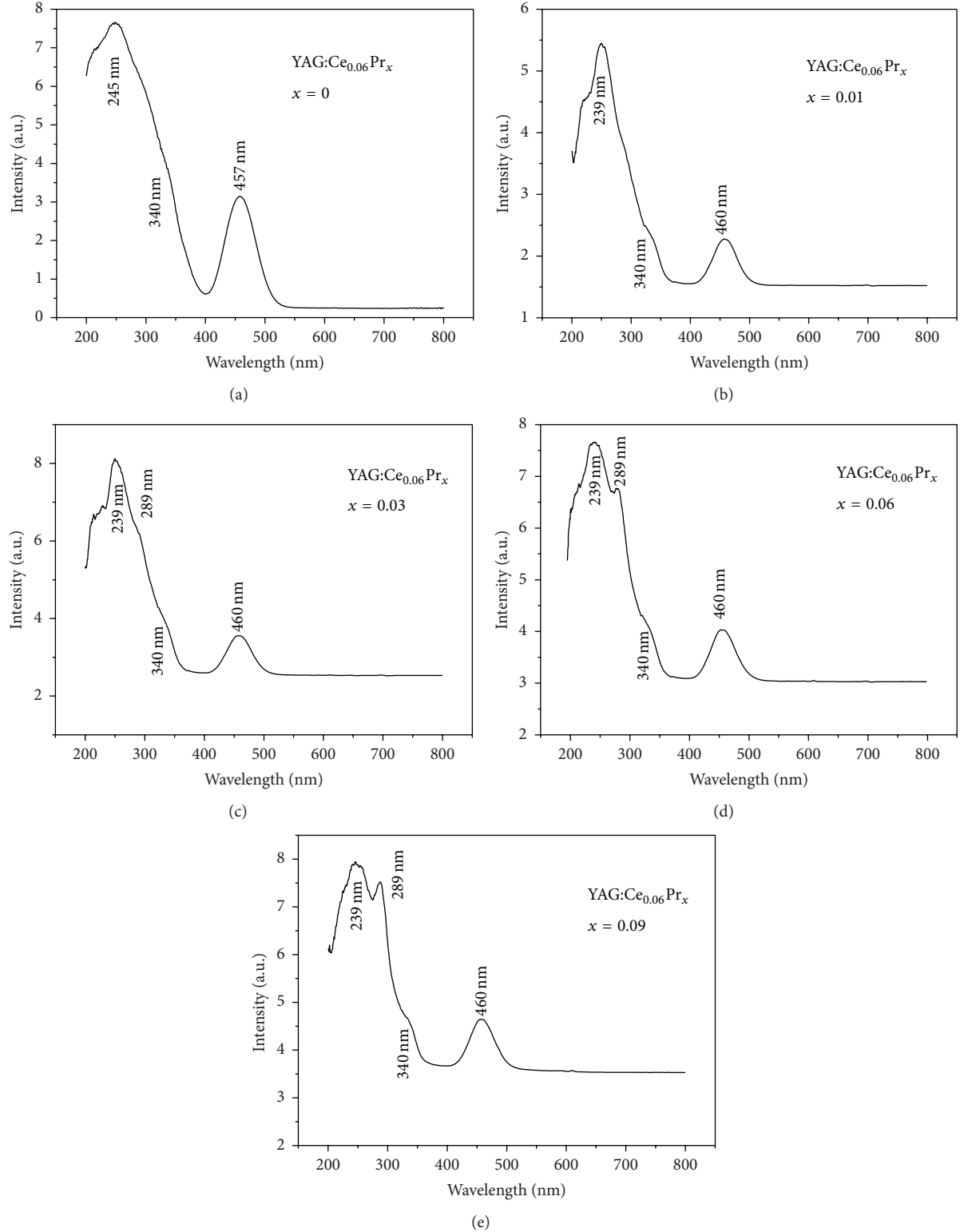
Diffuse reflection spectra of YAG:$Ce_{0.06}Pr_x$ were measured and the results were shown in Figure 3. YAG:Ce^{3+} phosphor without Pr^{3+} doping had a strong broad absorption peak at 460 nm and weak absorption band from 270 to 400 nm. With Pr^{3+} doping into the YAG:$Ce_{0.06}Pr_x$ phosphors, a small absorption peak appeared at 610 nm. With increase of Pr^{3+} concentration, intensity of the absorption peak at 610 nm gradually increased. At the same time, with Pr^{3+} concentration increase, the absorption intensity of 460 nm decreased, which may be caused by the formation of defects during Pr^{3+} doping [13].

3.2.2. Excitation and Emission Spectra.
Figure 4 shows the emission spectra of YAG:$Ce_{0.06}Pr_x$ (x = 0.006, 0.01, 0.03, 0.06, and 0.09) phosphors excited at wavelengths of 340 nm and 460 nm, respectively. As shown in the emission spectra, they both show a broad peak around 534 nm and a sharp peak around 610 nm. The electron configuration of $4f^1$ for Ce^{3+} can transfer to its excited state of $4f^05d^1$ and split into

TABLE 1: Lattice parameters of YAG:$Ce_{0.06}Pr_x$ ($x = 0$, 0.006, 0.01, 0.03, 0.06, and 0.09).

YAG:$Ce_{0.06}Pr_x$	$x = 0$	$x = 0.006$	$x = 0.01$	$x = 0.03$	$x = 0.06$	$x = 0.09$
$a = b = c$ (Å)	11.9962	12.0105	12.0164	12.0190	12.0295	12.0327

(a)

(b)

(c)

(d)

(e)

FIGURE 2: Absorption spectra of YAG:$Ce_{0.06}Pr_x$ phosphor with $x = 0$ (a), 0.01 (b), 0.03 (c), 0.06 (d), and 0.09 (e).
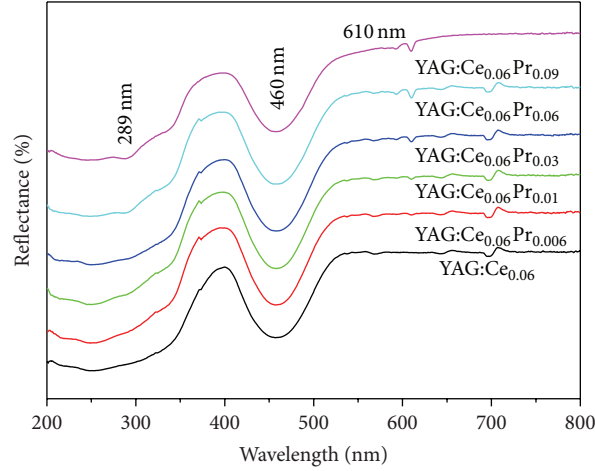
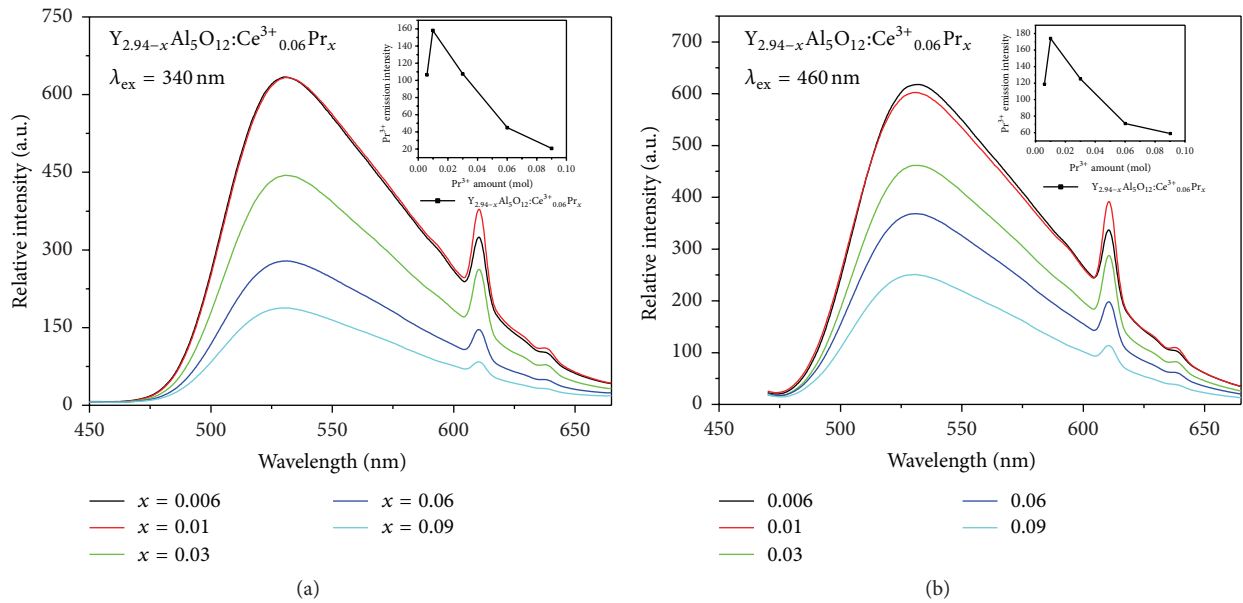FIGURE 3: UV-vis diffuse reflectivity spectra of YAG:Ce$_{0.06}$Pr$_x$ phosphors.

FIGURE 4: PL emission spectra of YAG:Ce$_{0.06}$Pr$_x$ phosphors excited at 340 nm (a) and 460 nm (b).

two spectroscopic terms $^2F_{7/2}$ and $^2F_{5/2}$ by spin coupling. The broad peak located at 534 nm in the yellow-green region can be attributed to the $4f^05d^1 \rightarrow {}^2F_{7/2}, {}^2F_{5/2}$ transition. The appearance of 610 nm, which is caused by $^1D_2 \rightarrow {}^3H_4$ transition of the Pr^{3+} ion [9, 13], indicates that Pr^{3+} doping increased the red light emission for YAG:Ce$_{0.06}$Pr$_x$. With Pr^{3+} doping concentration increasing, the intensity of yellow light emission at 534 nm decreased. Specifically, the intensity of the yellow light emission peak decreased from 632.48 ($x = 0.006$) to 183.24 ($x = 0.09$) under excitation at 340 nm (a decrease of 449.24); and the intensity decreased from 616.47 ($x = 0.006$) to 246.21 ($x = 0.09$) under excitation at 460 nm (a decrease of 370.26).

For the red light from Pr^{3+} emission at 610 nm, the intensity firstly increased to the maximum at $x = 0.01$ and

then decreased monotonically. Insets of Figures 4(a) and 4(b) present the relation of the Pr^{3+} doping concentration and the PL emission intensity of 610 nm at excitation at 340 nm and 460 nm, respectively. Specifically, under excitation at 340 nm, the peak intensity increased gradually from 106.36 to 157.54 when x increased from 0.006 to 0.01 and then decreased from 157.54 to 21.16 when x further increased from 0.01 to 0.09. A similar trend for the spectra that are excited at 460 nm is shown. Firstly, with Pr^{3+} concentration increase (from 0.006 to 0.01), part Y^{3+} was substituted by Pr^{3+}, and thus intensity of red light which caused by Pr^{3+} increased. However, further increase of Pr^{3+} concentration (from 0.01 to 0.09) decreased the distance between Pr^{3+} and Pr^{3+}, which induced the self-quenching phenomenon, and thus decreased the light intensity.

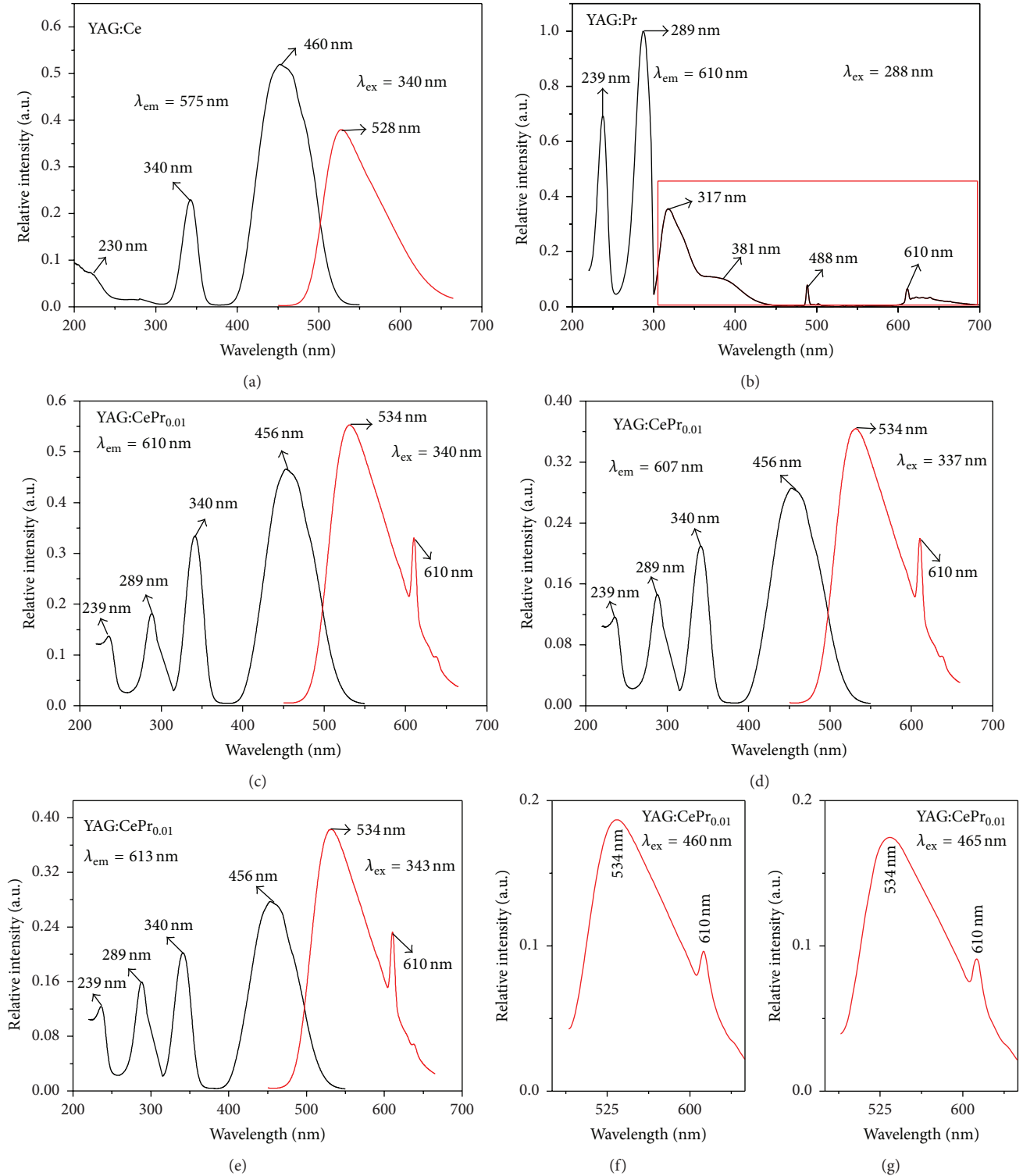FIGURE 5: PL excitation and emission spectra of YAG:$Ce_{0.06}$ (a), YAG:$Pr_{0.01}$ (b), and YAG:$Ce_{0.06}Pr_{0.01}$ (c–g) (black line is excitation spectra, and red line is emission spectra. For Figure 6(b), the emission spectrum of YAG:$Pr_{0.01}$ was encircled with a red box).

Figure 5 shows the excitation and emission spectra of YAG:$Ce_{0.06}$, YAG:$Pr_{0.01}$, and YAG:$Ce_{0.06}Pr_{0.01}$, respectively. The sample with singly doped Ce^{3+} showed a strong yellow light emission at 528 nm arising from the 5d → 4f transitions of Ce^{3+} ions, and the excitation spectra included a blue absorption at 460 nm and two UV absorptions at 230 nm and 340 nm. For the singly doped Pr^{3+}, at an excitation at 288 nm, the emission spectra can be divided into three
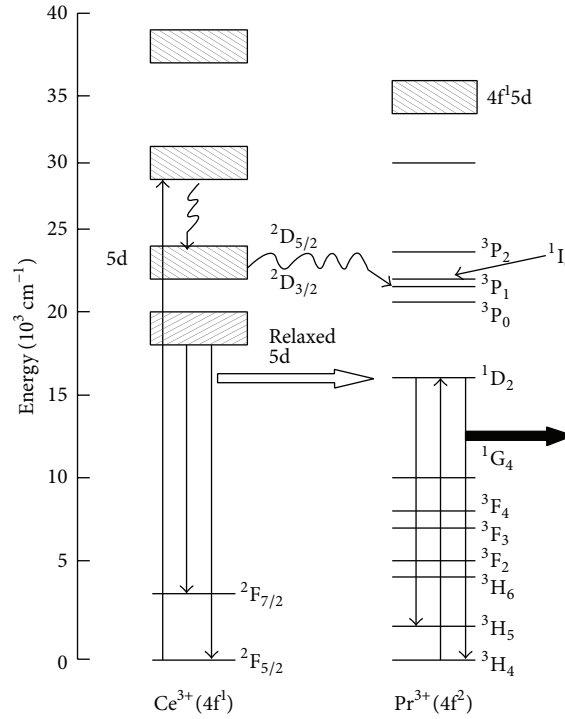
FIGURE 6: Energy level diagram and energy transfer of YAG:$Ce^{3+}Pr^{3+}$.

groups. The group in the UV region consisted of two broad emission bands at 317 nm and 381 nm, which were attributed to the $4f5d \rightarrow {}^3H_J$ (J = 4, 5, and 6) and $4f5d \rightarrow {}^3F_J$ (J = 2, 3, and 4) transitions of Pr^{3+}, respectively. The emission group in the range of 450 nm to 600 nm was attributed to the ${}^3P_0 \rightarrow {}^3H_{4,5}$ transition, and the main peak at 488 nm was due to ${}^3P_0 \rightarrow {}^3H_4$ transition. The other group was a red light emission at 610 nm, which was attributed to ${}^1D_2 \rightarrow {}^3H_4$ transitions. As shown in the excitation spectra of singly doped Pr^{3+}, two UV absorptions were located at 239 nm and 289 nm but no absorption peaks at 340 nm. However, under excitation at 340 nm, the emission spectra of Ce^{3+} and Pr^{3+} codoped YAG:$Ce_{0.06}Pr_{0.01}$ exhibit not only the yellow emission caused by Ce^{3+} but also the red emission caused by Pr^{3+} (Figure 5(c)). Figures 5(d) and 5(e) show the emission spectra excited at 337 nm and 343 nm respectively, and they also show similar emission spectra to that excited at 340 nm. As the excitation at 340 nm cannot lead to the direct electronic excitation of Pr^{3+} ions, the appearance of 610 nm red line emission from Pr^{3+} indicates the energy transfer from the excited Ce^{3+} to its neighbouring Pr^{3+} ions. To further prove the energy transfer phenomenon, YAG:$Ce_{0.06}Pr_{0.01}$ was excited at 460 and 465 nm, and its emission spectra were shown in Figures 5(f) and 5(g). It can be seen that the red light emission at 610 nm also exists under excitation at 460 and 465 nm, which further confirmed the energy transfer from Ce^{3+} to Pr^{3+}.

Figure 6 shows the energy level diagram and energy transfer behaviour of YAG:$Ce^{3+}Pr^{3+}$. It shows that the energy can be transferred from the 5d relaxed state of Ce^{3+} ion to

${}^1D_2$ energy level of the Pr^{3+} ion through a radiative transition process. And the energy can also be transferred from the lowest 5d band of Ce^{3+} to ${}^3P_0$ energy level of Pr^{3+} through a nonradiative process. The relaxed lowest 5d band of the Ce^{3+} ion is located at around 18,500 cm^{-1}, and therefore the energy transfer may occur radioactively at the D single state and the ${}^1D_2 \rightarrow {}^3H_4$ transition may lead to red light emission. If the energy transfers from the 5d energy band of Ce^{3+} to the ${}^3P_0$ energy band of Pr^{3+} through a nonradiative transition, a green light emission (${}^3P_0 \rightarrow {}^3H_4$) and a red light emission (${}^1D_2 \rightarrow {}^3H_4$) should appear simultaneously. However, the green light emission (${}^3P_0 \rightarrow {}^3H_4$) did not appear which meant that the nonradiative transition from the lowest 5d band of Ce^{3+} to ${}^3P_0$ energy level of Pr^{3+} did not happen [9]. As shown in the above emission spectra, there was only a weak red emission (610 nm) due to the ${}^1D_2 \rightarrow {}^3H_4$ transition of Pr^{3+}, indicating the existence of radiative energy transfer from the 5d relaxed state of Ce^{3+} to the ${}^1D_2$ energy level of Pr^{3+}.

3.2.3. Fluorescence Lifetime. The fluorescence decay curves of the samples were measured, and they were exponentially fitted to obtain the fluorescence decay lifetime [14]. Figures 7(a) and 7(b) show the decay curves of yellow light emission under excitation at 340 and 460 nm, which were monitored at 534 nm. Figure 7(c) shows the decay curves of the red emission for the ${}^1D_2 \rightarrow {}^3H_5$ transition of Pr^{3+} under excitation at 340 nm, which were monitored at 610 nm. The fluorescence lifetimes of Ce^{3+} and Pr^{3+} are listed in Table 2. When doping Pr^{3+} into YAG:Ce^{3+}, the lifetime of yellow light
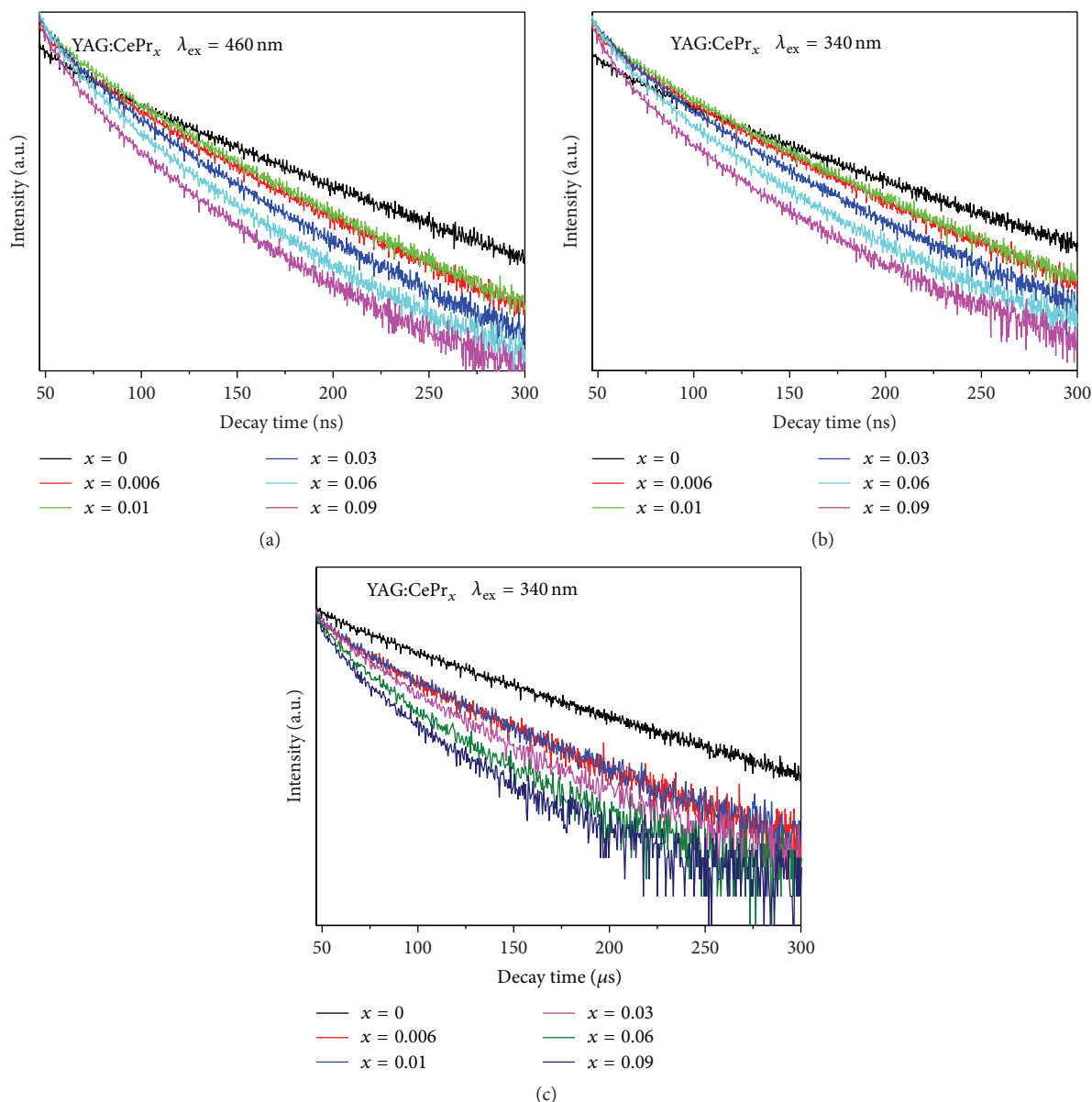
FIGURE 7: (a, b) Fluorescence lifetime of yellow light (534 nm) excited at wavelengths 340 nm (a) and 460 nm (b). (c) Fluorescence lifetime of red light (610 nm) excited at wavelength 340 nm.

decreased, and it further decreased as Pr^{3+} concentrations increase. Specifically, at excitation at 340 nm, fluorescence lifetimes of the yellow light emission decreased from 34.6 ns to 7.5 ns; and at excitation at 460 nm the fluorescence lifetimes decreased from 35.6 ns to 7.3 ns. In YAG:Ce^{3+}, only the energy transfer between two Ce^{3+} can happen, while in the codoped YAG:$Ce^{3+}Pr^{3+}$ there can be energy transfer between Pr^{3+} and Ce^{3+}. It may be the reason for lifetime decrease of yellow light. In the case of energy transfer from Ce^{3+} to Pr^{3+}, the decrease time from Ce^{3+} should be equal to the rise time from Pr^{3+}. However, the rise time from Pr^{3+} was not found here; oppositely, the lifetime of red light also decreased with Pr^{3+} doping. We guess the self-quenching between Pr^{3+} and Pr^{3+} maybe caused the lifetime decrease of red light.

4. Conclusions

A series of YAG:$Ce_{0.06}Pr_x$ phosphors with various Pr^{3+} concentrations ($x = 0$, 0.006, 0.01, 0.03, 0.06, and 0.09) were synthesised by coprecipitation method. Doping of Pr^{3+} did not change the phase of the YAG but induced a slight lattice parameters increase. Under excitation at either 340 nm or 460 nm, they both show a broad emission peak at 534 nm and a narrow emission peak at 610 nm. Appearance of the red emission peak at 610 nm was beneficial for improving the colour rendering of YAG:Ce^{3+}. As Pr^{3+} concentration increased from 0.006 to 0.01 mol, the intensity of red light emission increased slightly, and then it decreased gradually when Pr^{3+} concentration further increased from 0.01 to 0.09.

Table 2: Fluorescence lifetime of yellow and red light in $Y_{2.94-x}Al_5O_{12}:Ce^{3+}_{0.06}Pr_x$.

x	τ (ns) 5d of Ce^{3+}		τ (μs) $^1D_2$ of Pr^{3+}
	$\lambda_{ex} = 340$ nm $\lambda_{em} = 534$ nm	$\lambda_{ex} = 460$ nm $\lambda_{em} = 534$ nm	$\lambda_{ex} = 340$ nm $\lambda_{em} = 610$ nm
0	34.6	35.6	28.5
0.006	16.7	16.8	19.4
0.01	15.6	15.7	16.7
0.03	11.8	12.0	15.1
0.06	9.0	9.5	9.7
0.09	7.5	7.3	8.3

Emission properties of YAG:CePr at excitation at 340 and 460 nm proved the energy transfer from Ce^{3+} to Pr^{3+}.

Conflict of Interests

The authors declare that there is no conflict of interests regarding the publication of this paper.

Acknowledgments

References

[1] H. S. Jang, Y.-H. Won, and D. Y. Jeon, "Improvement of electroluminescent property of blue LED coated with highly luminescent yellow-emitting phosphors," *Applied Physics B: Lasers and Optics*, vol. 95, no. 4, pp. 715–720, 2009.

[2] J. K. Kim and E. F. Schubert, "Transcending the replacement paradigm of solid-state lighting," *Optics Express*, vol. 16, no. 26, pp. 21835–21842, 2008.

[3] F. K. Yam and Z. Hassan, "Innovative advances in LED technology," *Microelectronics Journal*, vol. 36, no. 2, pp. 129–137, 2005.

[4] R. Michael, O. Krames, B. Shchekin, M. M. Regina, G. O. Mueller, and L. Zhou, "Status and future of high-power light-emitting diodes for solid-state lighting," *Journal of Display Technology*, vol. 3, pp. 160–175, 2007.

[5] S. Ye, F. Xiao, Y. X. Pan, Y. Y. Ma, and Q. Y. Zhang, "Phosphors in phosphor-converted white light-emitting diodes: recent advances in materials, techniques and properties," *Materials Science and Engineering R: Reports*, vol. 71, no. 1, pp. 1–34, 2010.

[6] H.-T. Huang, Y.-P. Huang, and C.-C. Tsai, "Planar lighting system using array of blue leds to excite yellow remote phosphor film," *IEEE/OSA Journal of Display Technology*, vol. 7, no. 1, pp. 44–51, 2011.

[7] Z. Y. Liu, S. Liu, K. Wang, and X. B. Luo, "Optical analysis of phosphor's location for high-power light-emitting diodes," *IEEE Transactions on Device and Materials Reliability*, vol. 9, no. 1, pp. 65–73, 2009.

[8] C. C. Lin and R.-S. Liu, "Advances in phosphors for light-emitting diodes," *The Journal of Physical Chemistry Letters*, vol. 2, no. 11, pp. 1268–1277, 2011.

[9] X. Zhou, K. Zhou, Y. Li, Z. Wang, and Q. Feng, "Luminescent properties and energy transfer of $Y_3Al_5O_{12}:Ce^{3+},Ln^{3+}$ (Ln=Tb, Pr) prepared by polymer-assisted sol-gel method," *Journal of Luminescence*, vol. 132, no. 11, pp. 3004–3009, 2012.

[10] W. Wang, J. Tang, and P. Sullivan, "Energy transfer and enriched emission spectrum in Cr and Ce co-doped $Y_3Al_5O_{12}$ yellow phosphors," *Chemical Physics Letters*, vol. 457, pp. 103–105, 2008.

[11] H. Yang and Y.-S. Kim, "Energy transfer-based spectral properties of Tb-, Pr-, or Sm-codoped YAG:Ce nanocrystalline phosphors," *Journal of Luminescence*, vol. 128, no. 10, pp. 1570–1576, 2008.

[12] H. S. Jang, W. B. Im, D. C. Lee, D. Y. Jeon, and S. S. Kim, "Enhancement of red spectral emission intensity of $Y_3Al_5O_{12}:Ce^{3+}$ phosphor via Pr co-doping and Tb substitution for the application to white LEDs," *Journal of Luminescence*, vol. 126, no. 2, pp. 371–377, 2007.

[13] H. Yang, D.-K. Lee, and Y.-S. Kim, "Spectral variations of nano-sized $Y_3Al_5O_{12}:Ce$ phosphors via co-doping/substitution and their white LED characteristics," *Materials Chemistry and Physics*, vol. 114, no. 2-3, pp. 665–669, 2009.

[14] R. Singh and B. Pal, "Study of excited charge carrier's lifetime for the observed photoluminescence and photocatalytic activity of CdS nanostructures of different shapes," *Journal of Molecular Catalysis A: Chemical*, vol. 371, pp. 77–85, 2013.